

# Chapter 1

## Introduction

Laser light scattering techniques have been used since the early days of lasers to study properties of liquids [Benedek, 1968, Katyl and Ingard, 1967, Katyl and Ingard, 1968, Yeh and Cummins, 1964]. We have carried out optical studies of capillary waves at liquid-vapor interfaces using a light beating technique developed in our laboratory. In this thesis, the theoretical background and the experimental results of these studies are presented.

In Chapter 2, we begin with a general description of the light beating technique, Fourier transform heterodyne spectroscopy, which is central to all our experiments. The advantages of post-detection over pre-detection filtering methods, as well as the advantage of a frequency-shifted local oscillator for the study of liquid interfaces are discussed. The relationship between hydrodynamic fluctuations and the scattered light spectrum is also presented. We also show the

hydrodynamic fluctuations and the scattered light spectrum is also presented. We also show the basic experimental setup for Fourier transform heterodyne spectroscopy, and consider the experimental limits of the technique. Results obtained using this technique in crystal growth measurements and liquid surface studies are presented, and illustrate the high spectral resolution and directional sensitivity of the apparatus.

The Fourier transform heterodyne spectroscopy technique is first applied to measure the spectral asymmetry of light scattered from a nonequilibrium liquid-vapor interface in the presence of a temperature gradient. The derivation of the spectral asymmetry using a simple model, the results obtained from fluctuating hydrodynamic theory, as well as the experimental details and findings of this study are presented in Chapter 3.

Chapter 4 describes in detail the experimental apparatus and procedures, as well as the optical setup used for studying capillary wave damping. The experimental apparatus consists of a Langmuir trough, a surface area control, and a surface balance, all enclosed in a temperature-controlled chamber. A discussion on the cleaning procedures and liquid subphase handling is also presented. The optical setup incorporates the Fourier transform heterodyne spectroscopy with a differential measurement method, allowing for accurate measurements of the spatial damping coefficient of capillary waves. The advantages of this scheme and the wave generation method used in these experiments are also discussed.

Capillary wave damping on a pure liquid surface is examined in Chapter 5. The wave motion at the interface and the corresponding damping coefficients, are derived using hydrodynamic theory. The experimental results

obtained at a pure water-air interface are compared with the theoretical predictions.

Properties such as the spreading condition, two-dimensional pressure, and the phase behavior of an insoluble monolayer at a liquid-vapor interface are presented in Chapter 6. Particular attention is paid to the low surface concentration gas-liquid coexistence region

Capillary wave damping on a monolayer-covered liquid surface is examined in Chapter 7. Linearized hydrodynamics predicts a peak in the damping coefficient at some surface concentration of surfactant molecules. The damping coefficients are obtained to first order in perturbation theory. We compare the theoretical prediction and experimental results obtained for a water-air interface covered with a monolayer of pentadecanoic acid, and a discussion of the discrepancies between the two is presented. The possible use of damping measurements to locate phase transitions is also discussed.

## References

Benedek, G.B. in *Statistical Physics, Phase Transition and Superfluidity*, edited by M. Chretien, S. Deser and E. P. Gross, (Gordon and Breach Science Publishers, New York, 1968).

Katyl, R.H. and Ingard, K.U., *Phys. Rev. Lett.*, **19**, 64 (1967).

Katyl, R.H. and Ingard, K.U., *Phys. Rev. Lett.*, **20**, 248 (1968).

Yeh, Y. and Cummins, H.Z., *Appl. Phys. Lett.*, **4**, 176 (1964).

## Chapter 2

# Fourier Transform Heterodyne Spectroscopy

When a light beam is incident upon a rough surface, it is reflected, refracted, and at the same time scattered from the interface. Reflection is governed by Snell's law and refraction by the refractive indices of the two media forming the interface, while scattering depends upon the roughness of the surface. [Born and Wolf, 1980] For a surface whose roughness varies with time, it was first predicted by Brillouin [Brillouin, 1922] and Mandel'shtam, [Mandel'shtam, 1926] and later experimentally observed by Gross, [Gross, 1930] that the frequency of the scattered light is altered by the temporal behavior of the roughness. The resulting frequency spectrum is different from that of the incident light. Information about the dynamic behavior of the interface is therefore embedded in the scattered spectrum. In this chapter, light scattering at interfaces is

examined, with particular attention given to the relationship between optical correlations and hydrodynamic fluctuations. The theoretical consideration underlying Fourier transform heterodyne spectroscopy (FTHS), a surface light scattering technique developed in our laboratory, are presented, and limitations and applications of this technique are discussed.

## 2.1 Detected Signals and Optical Correlations

In a typical surface light scattering experiment, a light beam of intensity  $I_L$  is shone onto a surface, and the scattered light is collected by a detector. For scattered light whose electric field is represented by the complex function  $E_s(t)$ , the instantaneous intensity,  $I_s(t)$ , is given by

$$I_s(t) = \frac{c\epsilon_0}{2} E_s^*(t)E_s(t), \quad (2.1)$$

where  $c$  is the speed of light,  $\epsilon_0$  the dielectric constant, and  $E_s^*(t)$  the complex conjugate of  $E_s(t)$ . The measured intensity is obtained by averaging over the detector response time  $\tau_d$ . The detector signal,  $j_d(t)$ , is therefore proportional to this short-time average of the intensity,

$$j_d(t) \propto \frac{1}{2\tau_d} \int_{-\tau_d}^{\tau_d} I_s(t + \tau) d\tau. \quad (2.2)$$

For a typical detector (a photomultiplier tube, for instance), the response time,  $\tau_d$ , is on the order of  $1 \times 10^{-9}$  s, the obtained signal is therefore averaged over the rapid oscillations of the light wave, which is on the order of  $1 \times 10^{-14}$  s.

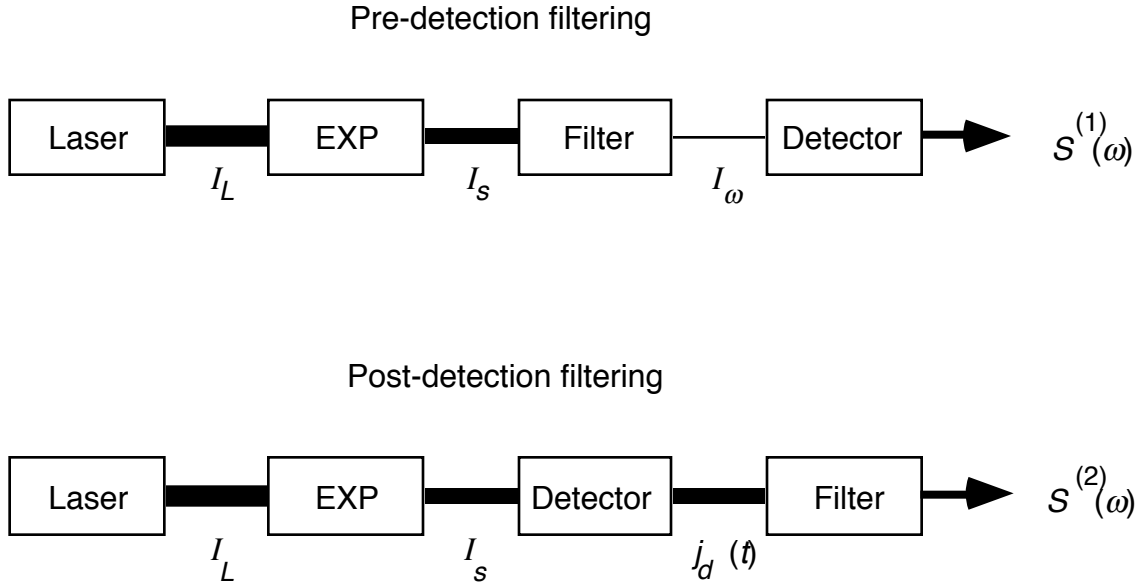


**Fig. 2.1** Pre- and post-detection filtering.  $I_L$  and  $I_s$  are the intensities of the probe and scattered laser light beams;  $I_\omega$  is the output mean power at  $\omega$  obtained using a filter of bandwidth  $\Delta\omega$ ;  $j_d(t)$  is the detector current;  $S^{(1)}(\omega)$  and  $S^{(2)}(\omega)$  are respectively the first and second order power spectrum.

Techniques for determining the scattered light spectrum fall into two categories: pre-detection and post-detection filtering (see Fig. 2.1). In the case of pre-detection filtering, the scattered light intensity,  $I_s(t)$ , is first spectrally filtered and then the spectral intensity,  $I_s(\omega)$ , measured. The detected signal yields the first-order power spectrum of the scattered field  $E_s(t)$  [Born and Wolf, 1980],

$$S^{(1)}(\omega) \equiv \int_{-\infty}^{\infty} E_s(\tau) e^{i\omega\tau} d\tau, \quad (2.3)$$

where  $T$  is the sampling time, the sharp brackets denote an ensemble average, and

$$E_s(\omega) = \int_{-\infty}^{\infty} E_s(\tau) e^{i\omega\tau} d\tau \quad (2.4)$$

is the Fourier transform of the scattered electric field. Notice that by the Fourier inversion formula,

$$E_s(\tau) = \int_{-\infty}^{\infty} E_s(\omega) e^{-i\omega\tau} d\omega. \quad (2.5)$$

On the other hand, the first-order or field correlation function,  $G^{(1)}(\tau)$ , is given by

$$G^{(1)}(\tau) \equiv \lim_{T \rightarrow \infty} \frac{1}{2T} \int_{-T}^T E_s^*(t) E_s(t + \tau) dt. \quad (2.6)$$

Using the ergodic theorem, the time average in (2.6) can be replaced by an ensemble average, yielding the relation,

$$G^{(1)}(\tau) = \langle E_s^*(0) E_s(\tau) \rangle. \quad (2.7)$$

Taking the Fourier transform of the above equation, comparing the result with Eq. (2.3), and then taking the inverse transform in Eq. (2.5), one finds that the measured optical power spectrum is related to the field correlation function by

$$S^{(1)}(\omega) = \int_{-\infty}^{\infty} G^{(1)}(\tau) e^{i\omega\tau} d\tau, \quad (2.8)$$

which is the optical equivalent of the Wiener-Khintchine theorem. [Khintchine, 1934, Wiener, 1930]

In post-detection filtering, the total intensity of the scattered light,  $j_d(t)$ , is detected before any filtering occurs. The detected intensity gives rise to a power spectrum of the form,

$$S_{j_d}(\omega) \equiv \lim_{T \rightarrow \infty} \frac{1}{2T} \langle j_d^*(\omega) j_d(\omega) \rangle, \quad (2.9)$$

where  $j_d(\omega)$  is the Fourier transform of  $j_d(t)$ , defined in Eq. (2.2). As in the case of pre-detection filtering, this spectrum can be related to an optical correlation function. Let us examine the intensity correlation of the scattered light, given by

$$G^{(2)}(\tau) = \lim_{T \rightarrow \infty} \frac{1}{2T} \int_{-T}^T I_s^*(t) I_s(t + \tau) dt. \quad (2.10)$$

Again evoking the ergodic theorem,  $G^{(2)}(\tau)$  can be written as

$$G^{(2)}(\tau) = \langle I_s^*(0) I_s(\tau) \rangle \quad (2.11)$$

Since  $j_d(t)$  is a linear functional of  $I_s(t)$ , one finds, upon applying the previously derived Wiener-Khintchine theorem, that the optical power spectrum is proportional to the intensity correlation function,

$$S_{j_d}(\omega) \propto \int_{-\infty}^{\infty} G^{(2)}(\tau) e^{i\omega\tau} d\tau. \quad (2.12)$$

This detected spectrum is therefore also proportional to the second-order power spectrum of the scattered light, defined as

$$S^{(2)}(\omega) \equiv \lim_{T \rightarrow \infty} \frac{1}{2T} \langle I_s^*(\omega) I_s(\omega) \rangle. \quad (2.13)$$

## 2.2 Hydrodynamic Fluctuations and Spectral Resolution

Before we can apply optical techniques to the study of fluctuations at a liquid-vapor interface, it is necessary to determine the relationship between hydrodynamic fluctuations and the optical correlation functions discussed in the previous section. Let us now consider in some detail an incident light field of the form

$$E_L(t) = A_L e^{-i\omega_L t + i\psi(t)}, \quad (2.14)$$

where  $A_L$  is the amplitude,  $\omega_L$  the frequency, and  $\psi(t)$  a slowly varying random function representing the fluctuating phase of the light. When this light is incident upon a liquid-vapor interface, it is scattered by surface roughness caused arising from hydrodynamic fluctuations. The scattered light can be written in the form

$$E_S(t) = f(t) A_L e^{-i\omega_L t + i\psi(t)}, \quad (2.15)$$

where  $f(t)$  is a complex stochastic quantity representing the hydrodynamic fluctuations in the scattering medium.

Substituting Eq. (2.15) into (2.7), the field correlation function is found to depend on the hydrodynamic and phase fluctuations of the incident light source in the following manner,

$$G^{(1)}(\tau) \propto \langle f^*(0) f(\tau) \rangle \langle e^{-i[\psi(0) + \psi(\tau)]} \rangle e^{-i\omega_L \tau}. \quad (2.16)$$

Since the power spectrum of the scattered light, in the case of pre-detection filtering, is the Fourier transform of the above correlation function (see Eq. (2.8)), Eq. (2.16) indicates this spectrum is in part determined by the phase fluctuations of the incident field. Thus, when the spectral width of the incident field is larger than the width associated with the scattering process, the field correlation function, and, consequently, the optical spectrum are dominated by the fluctuations in  $\psi(t)$ . The spectral resolution of conventional pre-detection filtering techniques is further limited by the filtering process itself. The frequency resolution of a filter is increased by narrowing its passband width, which correspondingly reduces the intensity of the signal. The resulting lowered signal-to-noise ratio may limit the spectral resolution even before phase

fluctuations of the incident light play a role. In practice, the limit of pre-detection filtering is on the order of a few MHz for interferometers. [Demtroder, 1982]

The intensity correlation function, in contrast, does not depend on the phase fluctuations of the incident light, but only on the hydrodynamic fluctuations at the interface. Substituting Eq. (2.15) into (2.11), one finds

$$G^{(2)}(\tau) \propto \langle f^*(0)f(0)f^*(\tau) \rangle. \quad (2.17)$$

In post-detection filtering, the detected spectrum of the scattered light is proportional to the Fourier transform of the intensity correlation. This Fourier transform is itself equal to the second-order power spectrum  $S^{(2)}(\omega)$  (see Eqs. (2.12) and (2.13)). It is thus evident from the above equation that the phase fluctuations of the incident field do not contribute to spectra detected in this manner. Unlike the case of pre-detection filtering, the ultimate spectral resolution in the post-detection case is limited neither by the spectral width of the incident light, nor by the passband width of the filter, but by the sampling time and stability of the apparatus. These limitations will be discussed in Section 2.5.

## 2.3 Homodyne and Heterodyne Detection

We have demonstrated the superiority of post-detection over pre-detection filtering in obtaining power spectra with high spectral resolution. In this section, two closely related detection techniques, homodyne and heterodyne detection are presented. Both of these methods utilize post-detection filtering and light beating spectroscopy.

Light beating spectroscopy [Cummins and Swinney, 1970] involves the mixing of two narrow-band optical components, producing a beat signal at the difference frequency. For beating to occur, the two components must be coherent and have good spatial overlap. In the homodyne or self-beating technique, light scattered from a liquid-vapor interface beats with its various spectral components. The detected signal,  $j_d(t)$ , gives rise to a spectrum which is proportional to the intensity correlation function, as in Eq. (2.17). Assuming hydrodynamic fluctuations to be random Gaussian processes, [Mandel, 1963] the second-order correlation function can then be written as

$$G^{(2)}(\tau) \propto \langle f^*(0)f(0) \rangle^2 + \left| \langle f^*(0)f(\tau) \rangle \right|^2. \quad (2.18)$$

In this case, the Fourier transform of Eq. (2.18) gives the second-order power spectrum. The first term produces a delta function at zero frequency, and represents the dc component of the spectrum. In the experiments we will be discussing, the correlation function  $\langle f^*(0)f(\tau) \rangle$  has a simple exponential dependence. The resulting transform thus gives a Lorentzian. Although homodyne detection has high spectral resolution, one cannot directly control the intensity of the beat signal, which can sometimes be too low to overcome the detector noise. [Arecchi, 1965]

This problem can, however, be overcome by spatially mixing the scattered light with a local oscillator, and detecting the beat signal between them. Such a procedure is utilized in heterodyne detection techniques, where the local oscillator allows one to control the intensity level of the beat signal. Consider a local oscillator coherent with the incident laser but frequency-shifted by an amount  $\omega_{LO}$ ,

$$E_{LO}(t) = A_{LO} e^{-i(\omega_L + \omega_{LO})t + i\psi(t)}. \quad (2.19)$$

The superposition of this field with the scattered light field given in Eq. (2.15) results in an instantaneous intensity,  $I_{S+LO}(t)$ , given by

$$\begin{aligned} I_{S+LO}(t) &= \frac{c\epsilon_0}{2} |E_S(t) + E_{LO}(t)|^2 \\ &= I_S(t) + I_{LO}(t) + \frac{c\epsilon_0}{2} [E_S^*(t)E_{LO}(t) + E_{LO}^*(t)E_S(t)]. \end{aligned} \quad (2.20)$$

Calculation of the intensity correlation function of the beat signal,  $\langle I_{S+LO}(0)I_{S+LO}(\tau) \rangle$ , thus involves sixteen terms. Ten of these terms contain the factor  $e^{-i\omega t}$ , average to zero. If the intensity of the local oscillator is much greater than that of the scattered light, and the time-independent terms are neglected, the intensity correlation function further reduces to

$$G^{(2)}(\tau) = \frac{c^2\epsilon_0^2}{4} [\langle E_S^*(0)E_{LO}(0)E_{LO}^*(\tau)E_S(\tau) \rangle + \text{c.c.}]. \quad (2.21)$$

Substituting Eqs. (2.15) and (2.19) for the fields in (2.21), one obtains

$$G^{(2)}(\tau) = \frac{c^2\epsilon_0^2}{4} |A_L|^2 |A_{LO}|^2 [\langle f^*(0)f(\tau) \rangle e^{i\omega_{LO}\tau} + \text{c.c.}]. \quad (2.22)$$

Since the intensity correlation function and second order power spectrum form a transform pair, Eq. (2.22) yields the power spectrum,

$$S^{(2)}(\omega) = \frac{c^2\epsilon_0^2}{4} |A_L|^2 |A_{LO}|^2 [S_f(\omega - \omega_{LO}) + S_f(-\omega - \omega_{LO})], \quad (2.23)$$

where  $S_f(\omega)$  is the power spectrum of the stochastic hydrodynamic fluctuations,

$$S_f(\omega) = \int_{-\infty}^{\infty} \langle f^*(0)f(\tau) \rangle e^{i\omega\tau} d\tau. \quad (2.24)$$

In Section 2.1, we demonstrated the proportionality of the detected power spectrum,  $S_{j_d}(\omega)$ , and the second-order power spectrum (see Eq. (2.12)). Using

this fact, we finally obtain the relationship between the detected spectrum and the hydrodynamic fluctuations,

$$S_{j_d}(\omega) \propto |A_{LO}|^2 [S_f(\omega - \omega_{LO}) + S_f(-\omega - \omega_{LO})]. \quad (2.25)$$

This equation indicates that, as for the case of homodyne detection, the phase fluctuations of the incident light cancel out in the heterodyne scheme. In addition, in contrast to the homodyne case, the intensity of the beat signal can now be controlled by adjusting the intensity of a local oscillator.

For a local oscillator whose frequency is the same as that of the incident beam ( $\omega_{LO}=0$ ), the power spectrum of the detected signal in Eq. (2.25) becomes

$$S_{j_d}(\omega) \propto |A_{LO}|^2 [S_f(\omega) + S_f(-\omega)]. \quad (2.26)$$

The detected spectrum thus represents the folded spectrum (folded at zero frequency) of the hydrodynamic fluctuations; the power spectrum of the fluctuations for positive and negative frequencies are superimposed. When heterodyne spectroscopy is used to study equilibrium interfacial fluctuations,  $S_f(\omega)$  is even in  $\omega$ . Such a superposition then leads to the doubling of the spectral intensity, without affecting the intrinsic spectral distribution. This is not, however, true for a system out of equilibrium, where  $S_f(\omega)$  and  $S_f(-\omega)$  are different. [Desai and Grant, 1986, Grant and Desai, 1983] The study of nonequilibrium systems thus requires a local oscillator having a non-zero frequency shift,  $\omega_{LO} \neq 0$ . In general, the optical frequency shift is determined by the spectral range of the particular application. Using a local oscillator with a non-zero shift also allows one to examine fluctuations at very low frequencies. Such signals are ordinarily filtered out or distorted by high-pass filters used to block the dc component of the signal. The advantages associated with a local

oscillator of non-zero frequency shift will be important in the applications discussed in sections 2.6 and 2.7.

The first application of heterodyne spectroscopy to the study of hydrodynamic fluctuations was carried out by Lastovka and Benedek in 1966. [Lastovka, 1966] In these experiments, the local oscillator was supplied by stray light scattered off both impurities in the scattering medium and the optical components. Although 'alignment' of the local oscillator is, in this case, automatic, one cannot control the oscillator intensity. In a more recently developed technique, the local oscillator is created by a diffraction grating. [Hård, Hamnerius, *et al.*, 1976, Shih, 1984] This is currently the most widely used method of generating a local oscillator. While such a technique allows for control of local oscillator intensity, the scattering angles which can be probed are limited by the ruling of the grating, and the frequency of the oscillator cannot be easily adjusted.

Upon detection, the beat signal can either be processed in the time domain to obtain the intensity correlation function, or in the frequency domain to obtain the power spectrum. Thus, both spectrum analyzer and autocorrelators are generally used in analyzing heterodyne data.

We have developed a Fourier transform heterodyne spectroscopy technique with high spectral resolution which is simpler and more direct than conventional techniques. Our technique requires neither spectrum analyzer nor autocorrelator, and allows for the continuous scanning of scattering angle as well as the easy adjustment of local oscillator frequency. The details of this technique are presented in the following section.

## 2.4 Optical Setup

Given are two different versions of the Fourier transform heterodyne spectroscopy setup: the post-sample mixing and pre-sample mixing schemes are depicted schematically shown in Figs. 2.2 (a) and 2.2 (b). Since the underlying principles are the same for both schemes, we use the post-detection scheme to illustrate the basis for this technique in the remainder of this section. A collimated 4 mW multimode He–Ne laser beam is used as the light source. The local oscillator is produced by splitting this beam in two with a beamsplitter [Chung, Lee, *et al.*, 1988, Mazur and Chung, 1987]: part of the beam serves as a local oscillator, while the remainder, the main beam, illuminates the scattering volume. This method allows for better control of the properties (intensity, polarization, frequency, collimation) of the local oscillator than is possible with a diffraction grating generated oscillator.

In our experiments, the optimal frequency shift for the local oscillator is around 5 kHz. This shift can be obtained by acousto-optic modulation. [Mazur and Chung, 1987] In this method, an acousto-optic crystal is driven at a desired shift frequency and the local oscillator beam is Bragg scattered off the standing waves created inside the crystal. The resulting frequencies of the two first-order scattered spots are thus upshifted and downshifted by the driving frequency. To ensure good spatial separation of the first-order and zeroth-order beams, two acousto-optic modulators to obtain this small frequency shifts. The local oscillator beam is first incident upon an acousto-optic crystal, driven at 40 MHz by a radio-frequency (rf) signal generator. The upshifted component from this crystal serves as input to a second crystal, driven at 40.005 MHz. The downshifted component from the second crystal then gives the local oscillator a net frequency shift of 5 kHz from the main beam.

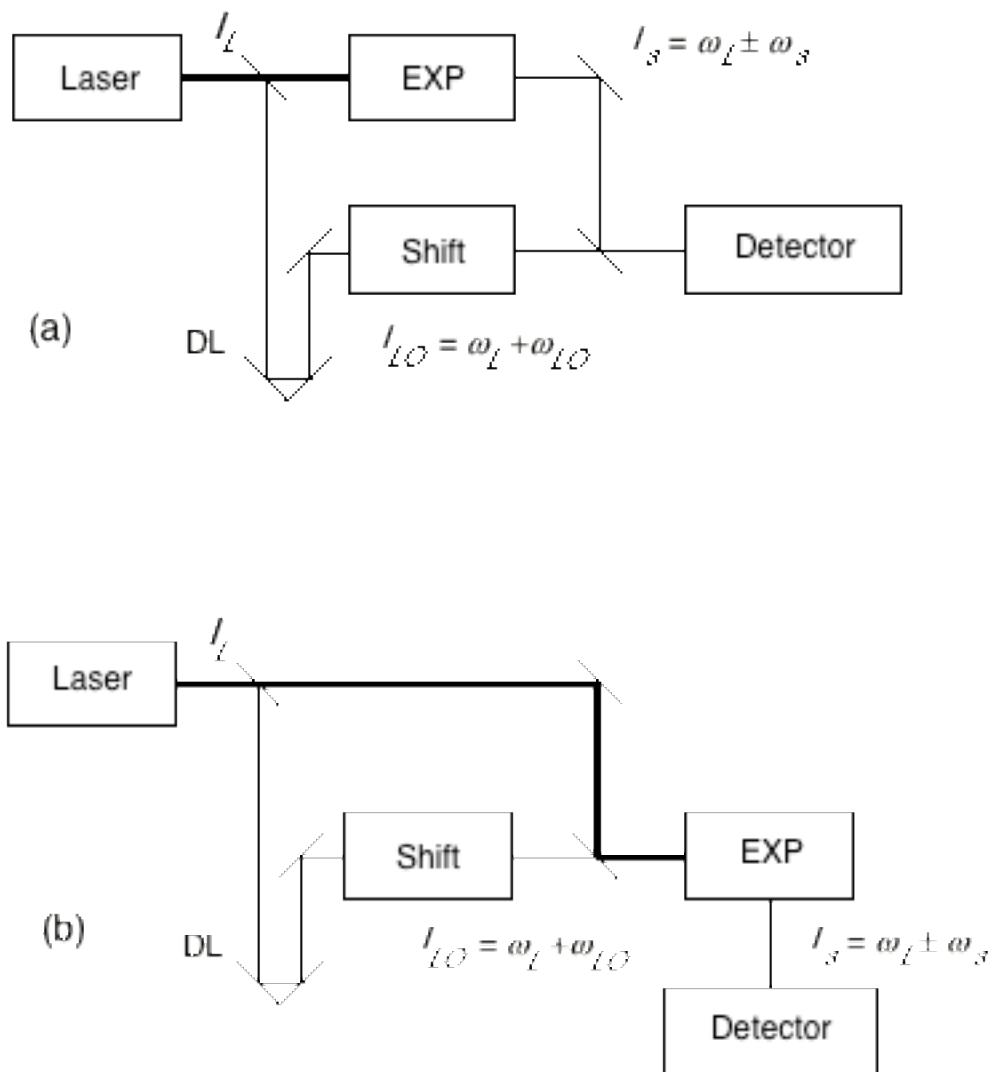


**Fig. 2.2** Pre- and post sample mixing configurations. The incident laser beam ( $I_L$ ) of frequency  $\omega_L$  is split into a main ( $I_M$ ) and local oscillator beam. The local oscillator beam ( $I_{LO}$ ) is frequency -shifted by  $\omega_{LO}$ . In (a), the main beam is incident on the scattering sample (EXP) and the scattered beam ( $I_s$ ) is combined with the local oscillator beam; in (b), the main and local oscillator beam are mixed before hitting the scattering sample. The beat signal of the scattered light and the local oscillator is then detected. DL – delay line;  $\omega_s$  – scattering frequency.

Alternatively, the frequency shift can be obtained by reflecting the local oscillator beam off a moving mirror. The Doppler shift of the reflected beam is given by

$$\Delta f = 2 \frac{v}{\lambda}, \quad (2.27)$$

where  $v$  is the velocity component of the mirror parallel to the incident beam, and  $\lambda$  the wavelength of the beam. For a He–Ne laser ( $\lambda = 632.8$  nm), a frequency shift of 5 kHz requires a mirror speed of 1.6 mm/s. Since the typical coherence length of an unstabilized He–Ne laser is about 0.3 m, one can sample the detector signal for up to 20 s in a single pass of the mirror. We have tested this scheme, and have found the resulting resolution to be limited by the stability of the moving mechanism. Spectra obtained using acousto-optic modulation have a higher spectral resolution; this modulation scheme is therefore utilized in our Fourier transform heterodyne spectroscopy setup.

The main beam illuminates the scattering volume, and the scattering angle is defined by a pinhole. The scattered and local oscillator beams are recombined using a beamsplitter. The two beams are aligned carefully to ensure good spatial overlap, as is necessary for the production of a strong beat signal. To obtain efficient mixing of the beams, it is also essential that the two be coherent at the detector. To this end, the delay line in Fig. 2.2 (a) allows for adjustment of the beam pathlengths. As we discussed, the typical coherence length of a He–Ne laser is about 0.3 m; maintaining the coherence of the two beams is thus a fairly easy task.

The beat signal between the scattered light and the local oscillator is recorded with a photomultiplier tube. The signal is amplified and digitized at a

20 kHz sampling rate by an analog–digital computer interface<sup>1</sup>, and the full signal trace is stored in the memory of a microcomputer<sup>2</sup>. The correlation function can then be obtained directly from the digitized data points, and the frequency spectrum of the digitized signal obtained using a fast Hartley transform. This transform is equivalent to a fast Fourier transform, but requires only half as many operations. [Bracewell, 1965] Our data acquisition system allows one to obtain both correlation functions and power spectra without using an autocorrelator or spectrum analyzer. In addition, this setup is more versatile and cost effective than conventional ones.

## 2.5 Experimental Limits of FTHS

We demonstrated in Section 2.3, that the spectral resolution of heterodyne spectroscopy is independent of the phase fluctuations of the incident beam. In this section, we examine the experimental limits of our Fourier transform heterodyne spectroscopy setup, and how they affect the spectral resolution.

In our setup, a detector signal  $j_d(t)$  is sampled for a period of  $T$  (the sampling time), and the digitized signal is Fourier transformed to obtain the spectrum. According to sampling theory, the frequency interval between adjacent spectral points,  $\delta f_s$ , is given by

$$\delta f_s = \frac{1}{T}. \quad (2.28)$$

---

<sup>1</sup>MacADIOS II, GW Instruments.

<sup>2</sup>Macintosh II, Apple Computers.

For a sampling time of four hours,  $\delta f_s$  is  $70 \mu\text{Hz}$ , which, for a He–Ne laser, corresponds to the Doppler shift resulting from a speed of  $0.2 \text{ \AA}/\text{s}$ . Although Eq. (2.28) indicates that the resolution can be made infinitesimally small for an infinitely long sampling time, in reality, it is limited by the electronic and optical pathlength stability of the setup.

Fluctuations in the frequency shift of the local oscillator,  $\delta f_{LO}$ , constitute the major source of instabilities in our present setup. Since the frequency shift is determined by the frequency difference between the two rf carrier frequencies which drive the acousto-optic modulators, fluctuations,  $\delta f_{LO}$ , results from the electronic drifts of these drivers. The drifts arise primarily from temperature fluctuations, and one can easily achieve a carrier frequency stability of 100 Hz for a typical 40 MHz rf driver. Because it is the frequency difference which is important in our experiment, the electronic stability can be improved by placing both rf drivers into the same environment. The two drivers then drift by the same amount, and the frequency difference is unaffected. The frequency drift,  $\delta f_{LO}$ , is found from direct measurements of the electronic beat signal to be about 0.1 Hz. This limit can be greatly reduced by locking the two drivers to a single oven-controlled time base. With locked drivers, our measurements show a dramatic reduction of the frequency drift; in this case,  $\delta f_{LO}$  is found to be about  $1 \mu\text{Hz}$ . Another source of electronic instability is the fluctuations in the digitization clock-rate,  $\delta f_{clock}$ . The analog-to-digital computer interface used gives a clock accuracy of 0.2 nHz, indicating that the electronic stability of our setup is practically determined by the stability of the rf drivers.

Fluctuations in the optical pathlength,  $\delta f_o$ , can be caused by changes in the index of refraction of air, mechanical perturbations of the optical elements due to temperature fluctuations, and acoustic noise in the environment. For a

temperature increase of 1 °C/hour, a 1-m long optical pathlength contracts at a speed of about 2.5 Å/s owing to changes in the refractive index of air. This temperature increase also leads to thermal expansion of the carbon steel optical table, at a rate of about 0.5 Å/s. Temperature fluctuations,  $\delta f_{temp}$ , therefore limit the resolution to about 300  $\mu$ Hz. A rough estimate of the effect of a 100-Hz sound wave of 50 dB on a typical aluminum mount, 1 cm<sup>2</sup> in square cross-sectional area and 5 cm in height, yields a lateral speed of the top surface of less than 1 Å/s. The resolution limit resulting from acoustic noise,  $\delta f_{noise}$ , is about 30  $\mu$ Hz. In our setup, the resolution limit is dictated not by the actual pathlength, but pathlength difference between the main and local oscillator beams. The above discussion then gives the upper limits of  $\delta f_{temp}$  and  $\delta f_{noise}$ ; the effective limits imposed by temperature fluctuations and noise are generally much smaller.

The instrumental resolution of the present setup was determined experimentally by mixing the local oscillator directly with the main laser beam, as shown in Fig. 2.3. The local oscillator was frequency-shifted by a combination of two acousto-optic modulators (see Section 2.4). The modulators were driven by two rf drivers, and the carrier frequencies were in the 20–40 MHz range, with a frequency difference of 5 kHz.

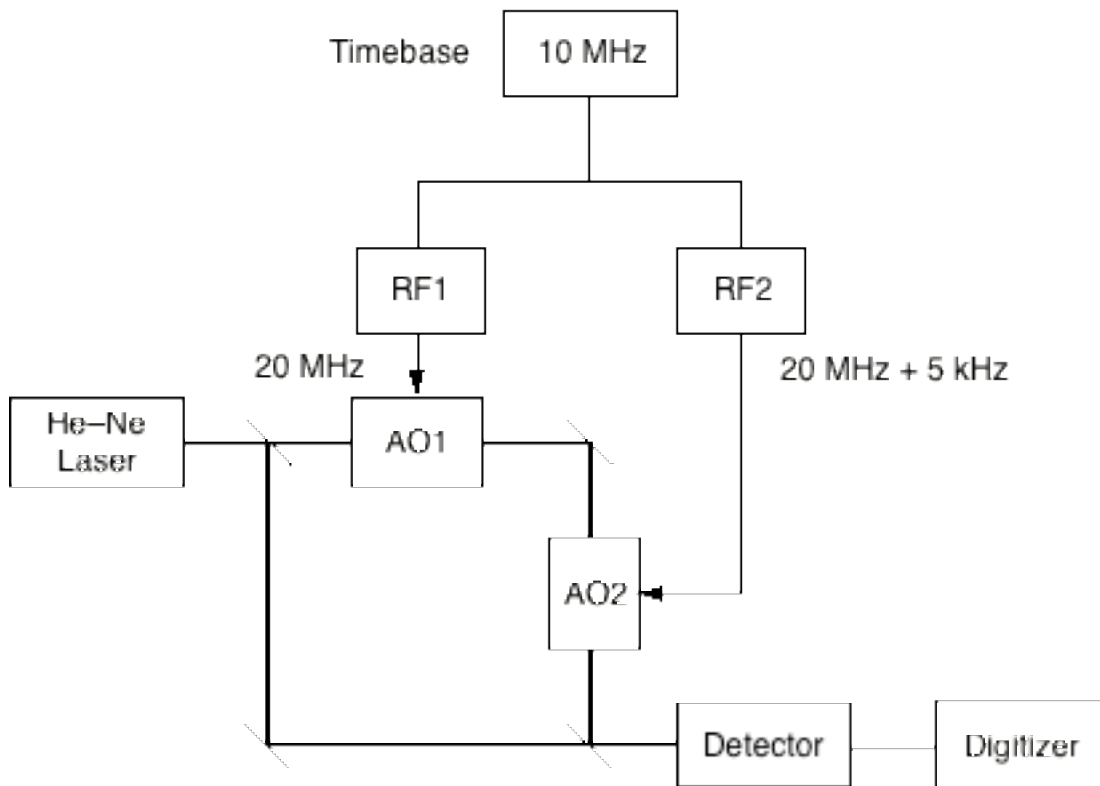


**Fig. 2.3** Schematic diagram of the experimental setup for the measurement of the instrumental resolution. Light from a He-Ne laser is split into a main beam and a local oscillator beam. The local oscillator beam is frequency-shifted by a set of two acousto-optic modulators (AO1, AO2), driven by two rf signal generators (RF1, RF2). The rf signal generators are locked to the same oven-controlled timebase to improve frequency stabilities of the local oscillator beam. The beating signal between the main and local oscillator beams is then detected and digitized.

When the two modulators were driven by two independent rf drivers<sup>3</sup>, the resolution was found to decrease with increasing sampling time, as expected from Eq. (2.28). A minimum resolution of about 150 mHz was achieved. A loss in resolution was noted for sampling times in excess of 60 s (open squares in Fig. 2.4). By comparing the optical beat spectrum with the spectrum obtained by electronically beating the two rf signals, it was found that the resolution limit

---

<sup>3</sup>ME-40, IntraAction Corporation.

arose from by instabilities in the carrier frequencies (diagonal crosses in Fig. 2.4). When the independent rf drivers were replaced by two locked to the same oven-controlled time base<sup>4</sup>, the resolution was improved by a factor of close to one hundred. As can be seen in Fig. 2.4, the rf resolution (vertical crosses) follows Eq. (2.28) down to 140  $\mu\text{Hz}$ , while the optical resolution (filled squares) begins to show deviations at about 400  $\mu\text{Hz}$ . The deviation in optical resolution most likely results from optical pathlength fluctuations over the sampling period. The highest instrumental resolution of the present setup, 200  $\mu\text{Hz}$ , was obtained with a 1.5-hour sampling time.

Above we have discussed the lower spectral limit of our FTHS technique. To explore its upper limit, let us consider a detector signal  $j_d(t)$  sampled at a sampling frequency  $f_s$  (the inverse of the interval between adjacent sampling points,  $\delta t_s$ ). The free spectral range  $F$  of the spectrum obtained by Fourier transforming the digitized signal is given by

$$F = \frac{1}{2\delta t_s} = \frac{1}{2}f_s. \quad (2.29)$$

In our experiments, we have used a variety of sampling frequencies, between 1 Hz and 20 kHz, resulting in a spectral range from 0.5 Hz to 10 kHz.

The highest free spectral range that can be achieved with our present setup is 50 kHz, owing to the 100 kHz maximal sampling rate of our signal digitizer. In general, the upper limit of the range is determined by either the detector response time or the speed of the signal digitizer. In practice, with a 1-ns response time and a fast transient digitizer, the spectral range can be extended

---

<sup>4</sup>3325-B frequency synthesizers, Hewlett Packard.

to the GHz regime. With a streak camera, this range can be further extended by at least two orders of magnitude.

A final practical limit must be considered – the computation time necessary for the analysis of the digitized signal. The total number of data points,  $N$ , is given by the product of the sampling time and sampling frequency,

$$N = T f_s, \quad (2.30)$$

while the transform time grows as  $N \log_2 N$ . With a Macintosh II personal computer, the time required to obtain the power spectrum of  $2^{16}$  data points is

|                   |   | Limiting factors                                  | Current limit                           |            |
|-------------------|---|---|---|------------|
| Resolution limits | $\delta f_s = \frac{1}{T}$                                  | Sampling time (4 hours)                           | 70 $\mu$ Hz                             |            |
|                   | $\delta f_{LO}$   | $\delta f_{temp}$ Temperature drift (1K/hour)     | < 300 $\mu$ Hz                          |            |
|                   |   | $\delta f_{noise}$ Acoustic noise (100 Hz, 50 dB) | 30 $\mu$ Hz                             |            |
|                   |   | $\delta f_e$                                      | RF oscillator precision                 | 1 $\mu$ Hz |
|                   |   | $\delta f_{clock}$                                | Clock accuracy ( $2.5 \times 10^{-6}$ ) | 0.2 nHz    |
| Spectral range    | $\mathcal{F} = \frac{1}{2\Delta T} = \frac{N\delta f_s}{2}$ | Detector response time (< 1 ns)                   | > 1 GHz                                 |            |
| Computation time  | $N \log_2 N, N = T f_s$                                     | CPU/FPU ( $N = 2^{16}$ , Mac II)                  | 40 s                                    |            |

Table 2.1 Experimental range and limitations of the Fourier transform heterodyne spectroscopy technique.

about 40 s. This transform time can be reduced by using faster computers.

With sub-mHz instrumental resolution and GHz spectral range, the Fourier transform heterodyne spectroscopy technique has potential applications in many fields of research. In the following two sections, we examine how this technique can be applied to two very different fields of study.

## **2.6 Applications to Crystal Growth Measurements**

Because of both its ultrahigh spectral resolution and the shifting of the elastically scattered peak out of the low frequency range, Fourier transform heterodyne spectroscopy is a technique suitable for the study of processes involving very small frequency shifts. A possible application is the measurement of extremely small Doppler shifts. As an illustration, we used this technique to study crystal growth at an amorphous-crystalline silicon interface.

The crystallization of an isolated piece of amorphous silicon occurs through the random formation and subsequent growth of nucleation clusters. When a thin film of amorphous silicon is in direct contact with a substrate of crystalline silicon, however, the crystallization process becomes ordered, with the crystalline substrate providing the film with the necessary template. Crystallization then proceeds as a layer by layer conversion of silicon atoms from the amorphous to the crystalline phase. When a light beam is incident upon such a sample, part of it is reflected at the amorphous-crystalline interface because the two phases have different indices of refraction. As the amorphous silicon crystallizes, the amorphous-crystalline interface moves. Light reflected

from this moving interface is Doppler shifted, with a frequency shift given by Eq. (2.27). The resulting Doppler shift can be measured using our Fourier transform heterodyne spectroscopy, allowing one to infer the growth rate of the interface.

The silicon sample used in our experiment consists of a  $2 \times 2$  mm substrate of crystalline silicon(100) with a top layer of amorphous silicon, 300-nm thick, made by implantation of  $^{30}\text{Si}^+$ . The sample is placed on a heating unit<sup>5</sup> in open air with the amorphous layer facing vertically upward. The rate of crystallization, and hence the growth rate of the interface, can be varied by adjusting the temperature of the system. To achieve a growth rate large enough to detect, the sample must be heated to a temperature of over 800 K. At these high temperatures, air turbulence around the sample and reduced mechanical stability of the heating unit greatly lower the overall stability of the setup. It is therefore necessary to mix the main laser beam with the local oscillator before hitting the sample; otherwise good constant overlap of the two beams cannot be ensured.

The pre-sample mixing setup for crystal growth measurements is shown schematically in Fig. 2.5. The frequency shift in the local oscillator beam is provided by two acousto-optic modulators<sup>6</sup> driven at carrier frequencies of 20.000 MHz and 20.005 MHz by two stabilized frequency generators locked to the same oven-controlled time base.<sup>7</sup> To suppress reflection from the front surface (the interface between air and amorphous silicon), the incidence angle of

---

<sup>5</sup>The silicon sample and the temperature control unit were provided by Professor M. J. Aziz at Harvard University.

<sup>6</sup>AOM-40, IntraAction Corporation.

<sup>7</sup>Frequency synthesizer 3325-B, Hewlett-Packard.

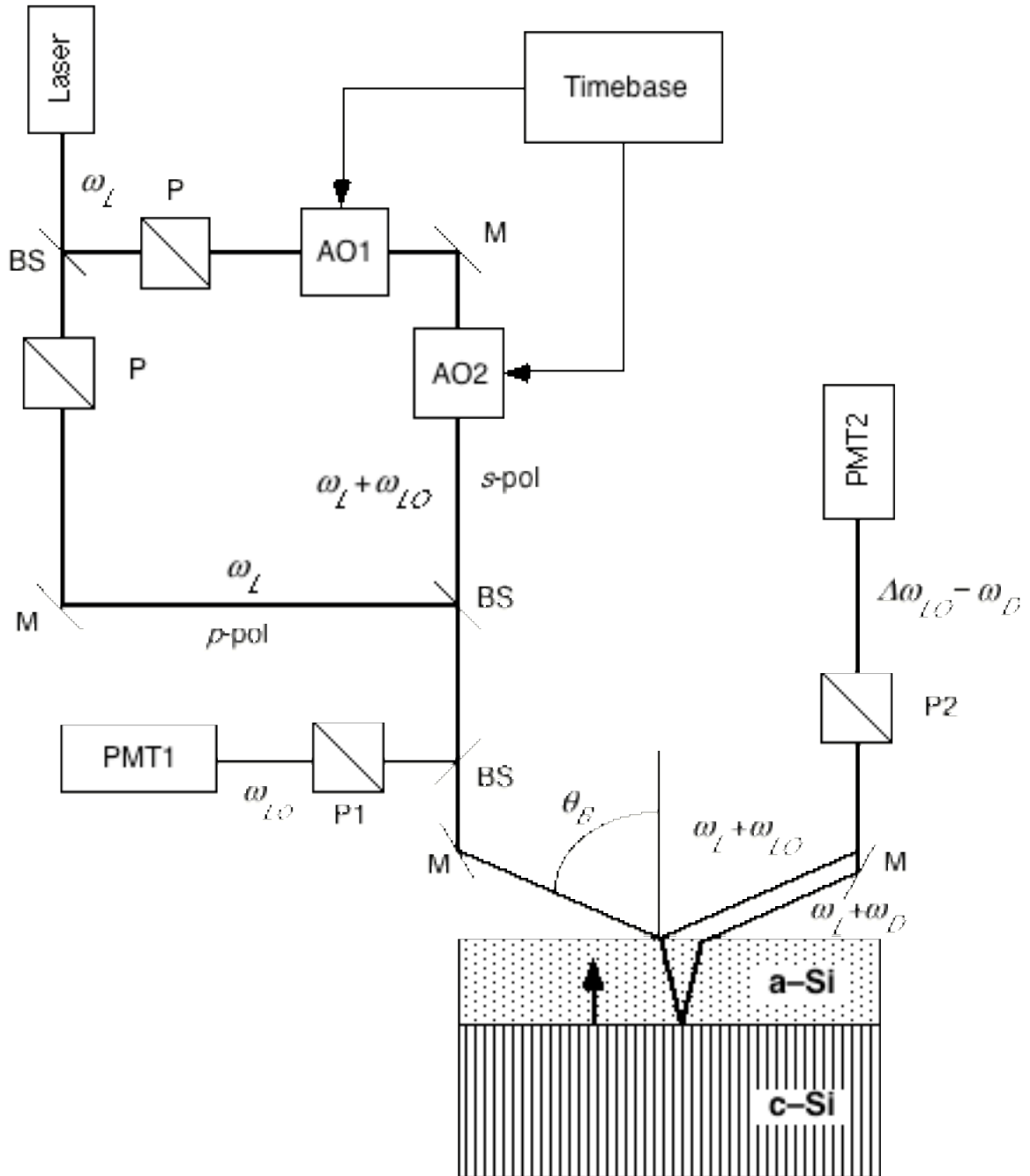


**Fig. 2.5** Experimental setup for measuring the Doppler shift from a growing amorphous-crystalline silicon interface. A p-polarized beam at angular frequency  $\omega_L$  and a s-polarized beam at  $\omega_L + \omega_{LO}$  are combined before they hit the silicon sample at Brewster angle  $\theta_B$ . The silicon sample consists of a crystalline silicon substrate (c-Si) and a 300-nm amorphous silicon layer (a-Si). PMT1 monitors the beat signal between the unshifted main beam and the local oscillator beam; PMT2 records the beat signal between the Doppler-shifted main beam and the local oscillator beam. Mixing of the orthogonally polarized main and local oscillator beams is facilitated by 45° polarizers (P1, P2). BS – beamsplitter; P – polarizer; M – mirror; AO – acousto-optic modulator.

the beams is kept near the Brewster angle. The Brewster angle is calculated using the real part of the index of refraction of amorphous silicon at the He-Ne laser wavelength of  $\lambda = 632.8$  nm,  $\text{Re}(n_{as})$ , given by [Olson and Roth, 1988] ,

$$\text{Re}(n_{as}) = 4.39 + 5 \times 10^{-4} T , \quad (2.31)$$

where  $T$  is the absolute temperature of the system. At 835 K,  $n_a = 4.81$  and ignoring s possible contribution arising from the presence of a surface layer of silicon oxide, the Brewster angle,  $\theta_B$ , is

$$\theta_B = \tan^{-1} \text{Re}(n_{as}) = 78.2^\circ . \quad (2.32)$$

At this incidence angle, the refraction angle is  $11.7^\circ$  and the change in the vertical component of the growth velocity is 2%. The main beam is  $p$ -polarized, and the local oscillator is  $s$ -polarized. In this polarization configuration, most of the local oscillator beam is reflected at the air-amorphous silicon interface, while most of the main beam penetrates the amorphous layer and is reflected at the amorphous-crystalline silicon interface. Since the main and local oscillator beams are perpendicularly polarized, a  $45^\circ$  polarizer is used to mix the two. The beat signals between the two beams are sampled by two photomultiplier tubes. One (PMT1 in Fig. 2.5) records the beat signal before the beams hit the sample, and provides a reference spectrum without any Doppler shifted peak. The other (PMT2 in Fig. 2.5) monitors the beat signal after the two beams hit the sample. The resulting spectrum is characterized by a Doppler shifted peak arising from the motion of the amorphous-crystalline interface.

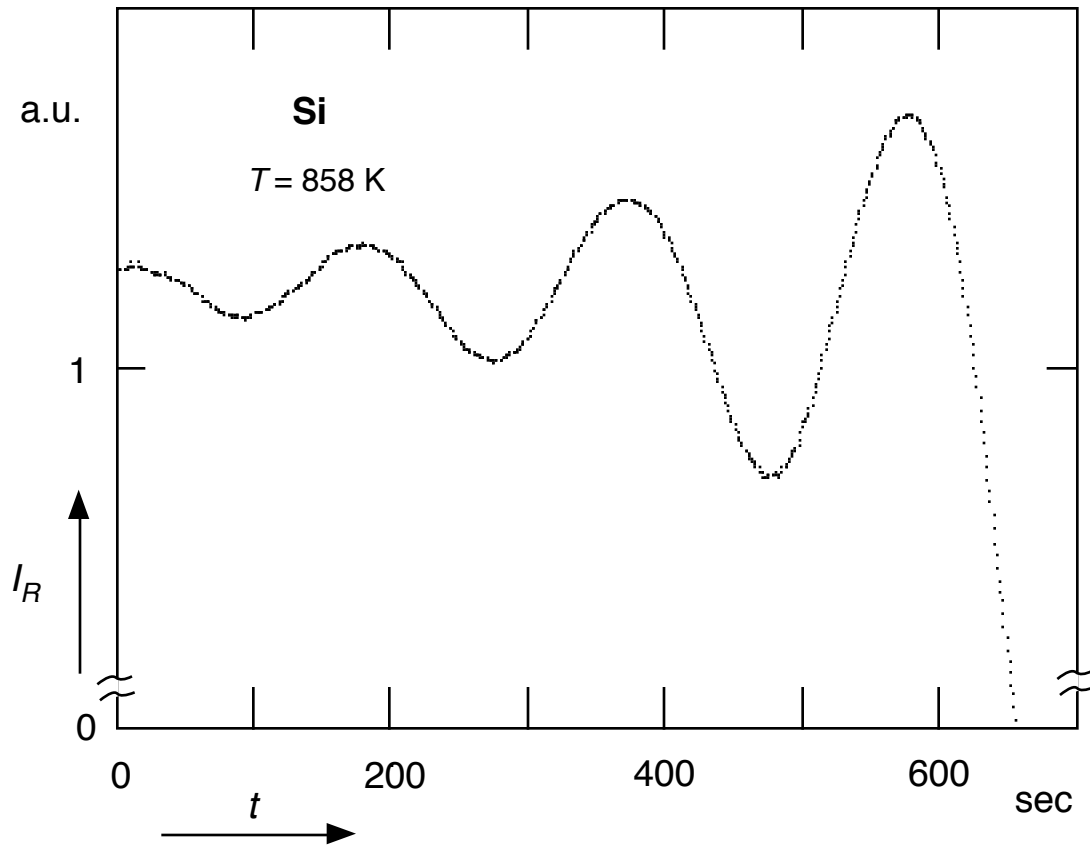


**Fig. 2.6** Time-resolved reflectivity measurement of a growing amorphous-crystalline silicon interface at 858 K. The ratio of the outputs from the two photomultipliers,  $I_R$ , is monitored with time  $t$ .

When the local oscillator beam blocked, our setup is identical to that for standard time-resolved reflectivity measurements. A trace of the time-resolved reflectivity obtained using this setup with the silicon sample heated to 858 K is shown in Fig. 2.6. Between successive maxima and minima in the trace, the amorphous film thickness decreases by  $n_{as}\lambda/4$ . One thus determines the growth rate to be 0.35 nm/s, which agrees with the published data of Olson and Roth. [Olson and Roth, 1988]

When the local oscillator beam is no longer blocked and is allowed to mix with the main beam, the power spectrum obtained after the two beams hit the sample shows a Doppler shifted peak. Figure 2.7 shows the spectrum for a silicon sample heated to 835 K. To obtain this spectrum, the signal was sampled for 14 minutes at a rate of 76.9 Hz; the points in the spectrum are then each separated by 1.2 mHz. Circles are data points from the Fourier transform, while the solid line is a visual aid. The large peak results from the beating of the main and local oscillator beams reflected at the air-amorphous silicon interface. The smaller peak is Doppler shifted by the motion of the amorphous-crystalline

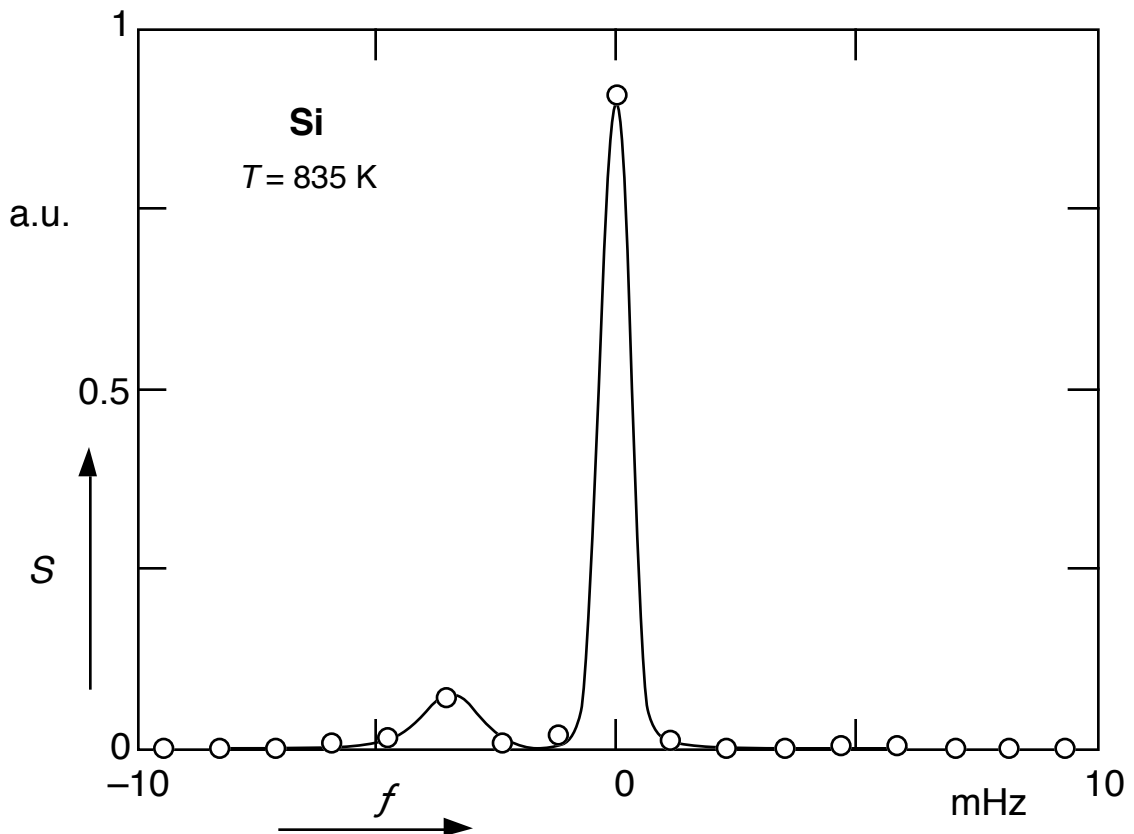


**Fig. 2.7** Spectrum of light reflected from a growing amorphous-crystalline silicon interface at 835 K. The small peak left of the large central one represents the Doppler shift due to the moving interface. The solid line through the data points is a guide to the eye.

interface. The Doppler shift, in this case, is 3 mHz, corresponding to a speed of about 0.2 nm/s. This agrees well with the results of our time-resolved reflectivity measurements and published data. [Olson and Roth, 1988]

With higher spectral resolution, one can, in principle, obtain the distribution of speeds over the sampled area from the broadening of the Doppler shifted peak (the shift reflects only the average speed). Since the current resolution of 1.2 mHz is almost two orders of magnitude above our instrumental limit, one should be able to obtain this information using the Fourier transform heterodyne spectroscopy technique. Since the resolution of such measurements is limited by the maximum sampling time (see Eq. (2.28)), longer measurements can be taken to increase the spectral resolution. For a fixed growth rate, longer measurement times require thicker samples; the resolution is therefore limited by the ratio of the amorphous layer thickness to the growth rate. One problem with increasing the layer thickness is, however, that amorphous silicon layer absorbs a significant amount of visible light. The imaginary index of refraction of amorphous silicon at the He-Ne wavelength is  $\text{Im}(n_{as}) = 0.61$ ; for a 300-nm thick layer, 97% of the light is absorbed. A sufficiently thin sample is thus necessary to obtain a reasonable signal. Signal attenuation can be drastically reduced if a different light frequency is used, or if one probes from the crystalline silicon side, which is far less absorptive with  $\text{Im}(n_s) = 0.018$ . Unfortunately, due to experimental and sample constraints, we were unable to test these ideas.

## 2.7 Application to Liquid Surface Studies

Fourier transform heterodyne spectroscopy can also be applied to the study of the dynamics at a liquid-vapor interface. Let us consider a light wave of

angular frequency  $\omega_L$  and wavevector  $\mathbf{k}'_L$  incident upon such an interface. For a perfectly flat boundary between two phases with different indices of refraction, the light beam is specularly reflected and refracted. A real liquid-vapor interface, however, is not perfectly flat. Thermal fluctuations give rise to small amplitude (less than 10 Å) surface waves of various wavelengths. The propagating surface modes correspond to gravity waves for long wavelengths and capillary waves for small wavelengths. The simple dispersion relation for these waves, which can be obtained from classical hydrodynamic theory [Landau and Lifshitz, 1959, Levich, 1962], is given by

$$\omega_{sw}^2 = gk_{sw} + \frac{\sigma}{\rho}k_{sw}^3, \quad (2.33)$$

with  $\omega_{sw}$  and  $k_{sw}$  the angular frequency and magnitude of the wavevector  $\mathbf{k}_{sw}$  of the surface waves,  $g$  the acceleration due to gravity, and  $\sigma$  and  $\rho$  the surface tension and density of the liquid phase. The existence of these waves roughens the interface and, as a result, leads to the inelastic scattering of the incident light.

Figure 2.8 schematically depicts a two-dimensional cross-section for such a scattering process. A surface wave with wavevector  $\mathbf{k}_{sw}$  and corresponding angular frequency  $\omega_{sw}$  traveling from left to right, scatters an incident light beam into two directions. Both momentum and energy are conserved, satisfying the conditions,

$$\mathbf{k}_{scatt} = \mathbf{k}_L \pm \mathbf{k}_{sw}, \quad (2.34)$$

$$f_{scatt} = f_L \pm f_{sw}, \quad (2.35)$$

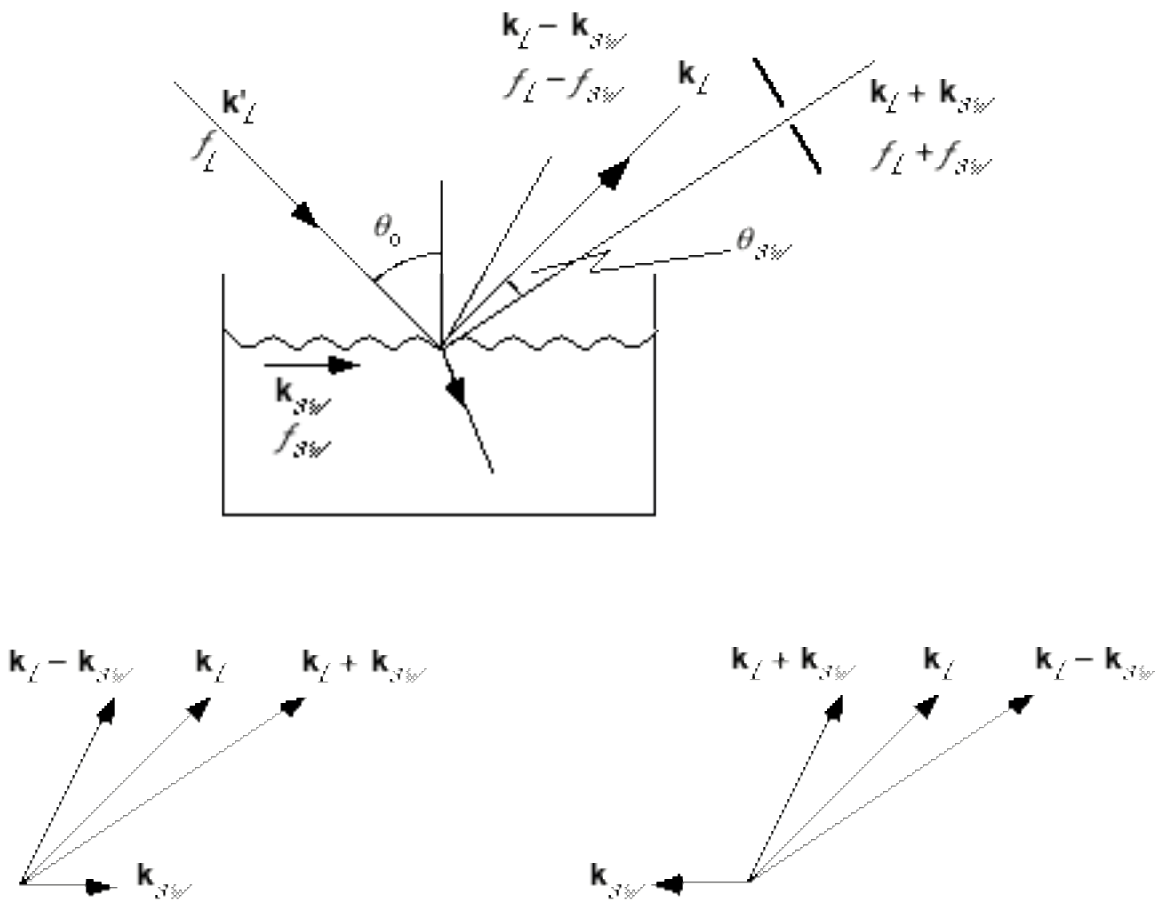


**Fig. 2.8** Optical geometry for inelastic light scattering caused by capillary waves at a liquid-vapor interface. A light beam of wavevector  $\mathbf{k}_L$  and frequency  $f_L$  is incident on the interface at an angle  $\theta_0$ . In addition to specular reflection and refraction in the bulk liquid, the incident beam is also scattered by capillary waves at the interface. Light can be scattered off in two directions by a capillary wave of wavevector  $\mathbf{k}_{sw}$  and frequency  $f_{sw}$ . The scattering angle  $\theta_{sw}$  of the inelastically scattered light is determined by the phase-matching condition of momentum conservation. The light scattered off the capillary wave described above at the scattered angle shown gives rise to an upshifted peak in the power spectrum. A capillary wave of the same wavelength but propagating in the opposite direction gives rise to a downshifted peak in the spectrum.

where  $(\mathbf{k}_{scatt}, f_{scatt})$ ,  $(\mathbf{k}_L, f_L)$ , and  $(\mathbf{k}_{sw}, f_{sw})$  are, respectively, the wavevectors and frequencies of the scattered light, reflected light, and surface waves. The plus and minus signs correspond, respectively, to the annihilation and creation of a surface wave of wavevector  $\mathbf{k}_{sw}$ . The scattering angle,  $\theta_{sw}$ , is given by the

phase-matching (momentum conservation) condition of Eq. (2.34). When the surface wavevector,  $\mathbf{k}_{sw}$ , is much smaller than that of the laser,  $\mathbf{k}_{laser}$ , the magnitudes of the incident and scattered wavevectors are approximately equal,

$$k_{scatt} \approx k_L. \quad (2.36)$$

This scattering angle and surface wavevector are then related by the formula,

$$k_{sw} = k_L [\sin(\theta_0 + \theta_{sw}) - \sin\theta_0] \approx k_L \theta_{sw} \cos\theta_0, \quad (2.37)$$

where  $\theta_0$  is the incident angle. In other words, for a scattering angle  $\theta_{sw}$  as shown in Fig. 2.8, the light scattered by a surface wave ( $\mathbf{k}_{sw}, f_{sw}$ ), travelling from left to right, has a wavevector-frequency pair given by  $(\mathbf{k}_L + \mathbf{k}_{sw}, f_L + f_{sw})$ . Since there is no preferred direction of travel for surface waves, waves traveling in the opposite direction exist as well. Light scattered by these waves ( $-\mathbf{k}_{sw}, f_{sw}$ ) also satisfies conservation of momentum and energy,

$$\mathbf{k}_{scatt} = \mathbf{k}_L \pm (-\mathbf{k}_{sw}), \quad (2.38)$$

$$f_{scatt} = f_L \pm (-f_{sw}). \quad (2.39)$$

Thus, for the same scattering angle  $\theta_{sw}$ , waves propagating from right to left give rise to scattered light having a wavevector-frequency pair  $(\mathbf{k}_L - \mathbf{k}_{sw}, f_L - f_{sw})$ . Hence, the frequency of the scattered light at an angle  $\theta_{sw}$  is either upshifted or downshifted by  $f_{sw}$ , depending on the direction of propagation of the wave. The spectrum of the scattered light therefore consists of three peaks: a central peak from elastic scattering, and two side peaks (Brillouin peaks) due to surface waves traveling in opposite directions.

Since beating is only sensitive to frequency differences, upshifted and downshifted peaks from counter-propagating waves superimpose and appear at

the same frequency using conventional heterodyne detection with an unshifted local oscillator (see Eq. (2.26)). Use of a frequency shifted local oscillator in our Fourier transform heterodyne spectroscopy technique therefore allows us to spectrally resolve surface waves propagating in opposite directions. For a frequency shift of  $f_{LO}$ , the scattering configuration in Fig. 2.8 results in two Brillouin peaks at frequencies  $f_{LO} - f_{sw}$  and  $f_{LO} + f_{sw}$ ; the former corresponds to waves traveling from the left, and the latter to waves from the right. To demonstrate this feature, surface waves of 1 kHz were mechanically induced at a water-air interface using a wire attached to a speaker, and the local oscillator was shifted by 5 kHz. The transducer was placed first to the left of the probe spot, and then to the right; Figures 2.9 (a) and 2.9 (b) show the resulting spectra. A sharp peak appears at either 4 or 6 kHz, depending on the relative position of the transducer. Additional peaks at 1 and 5 kHz result from the mixing of stray light with the scattered signal and local oscillator, respectively. In the following chapters, the capability of our Fourier transform heterodyne spectroscopy technique to spectrally resolve surface waves traveling in opposite directions is exploited to study the behaviors and properties capillary waves at liquid-vapor interfaces.

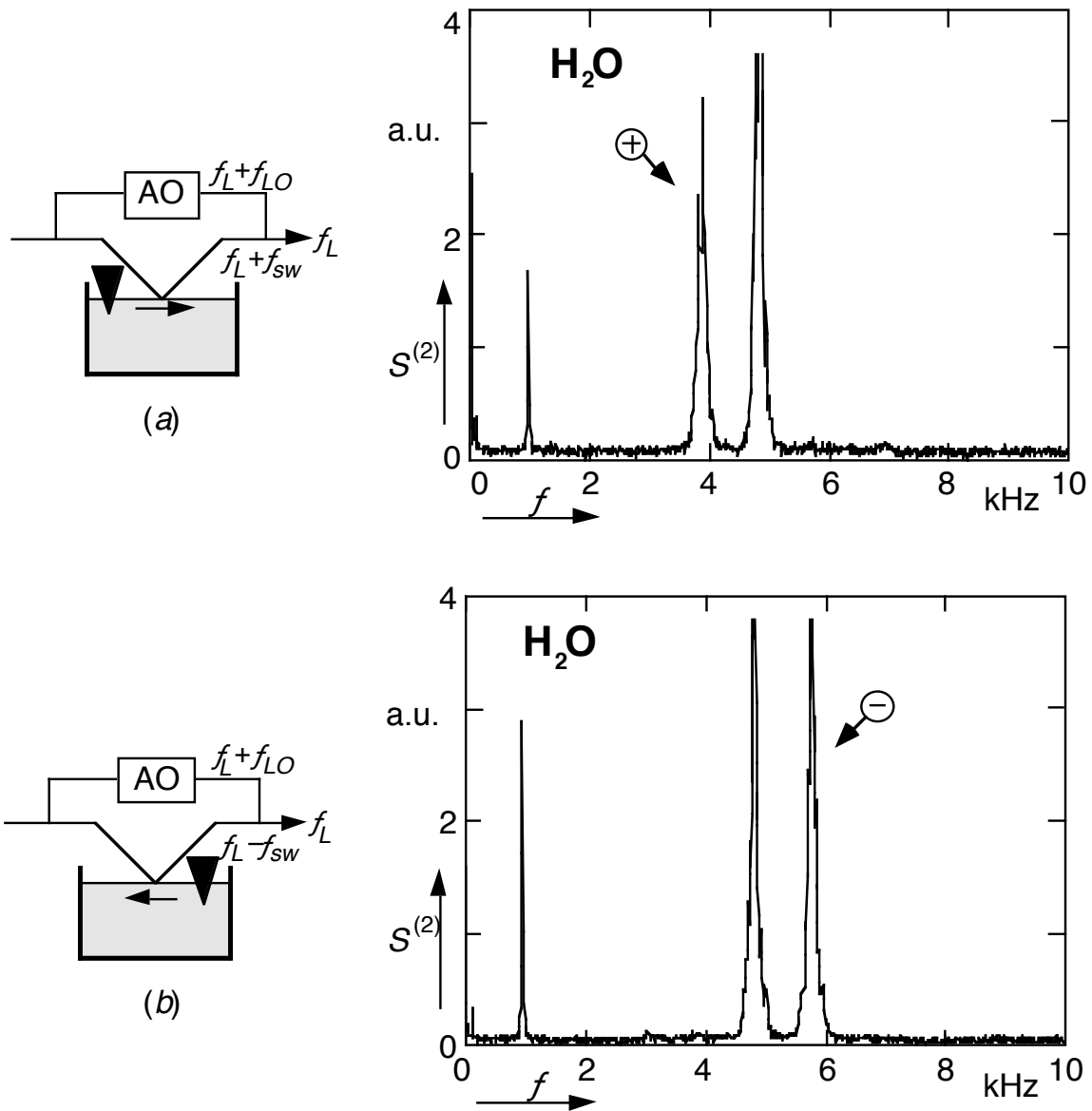


**Fig. 2.9** Power spectrum of induced capillary waves. Unidirectional capillary waves of  $f_{sw} = 1$  kHz are induced at a water-air interface by a transducer (black triangle) as shown in the diagrams on the left. The direction of propagation of the induced wave can be changed by altering the position of the transducer relative to the probe spot. In both cases, the heterodyne spectrum shows only one capillary wave peak. The configuration in (a) results in a downshifted heterodyne peak, while the one in (b) results in an upshifted peak. Note that the homodyne peaks, which correspond to the beating between  $f_L$  and  $f_L \pm f_{sw}$ , appear at  $f_{sw}$ .

## References

- Arecchi, F.T., *Phys. Rev. Lett.*, **15**, 912 (1965).
- Born, M. and Wolf, E., *Principles of Optics* (Pergamon Press, London, 1980).
- Bracewell, R.N., *The Fourier Transform and its applications* (McGraw-Hill, New York, 1965).
- Brillouin, L., *Ann. Phys. (Paris)*, **17**, 88 (1922).
- Chung, D.S., Lee, K.Y.C. and Mazur, E., *Int. J. Thermophysics*, **9**, 729 (1988).
- Cummins, H.Z. and Swinney, H.L. in *Progress in Optics*, edited by E. Wolf, 133 (North-Holland, Amsterdam, 1970).
- Demtroder, W., *Laser Spectroscopy* (Spring-Verlag, Berlin, 1982).
- Desai, R.C. and Grant, M. in *Fluid Interfacial Phenomena*, edited by C. A. Croxton, (Wiley, New York, 1986).
- Grant, M. and Desai, R.C., *Phys. Rev.*, **A27**, 2577 (1983).
- Gross, E., *Nature*, **126**, 201 (1930).
- Hård, S., Hamnerius, T. and Nilsson, O., *J. Appl. Phys.*, **47**, 2433 (1976).
- Khintchine, A., *Math. Ann.*, **109**, 604 (1934).
- Landau, L.D. and Lifshitz, E.M., *Fluid Mechanics* (Pergamon, Oxford, 1959).
- Lastovka, J.B., *Phys. Rev. Lett.*, **17**, 1039 (1966).
- Levich, V.G., *Physicochemical Hydrodynamics* (Prentice-Hall, Englewood Cliff, New Jersey, 1962).
- Mandel, L. in *Progress in Optics*, edited by E. Wolf, 181 (North-Holland, Amsterdam, 1963).
- Mandel'shtam, L.I., *Zh. Russ. Fiz. Khim. Obshchestva*, **58**, 381 (1926).
- Mazur, E. and Chung, D.S., *Physica*, **A147**, 387 (1987).
- Olson, G.L. and Roth, J.A., *Mat. Sci. Rep.*, **3**, 1 (1988).
- Shih, L.B., *Rev. Sci. Instrum.*, **55**, 716 (1984).
- Wiener, N., *Acta Math.*, **55**, 117 (1930).

## Chapter 3

# Spectral Asymmetry at a Nonequilibrium Interface

Microscopic fluctuations of macroscopic variables play an important role in many physical phenomena both in and out of equilibrium. For more than a century, equilibrium fluctuations in systems ranging from simple molecular fluids to complex biological solutions have been studied both theoretically and experimentally. In the past two decades, there has been much interest in nonequilibrium steady state fluctuations [1984, Fox, 1982]. For nonequilibrium bulk fluids, a number of theoretical predictions were confirmed experimentally using laser light scattering techniques. In particular, asymmetries in the spectra of the scattered light were found to be in agreement with theory [Beysens, 1983, Beysens, Garrabos, *et al.*, 1980, Kiefte, Clouter, *et al.*, 1984, Law, Gammon, *et al.*, 1988]. On the other hand, there have been few theoretical and experimental studies of interfaces out of equilibrium, as the lack of translational symmetry

across the interface renders such studies difficult. Recently, it has been predicted that in the presence of a temperature gradient, the spectrum of light scattered from capillary waves (ripples) on a fluid interface is also asymmetric [Desai and Grant, 1986, Grant and Desai, 1983]. In this chapter, we review the theoretical basis of this prediction, present the results of a surface light scattering experiment designed to observe the predicted asymmetry, and compare these experimental findings with the theoretical expectations.

### 3.1 Background

The thermal fluctuations of the molecules near an interface give rise to propagating capillary waves. Such waves have a very small amplitude, on the order of a few angstroms. As shown in the previous chapter, the presence of capillary waves at an interface is characterized by a Brillouin doublet in the spectrum of the light scattered from the interface. The peaks of the doublet correspond to the downshifting (Stokes) and upshifting (anti-Stokes) of the incident laser beam caused by waves traveling in opposite directions. The frequency at which the doublet occurs is determined by the scattering angle, while the intensity of each peak is proportional to the population of capillary waves traveling in that direction. Here the population of capillary waves resulting in a Stokes shift is denoted as  $n_s$ , and that in an anti-Stokes shift as  $n_a$ , with the corresponding integrated intensities represented by  $I_s$  and  $I_a$ .

In equilibrium, the Stokes and anti-Stokes Brillouin peaks have the same intensity because there are an equal number of capillary waves traveling in each direction. When a temperature gradient exists at the interface, however, the system is no longer in equilibrium. Since the capillary waves are thermally

induced, one expects the populations  $n_S$  and  $n_a$  to no longer be equal, and, consequently, the light scattering spectrum to be asymmetric.

## 3.2 Heuristic Arguments

We begin by using simple arguments [Chung, Lee, *et al.*, 1990, Chung, Lee, *et al.*, 1988] to derive an expression for the asymmetry  $\Delta$  in the Stokes and anti-Stokes populations. We define  $\Delta$  as follows:<sup>1</sup>

$$\Delta = \frac{I_S - I_a}{I_S + I_a} = \frac{n_S - n_a}{n_S + n_a}. \quad (3.1)$$

At high temperatures  $T$ , the population  $n$  of capillary waves with angular frequency  $\omega_c$  is proportional to temperature,

$$n = \frac{k_B T}{\hbar \omega_c}, \quad (3.2)$$

with  $k_B$  and  $\hbar$  the Boltzmann and Planck constants, respectively. The population difference  $n_S - n_a$  can then be approximated by

$$n_S - n_a \approx \frac{k_B}{\hbar \omega_c} 2\Delta T^*, \quad (3.3)$$

where  $\Delta T^*$  is the 'effective' temperature difference for a capillary wave along its mean free path  $l_c$  (see Fig. 4.1). Thus, if we write

$$\Delta T^* = l_c \hat{\mathbf{k}} \cdot \nabla T, \quad (3.4)$$

---

<sup>1</sup>The asymmetry definition of Grant and Desai [Grant and Desai, 1983] is larger by a factor of two.

with  $\hat{\mathbf{k}}$  a unit vector in the direction of propagation of the capillary wave, the asymmetry  $\Delta$  becomes

$$\Delta \approx \frac{n_s - n_a}{2n} \approx \frac{l_c \hat{\mathbf{k}} \cdot \nabla T}{T}, \quad (3.5)$$

Defining the characteristic length scale of the temperature gradient as

$$L_\nabla \equiv [\hat{\mathbf{k}} \cdot \nabla \ln T]^{-1}, \quad (3.6)$$

Eq. (3.5) can be re-expressed. We find

$$\Delta \approx \frac{l_c}{L_\nabla}. \quad (3.7)$$

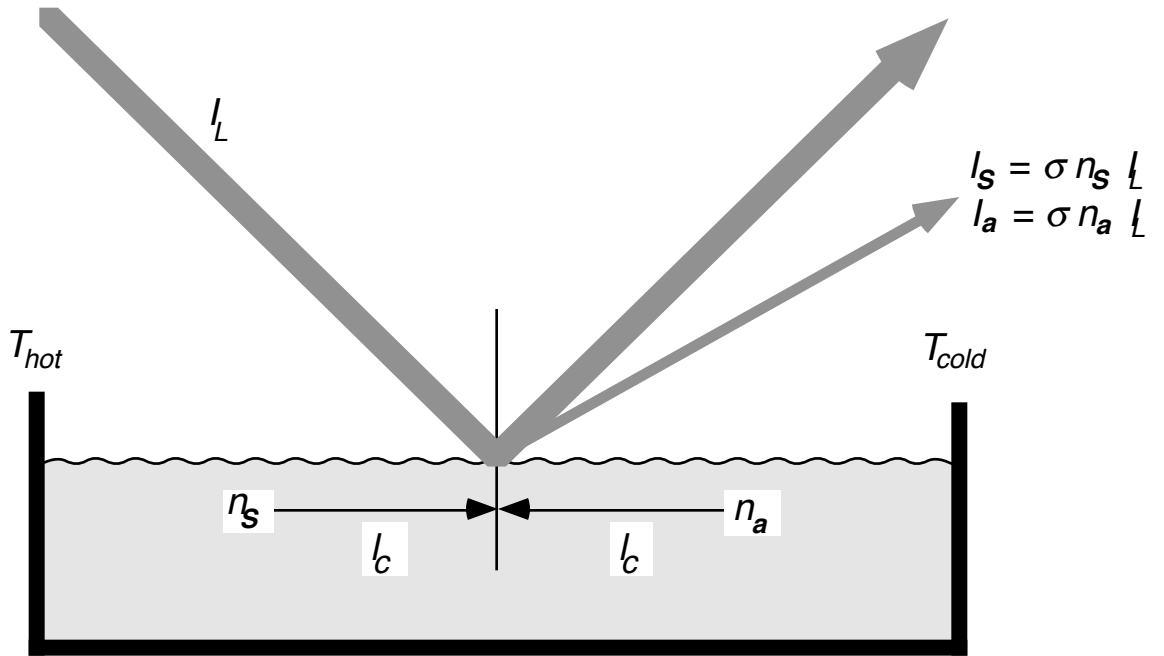


**Fig. 3.1** Scattering of light from an liquid interface out of equilibrium.  $I_L$  is the intensity of the incident light;  $s$  is the scattering cross-section;  $I_S$  and  $I_a$  are the integrated intensities of the scattered light corresponding to the Stokes and anti-Stokes peaks;  $n_s$  and  $n_a$  are the populations of capillary waves resulting in the Stokes and anti-Stokes shifts;  $l_c$  is the mean free path of the capillary waves;  $T_{cold}$  and  $T_{hot}$  are the temperatures at one mean free path away from the probe spot on each side.

Hence, the asymmetry is proportional to the ratio between the mean free path and the characteristic length scale of the temperature gradient.

### 3.3 Fluctuating Hydrodynamic Theory

A more rigorous derivation of the spectral asymmetry at the interface in the presence of a temperature gradient was first presented out by Grant and Desai [Grant and Desai, 1983] using fluctuating hydrodynamics. An equation of motion for the instantaneous position  $\zeta$  of a fluid interface is derived from the linearized hydrodynamic equations [Landau and Lifshitz, 1959]. The spontaneous thermal fluctuations responsible for the time-dependent behavior of  $\zeta$  are taken account of by stochastic driving forces which are added to this equation [Lifshitz and Pitaevskii, 1980]. Next, the nonequilibrium ensemble average of the interfacial fluctuations in  $\zeta$  is obtained from the fluctuation-dissipation theorem. Following the approach of Grant and Desai, we have rederived an expression for the spectral asymmetry  $\Delta$  [Chung, 1991, Chung, Lee, *et al.*, in preparation]. The details of this derivation are not presented in this section, but a comparison between these results and the results from the heuristic arguments of Section 3.2 is made.

From fluctuating hydrodynamics, one finds that for a system of low viscosity, the power spectrum of the interfacial fluctuations yields an asymmetry [Chung, 1991, Grant and Desai, 1983]

$$\Delta = \frac{3}{4} \frac{\sqrt{\sigma\rho}}{\eta} k^{-3/2} \nabla \ln T, \quad (3.8)$$

where  $\sigma$ ,  $\rho$ ,  $\eta$  are respectively the surface tension, density, and shear viscosity of the liquid. It is this result we wish to compare with Eq. (3.7), which was derived using simple arguments.

The dispersion relation for capillary waves of angular frequency  $\omega_c$  is given by [Levich, 1962]

$$\omega_c = \sqrt{\frac{\sigma}{\rho}} k^{3/2} + i\beta, \quad (3.9)$$

where  $k$  is the magnitude of the wavevector  $\mathbf{k}$ , and  $\beta$  is the temporal damping coefficient<sup>2</sup>,

$$\beta = 2\nu k^2, \quad (3.10)$$

in the low-viscosity limit. We define the mean free path of the capillary wave to be the inverse of the spatial damping coefficient<sup>3</sup>. We then have<sup>4</sup>

---

<sup>2</sup>The derivation of the temporal damping coefficient is shown in Section 5.3.

<sup>3</sup>In the low-viscosity limit, the spatial damping coefficient,  $\alpha$ , is related to the temporal damping coefficient by

$$\alpha = \frac{\beta}{v_g} = \beta \left( \frac{\partial \omega_c}{\partial k} \right)^{-1}$$

where  $v_g$  is the group velocity defined as  $\partial \omega_c / \partial k$ . The derivation of this relation is given in Section 5.3.

<sup>4</sup>Grant and Desai [Desai and Grant, 1986, Grant and Desai, 1983] employ a different definition for the mean free path that uses the phase instead of the group velocity:

$$l_c = \frac{1}{\beta} \frac{\omega_c}{k} = \frac{1}{2} \frac{\sqrt{\sigma \rho}}{\eta} k^{-3/2},$$

which results in a factor of 3/2 difference from Eq. (3.11).

$$I_C = \frac{1}{\beta} \frac{\partial \omega_C}{\partial k} = \frac{3}{4} \frac{\sqrt{\sigma\rho}}{\eta} k^{-3/2}. \quad (3.11)$$

Substituting Eqs. (3.6) and (3.11) into (3.8), and using the fact that the temperature gradient is parallel to the unit vector  $\hat{\mathbf{k}}$ , the spectral asymmetry obtained from fluctuating hydrodynamics can then be written as

$$\Delta = \frac{I_C}{L_\nabla}, \quad (3.12)$$

which is identical to the result obtained heuristically in Eq. (3.7).

### 3.4 Experimental Considerations

The larger the asymmetry, the easier its detection. It is thus desirable to choose a system which maximizes the asymmetry, rendering experimental observation feasible. The results of fluctuating hydrodynamics indicates that the spectral symmetry depends on the molecular parameters of the liquid,  $\sqrt{\sigma\rho}/\eta$ , the wavevector,  $k^{-3/2}$ , and the temperature gradient,  $\nabla \ln T$  (see Eq. (3.8)). The success of our experiment then rests on our choice of liquid sample, wavevector, and temperature gradient.

To choose the optimal sample, experiments were carried out using various liquids – mercury, octane and water. Mercury was chosen initially because it is characterized by a large value of  $\sqrt{\sigma\rho}/\eta$ . Unfortunately its high surface tension results in low amplitude capillary waves, and a signal-to-noise ratio insufficient to permit observation of the asymmetry. Measurements on octane, in contrast, yield spectra with an excellent signal-to-noise ratio in equilibrium. In the presence of a temperature gradient, however, the system

becomes unstable. The data presented in this chapter were obtained at a water-air interface. With a water sample, a signal-to-noise ratio is achieved. In addition, the interface remains stable in the presence of a temperature gradient, as the temperature dependence of the molecular parameters  $\sigma$ ,  $\rho$  and  $\eta$  is relatively small.

Equation (3.8) shows that the spectral asymmetry is directly proportional to the temperature gradient; we therefore wish to determine the magnitude of the largest possible gradient so as to maximize the asymmetry. The limits imposed on the gradient are determined by both the freezing and vaporization points of water, as well as by the onset of nonlinear effects, like convection. Measurements on water samples at room temperature, one can allow for a maximal temperature gradient of 20 °C/cm.

The wavevector dependence of the asymmetry,  $k^{-3/2}$ , indicates that experiments are best carried out at small values of  $k$ . We have shown in Chapter 2 that the scattering angle,  $\theta_s$ , of a laser beam incident at an angle  $\theta_j$  upon an interface is related to the wavevector by

$$\theta_s = \frac{k}{k_{laser} \cos \theta_j}, \quad (3.13)$$

where  $k$  and  $k_{laser}$  are respectively the wavevectors of the capillary waves and laser. Choosing a small wavevector then translates into choosing a small scattering angle. With a He-Ne laser beam incident at an angle of about 75° with the normal to the water-air interface, a scattering angle smaller than 10 mrad is necessary for the observation of capillary waves. The resultant wavevectors are in the 60–90 cm<sup>-1</sup> range. Because the scattering angle is so small, it is necessary that stray forward scattering light, the divergence of the laser beam, and the angular motion of the liquid surface be kept to a minimum. The amount of stray

forward scattered light is reduced by placing all optical components at least over 35 cm away from the probe spot on the liquid surface. The divergence of the laser beam is lowered by spatially filtering the beam with pinholes, and collimating it with lenses. Finally, the mechanical stability of the liquid surface is ensured by reducing the depth of the sample with a Delrin spacer, and isolating the setup from external perturbations. The entire experimental setup is placed on an actively stabilized platform, which, in turn, is located on top of a pneumatically vibration-isolated optical table. The resulting stability of the surface is about  $70 \mu\text{rad}$ , and the angle of view determined by the opening of a pinhole is about  $100 \mu\text{rad}$ .

The wavevector range determined above corresponds to capillary wave frequencies between 0.6 and 1.2 kHz. A high resolution technique is therefore necessary to spectrally resolve the power spectrum of the interface fluctuations.

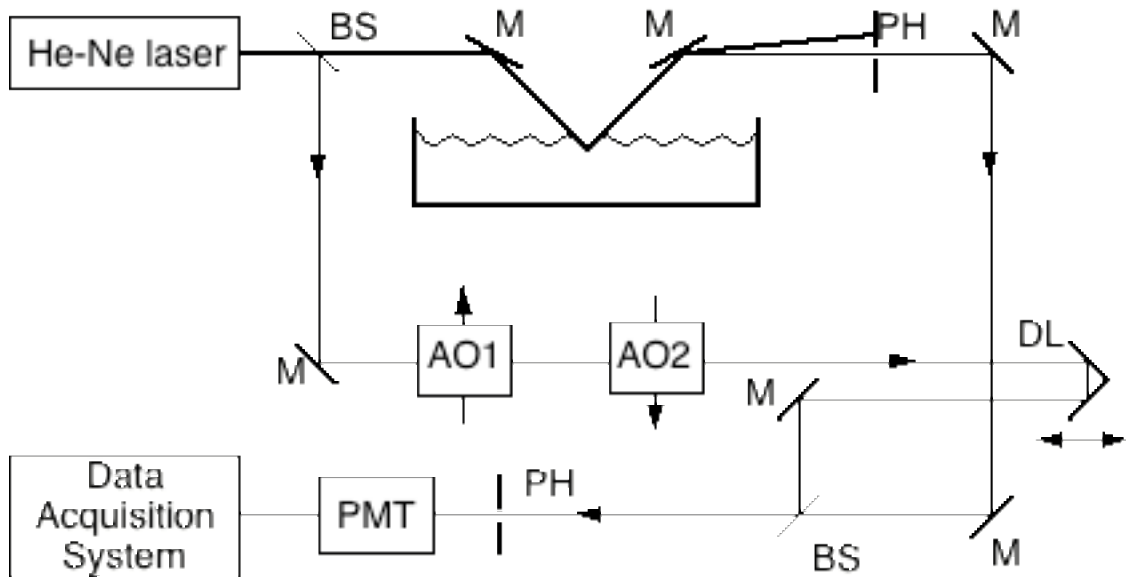


**Fig. 3.2** Schematic diagram of the experimental setup. The surface of the liquid is probed with a multimode He-Ne laser beam. A local oscillator is derived from the same laser, and frequency-shifted by two acousto-optic modulators (AO1 and AO2). The scattered beam is combined with the local oscillator beam by a beamsplitter (BS), and the resulting beat signal is recorded by a photomultiplier tube (PMT). The delay line (DL) is for the adjustment of the pathlength of the local oscillator beam to match with that of the scattered beam. M – mirror; PH – pinhole.

In addition, the measurement of the asymmetry requires a technique which can spectrally separate capillary waves traveling in opposite directions. The Fourier transform heterodyne spectroscopic technique described in Chapter 2, which has a resolving power of over  $10^{13}$ , and is sensitive to the direction of capillary wave propagation, makes it a suitable candidate for this experiment.

A schematic diagram of the surface light scattering apparatus is shown in Fig. 4.2. A collimated, 4 mW multimode He-Ne laser beam<sup>5</sup> is split into two with a beam splitter: 5% of the beam serves as a local oscillator, while the remainder illuminates the liquid surface. The main beam, which is polarized perpendicular to the plane of incidence, makes an angle of about  $75^\circ$  with the normal to the surface. The beam width near the surface is 2 mm, yielding a surface spot of about 10 mm. A polarizer in front of the photomultiplier tube eliminates stray light. To separate the two Brillouin peaks in this frequency range, the local oscillator is frequency-shifted by 4.5 kHz. This is accomplished using two 40 MHz acousto-optic modulators<sup>6</sup> with a difference in carrier frequency of 4.5 kHz. To align the setup, strong surface waves of the desired frequency are induced with a transducer<sup>7</sup>. For high enough amplitudes, the Bragg scattered beam is visible and can be aligned with the local oscillator beam. Since the alignment is very sensitive to the motion of the interface, the system must be adequately isolated from external vibrations; the necessary isolation is provided by the actively stabilized platform and the pneumatically vibration-isolated optical table.

---

<sup>5</sup>CR 80-5HMM, Coherent.

<sup>6</sup>AOM-40, IntraAction Corporation.

<sup>7</sup>The transducer is a flat wire attached to the membrane of a tweeter. Audio signals of the desired frequency applied to the tweeter are converted to mechanical vibrations of the wire. The wire is placed across the surface of the liquid, parallel to the plane of incidence of the laser beam. This arrangement results in the generation of plane waves at the surface.

The water sample is contained in a shallow black Delrin container ( $75 \times 75 \times 4 \text{ mm}^3$ ), located inside a sealed compartment ( $0.66 \times 0.23 \times 0.23 \text{ m}^3$ ) made of black anodized aluminum. Care is taken to prevent dust and impurities from contaminating the interface. Distilled and deionized water is obtained from a Milli-Q system and prepared in a class 1000 clean room. Before each set of measurements, the container is cleaned and pre-soaked. The compartment is evacuated and flushed several times with 'dry high purity' grade nitrogen gas filtered<sup>8</sup> to remove dust particles. After cleaning and flushing, the compartment is filled with nitrogen gas at atmospheric pressure. The water sample, contained in a thoroughly cleaned glass dispenser<sup>9</sup>, is introduced into the container from outside the compartment by a feedthrough.

A temperature gradient is created along the surface using a pair of epoxy-coated copper plates, temperature-controlled by two thermoelectric heat pumps<sup>10</sup>. A schematic diagram is shown in Fig. 4.3. The plates, which are separated by 16 mm, are immersed about 0.1 mm below the surface to avoid surface distortion. To damp out long-wavelength gravity waves, reduce convection, and increase mechanical stability, the depth of the water sample is kept at around 1 mm. A liquid-cooled<sup>11</sup> heat sink drains excess heat from the heat pumps and prevents condensation of water vapor on the optics. The temperature of the plates is monitored by a pair of thermistors<sup>12</sup>, which are accurate to within  $\pm 0.1 \text{ K}$ . To determine the temperature gradient at the

---

<sup>8</sup>0.22- $\mu\text{m}$  pore size, Millipore Corporation.

<sup>9</sup>2-liter Chempette® compact dispenser, L-07916-50, Cole-Parmer.

<sup>10</sup>CP 1.4-127-0.6L, Melcore.

<sup>11</sup>2-liter temperature bath, Lauda K-2/R, Brinkman Instruments.

<sup>12</sup>44032, Omega.

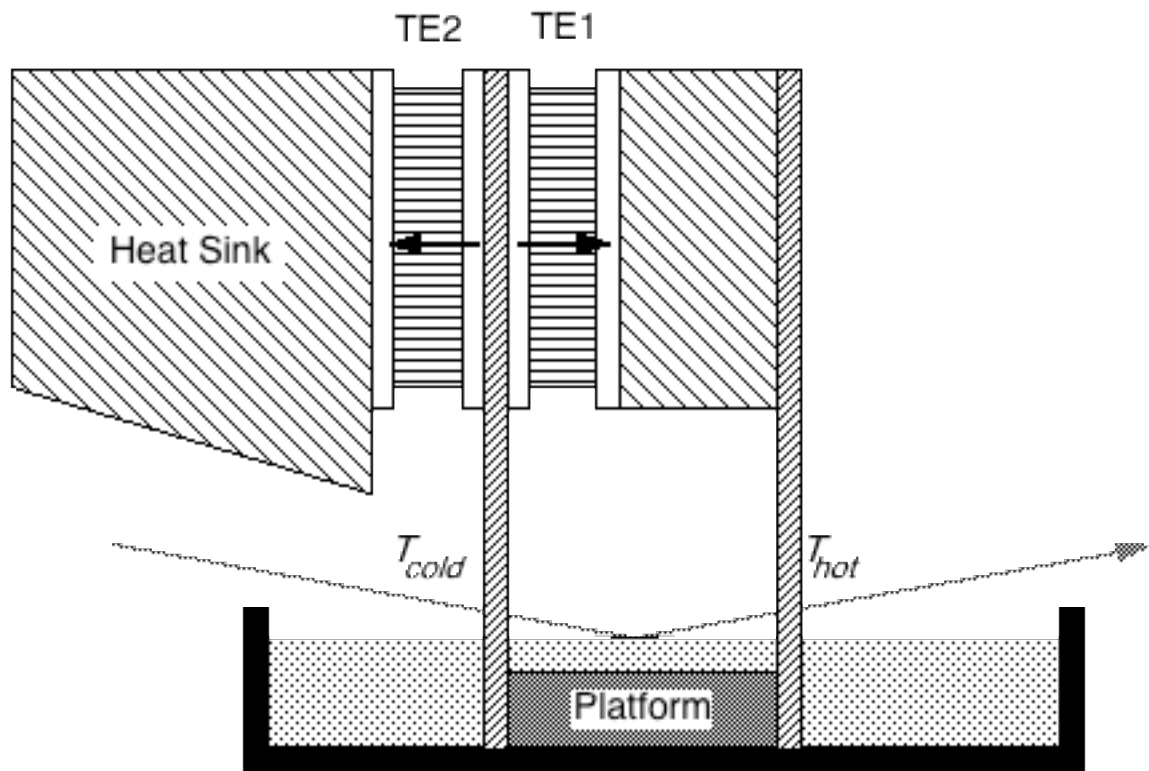


**Fig. 3.3** Temperature gradient assembly. A temperature gradient is applied along the surface by a pair of copper plates kept at temperatures  $T_{cold}$  and  $T_{hot}$ . The spacing between the two plates is 16 mm. The temperatures of the plates are controlled by two thermoelectric heat pumps (TE1 and TE2), with a water-cooled heat sink removing the excess heat from the pumps. A platform is used to reduce the depth of the water sample.

illuminated surface spot, the temperature profile along the surface is measured with a second pair of thermistors mounted on a translation stage. The profile is found to be nonlinear. When the probe spot is located midway between the two plates, the gradient at this center point, obtained from the measured temperature profile is half as large as would be expected assuming a linear profile.

The beat signal between the scattered light and the local oscillator is recorded with a photomultiplier tube. The signal is sampled for 15 s at a 20-kHz rate using an analog-to-digital computer interface<sup>13</sup>, and the full signal trace is

<sup>13</sup>MacADIOS II, GW Instruments.

stored in the memory of a microcomputer<sup>14</sup>. Next, the frequency spectrum of the digitized signal is obtained using a fast Hartley transform of the sampled data points [Bracewell, 1965]. This procedure is repeated eight times to improve the signal-to-noise ratio. An example of the resulting averaged spectrum, corresponding to the spectrum of the interfacial fluctuations, is shown in Fig. 4.4.

Asymmetry values are determined by fitting a theoretical spectral shape to the experimental data points. The spectral shape,  $S(\omega)$ , is obtained from linear response theory [Langevin, Meunier, *et al.*, 1984]. For a system of low viscosity,  $S(\omega)$  is well approximated by squared Lorentzians [Chung, 1991]

$$S(\omega) = \frac{16k_B T \eta k^3 / \rho^2}{\left[ (\omega - \omega_{AO})^2 - \omega_C^2 \right]^2 + 4\beta^2 (\omega - \omega_{AO})^2}, \quad (3.14)$$

where  $\omega_{AO}$  is the angular frequency of the acousto-optic modulator. In the narrow linewidth approximation [Loudon, 1984], the power spectrum reduces to Lorentzians,

$$S(\omega) = \frac{4k_B T \eta k^3 / \rho^2}{\left[ (\omega - \omega_{AO}) - \omega_C \right]^2 + 4\beta^2 (\omega - \omega_{AO})}. \quad (3.15)$$

---

<sup>14</sup>Macintosh II, Apple Computers

Because of the divergence of the laser beam, the finite size of the pinholes, and the residual motion of the surface, experimental spectra are always convoluted with some instrumental function. The data points are then most accurately fitted to a convolution of the spectral shape obtained from linear response theory and an instrumental function measured for a system of low viscosity [Langevin, 1974]. In general, the instrumental function is approximately Gaussian [Earnshaw, McGivern, *et al.*, 1988], and the measured spectrum can thus be approximated by the convolution of a Lorentzian and a Gaussian (Voigt profile)

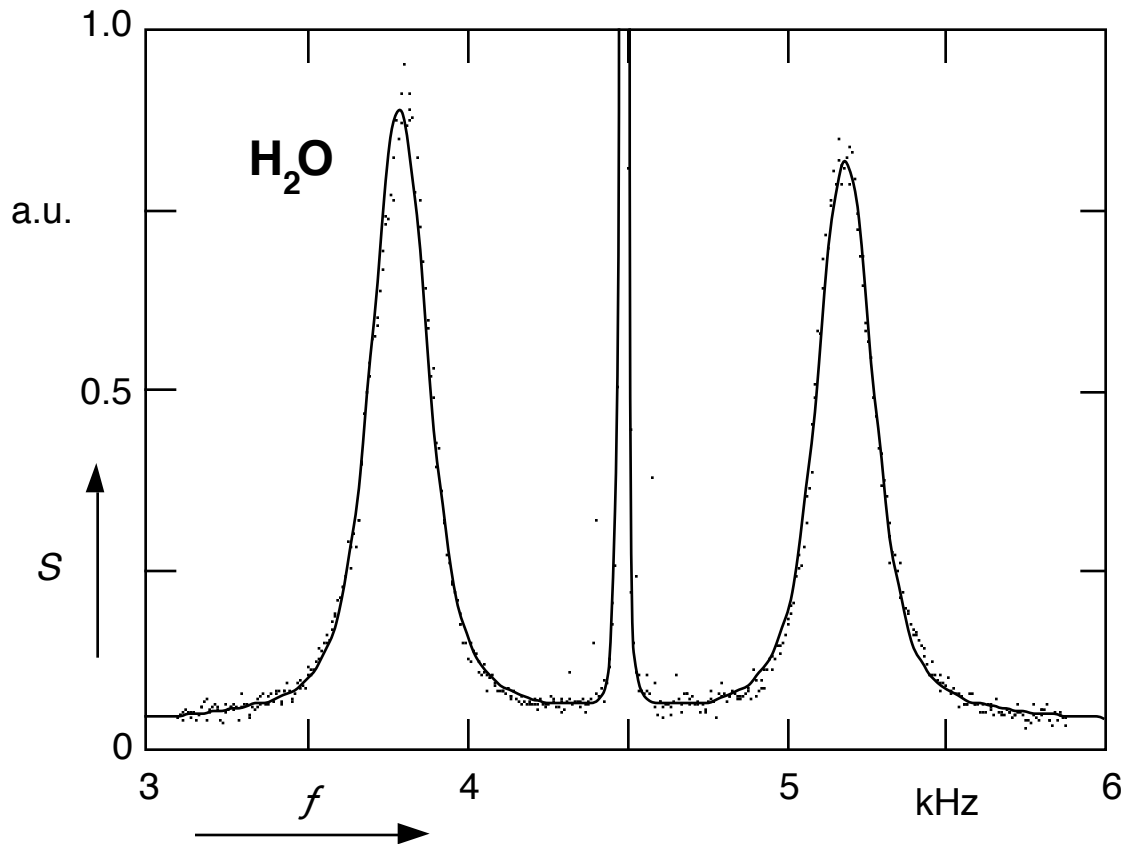


**Fig. 3.4** Power spectrum obtained for  $k = 90 \text{ cm}^{-1}$  and  $\nabla T = 9.5 \text{ K/cm}$  at  $T = 295 \text{ K}$ . A capillary wave peak is found on each side of an intense central peak at  $\omega = \omega_{LO}$ , which is due to stray elastic scattering of the incident laser light. The dots are experimental data points, while the solid line is a least-squares fitted set of two Voigt profiles for the two side peaks and a Lorentzian for the central peak. The experimental observed asymmetry is 0.008, while the theoretically predicted one is 0.023.

[Armstrong, 1967]. The asymmetries reported here were obtained from nonlinear least-squares fitting with the Voigt profiles producing the best fit<sup>15</sup>.

### 3.5 Results and Discussion

In Fig. 4.5, the experimentally determined asymmetry,  $\Delta_{exp}$ , is compared with the theoretically predicted one,  $\Delta_{theory}$  (see Eq. (3.8)). Here, literature values for the density, surface tension and viscosity at the temperature of the probed region [CRC, 1984] are used. Since the frequency response of the apparatus is not completely flat, spectra taken in the absence of a temperature gradient show a small instrumental asymmetry,  $\Delta_{inst}$ . All data are corrected for this small asymmetry. The error bar for the point at  $\Delta_{theory} = 0$  represents the standard deviation in  $\Delta_{inst}$  when  $\nabla T = 0$ . The sign of the asymmetry can be reversed by reversing  $\hat{\mathbf{q}}$ . As can be seen from Fig. 4,5, this indeed results in a sign change of the measured asymmetry. The slope of the experimental data points, represented by the solid line in Fig. 4.5, is about three times smaller than expected on the basis of Eq. (3.8). A number of possible causes contributing to this discrepancy are: 1) finite size effects, 2) nonlinear effects, 3) contamination of the surface, and 4) the fitting procedure. Each of these possible problems is discussed below.

In light scattering experiments on nonequilibrium bulk liquids [Beysens, Garrabos, *et al.*, 1980], a similar discrepancy between measured and predicted asymmetries was found. In this case, the discrepancy was attributed to finite size

---

<sup>15</sup>We have also fitted our experimental data the square Lorentzian and Lorentzian profiles given by Eqs. (3.14) and (3.15), but the  $\chi^2$  values obtained from Voigt profile fits are consistently about two times better than those from other fits.

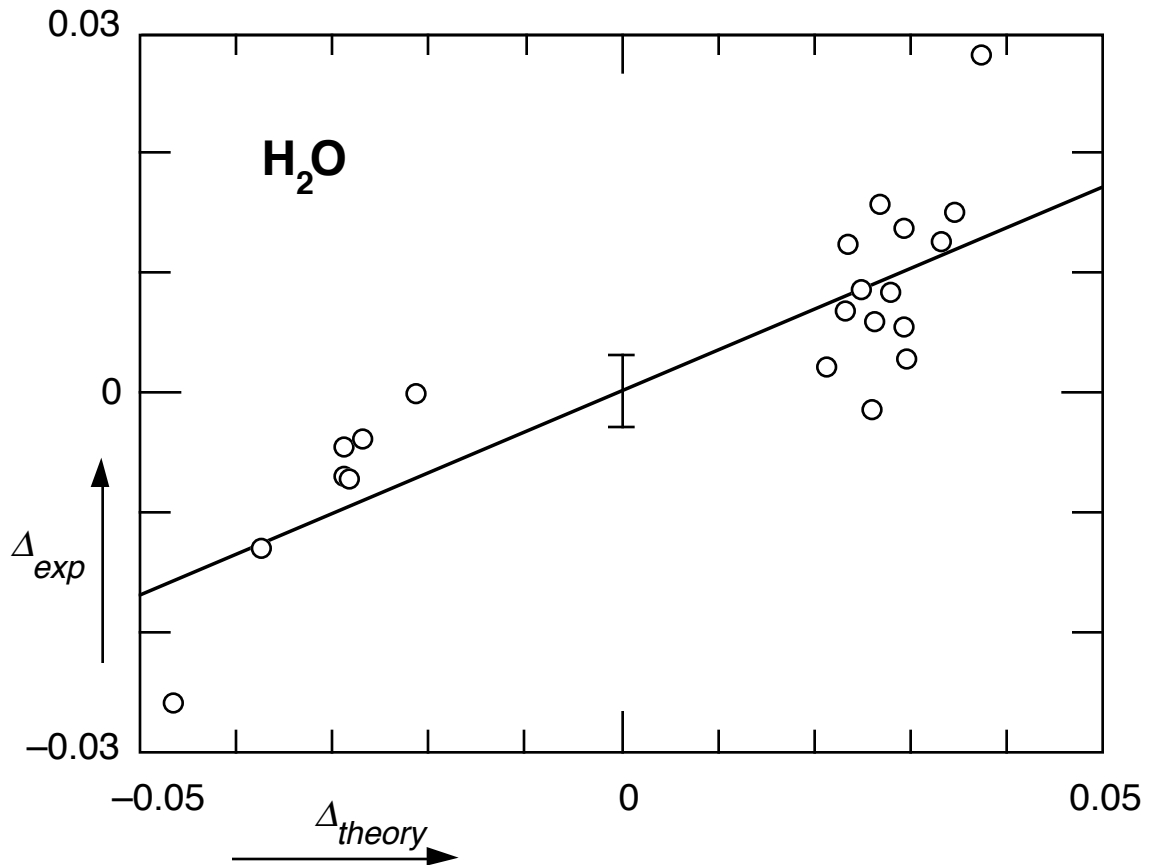


**Fig. 3.5** Measured capillary wave asymmetry vs. theoretical predicted values. The expected slope is 1; the experimental slope (solid line) is  $0.34 \pm 0.04$ .

[Satten and Ronis, 1982] and nonlinear effects [Kirkpatrick, Cohen, *et al.*, 1982]. In a later experiment by Kiefte *et al.* [Kiefte, Clouter, *et al.*, 1984], close agreement with theory was obtained for a particular ‘best’ data set. It was shown that finite size and, to a lesser extent, nonlinear effects indeed affect the measurements. Thus far, theoretical analyses of these effects have only been carried out for bulk liquids.

In the case of a nonequilibrium interface, one expects finite size effects to be important a role when either  $l_c/L$  or the acoustic reflectivity of the container walls is large [Satten and Ronis, 1982]. Here  $l_c$  is the mean free path (see Eq. (3.11)) and  $L$  is the distance between the two plates. For our setup, using

literature values of  $\sigma$  and  $\eta$ , the ratio falls in the range  $0.45 \leq l_c/L \leq 0.9$ . Additional tests show that the spectrum of an induced capillary wave traveling in one direction has only a single side peak, indicating that acoustic reflectivity is negligible.

The nonlinear effects that associate with the temperature gradient depend on  $l_c / L_\nabla$ , the ratio of the mean free path to the characteristic length scale of the gradient (see Eq. (3.6)). In addition, the ratio  $\Delta T/T$  must be small enough so that the temperature dependence of the molecular parameters may be neglected and a steady state maintained. In the present setup,  $\Delta T/T \approx 0.1$ . This value is comparable to the value for the best data set from the experiment by Kieft *et al.* on bulk water. Recall that the asymmetry obtained from that data agree with the theoretical predictions. We also attempted to investigate the dependence of the asymmetry on the temperature difference and spacing between the plates. Unfortunately, the possible variations in the relevant parameters were insufficient to allow for any conclusive statements.

Contamination of the liquid surface can contribute significantly to the observed discrepancy. Surface contaminants tend to lower the surface tension, thus reducing the asymmetry, as in Eq. (3.8). Based on results from a related experiment (see Section 5.4), we believe that contamination of the water surface by impurities in the buffer gas may be largely responsible for the difference between the expected and observed values. In that experiment, the spatial damping coefficient of capillary waves at a water-air interface was measured. Results obtained using 'dry high purity' nitrogen yields a damping coefficient two to four times greater than predicted by hydrodynamic theory, while results obtained with an ultra high purity nitrogen buffer gas (<0.5 ppm total hydrocarbon content) are in excellent agreement with theory. We believe that

the trace hydrocarbons in the 'dry high purity' nitrogen are deposited at the water-air interface, lowering the surface tension and producing an unexpectedly small observed asymmetry.

Finally, despite the excellent separation of the Brillouin peaks from the central peak, the experimentally determined asymmetry has a weak dependence on the background intensity at the position of the Brillouin peaks, as well as on the lineshape used in the fitting procedure. While resulting in a poorer overall fit, fitting with simple or squared Lorentzians, for example, consistently yields asymmetries about 30% larger than obtained using the Voigt profile. Such an effect is, however, too small to explain the observed factor of three discrepancy.

In conclusion, Fourier transform heterodyne spectroscopy, with its directional sensitivity and high resolution, allows one to observe the broken translational symmetry of a nonequilibrium liquid surface. We have measured the asymmetry in the two Brillouin peaks of light scattered from a liquid-vapor interface subject to a temperature gradient. Our result agrees, in sign and order of magnitude, with the asymmetry predicted by linearized fluctuating hydrodynamics.

## References

- Armstrong, B.H., *J. Quant. Spectros. Rad. Transfer*, **7**, 61 (1967).
- Beysens, D., *Physica*, **118A**, 250 (1983).
- Beysens, D., Garrabos, Y. and Zalczer, G., *Phys. Rev. Lett.*, **45**, 403 (1980).
- Bracewell, R.N., *The Fourier Transform and Its Applications* (McGraw-Hill, New York, 1965).
- Chung, D.S., Ph.D. thesis: *Fourier Transform Heterodyne Spectroscopy of Liquid Interfaces* (Harvard University, 1991).
- Chung, D.S., Lee, K.Y. and Mazur, E., *Phys. Lett.*, **A145**, 348 (1990).
- Chung, D.S., Lee, K.Y. and Mazur, E., (in preparation).
- Chung, D.S., Lee, K.Y.C. and Mazur, E., *Int. J. Thermophysics*, **9**, 729 (1988).
- CRC Handbook of chemistry and physics*, edited by Weast, R. (CRC Press, Boca Raton, 1984)
- Desai, R.C. and Grant, M. in *Fluid Interfacial Phenomena*, edited by C. A. Croxton, (Wiley, New York, 1986).
- Earnshaw, J.C., McGivern, R.C. and Winch, P.J., *J. Phys. (France)*, **49**, 1271 (1988).
- Fox, R.F., *J. Phys. Chem*, **86**, 2812 (1982).
- Grant, M. and Desai, R.C., *Phys. Rev.*, **A27**, 2577 (1983).
- Kiefte, H., Clouter, M.J. and Penny, R., *Phys. Rev.*, **B30**, 4017 (1984).
- Kirkpatrick, T., Cohen, E.G.D. and Dorfman, J.R., *Phys. Rev. A*, **26**, 972 (1982).
- Landau, L.D. and Lifshitz, E.M., *Fluid Mechanics* (Pergamon, Oxford, 1959).
- Langevin, D., *J. Chem. Soc. Faraday Trans. I*, **70**, 95 (1974).

Langevin, D., Meunier, J. and Chatenay, D. in *Surfactants in solutions*, edited by K. L. Mittal and B. Lindman, (Plenum, New York, 1984).

Law, B.M., Gammon, R.W. and Sengers, J.V., *Phys. Rev. Lett.*, **60**, 1554 (1988).

Levich, V.G., *Physicochemical hydrodynamics* (Prentics-Hall, Englewood Cliffs, 1962).

Lifshitz, E.M. and Pitaecskii, L.P., *Statistical Physics Part 2* (Pergamon, Oxford, 1980).

Loudon, R. in *Surface Excitations*, edited by Agranovich, V. M. and Loudon, R. (North-Holland, Amsterdam, 1984).

*Physics Today*, **37** (1984), entire volume.

Satten, G. and Ronis, D., *Phys. Rev. A*, **26**, 940 (1982).

## Chapter 4

# Experimental Apparatus and Procedures for Capillary Wave Damping Measurements

At a pure liquid-vapor interface, the energy of capillary waves is dissipated by the viscosity of the liquid, and, as a result, the surface waves are damped. When the interface is covered by a surfactant<sup>1</sup> film, the surface properties of the system are altered. This gives rise to changes in capillary wave damping, which, in turn, depend on the concentration of the surface-active molecules. The first step towards studying capillary wave damping therefore calls for an apparatus which allows one to effectively control and measure the relevant parameters (surface concentration, temperature, two-dimensional surface pressure, etc.) of the liquid system. Such an apparatus for handling the liquid sample is described in detail in

---

<sup>1</sup>Surfactant is short for 'surface-active substance'; these are substances which, when spread on a liquid surface, change the properties of the liquid surface.

the first half of this chapter. With a reliable apparatus at hand, one can proceed to carry out damping measurements. We have developed a non-intrusive, differential optical technique to measure spatial damping of capillary waves. The details of this technique are presented in the second half of this chapter.

## 4.1 Apparatus

The attenuation of capillary waves can be greatly increased by the presence of any surface-active material at the interface. To investigate the effect of a given surfactant monolayer on capillary wave damping, it is necessary to minimize other surface impurities at the interface, and to ascertain that the system under study is clean.

To achieve this, all damping measurements are done using a home-made Langmuir trough. The trough, which has a barrier laid across its top, holds the liquid sample, often referred to as the liquid subphase, under study. The barrier is mounted onto a translation stage, and the surface area occupied by the surfactant film can be altered by changing the barrier position. A Teflon-coated stainless steel trough is chosen a solid Teflon trough because better temperature control can be attained in the former. One drawback of this is, however, that a good seal between the barrier and the trough is difficult to maintain at high temperatures due to the big difference in the coefficients of thermal expansion between stainless steel and Teflon.

The entire setup is sealed inside an aluminum chamber filled with ultrahigh purity nitrogen<sup>2</sup>. The chamber is designed in such a fashion that

---

<sup>2</sup>99.999% purity with < 0.5 ppm total hydrocarbon content, Igo.

addition and removal of the liquid subphase, aspiration of the subphase surface, spreading of surfactant monolayer, control of surfactant concentration, measurement of surface pressure, generation of induced capillary waves, and translation of the wave source can all be done with the chamber sealed. The chamber is temperature-controlled, and fitted with optical quality windows for the incident and scattered laser beams. The following sections describe the various aspects of this apparatus.

### 4.1.1 Langmuir Trough

The trough is milled from a solid piece of stainless steel 34.29 cm  $\times$  8.89 cm  $\times$  1.75 cm. A recess 30.48 cm  $\times$  7.62 cm  $\times$  0.48 cm, with 0.64-cm thick walls all around, is used for holding the liquid subphase. This stainless steel piece is also equipped with water passages for temperature control. A cross-section of this is shown in Fig. 4.1. The top edges of the wall are flat, but the top parts of the inner side edges along the length of the trough are cut at a 45° angle so as to make good contact with the barrier sliding over them. Four clearance holes are found at each end of the trough: two are for aligning the trough to the translation stage described in Section 4.1.2, and the other two are for the actual attachment.

Next, the trough is sent out to be coated with Teflon<sup>3</sup>. The surface of the trough is first roughened by a grit-blasting treatment carried out at over 370 °C. A layer of acid primer, provide the necessary etching, is then applied to the rough surface. An intermediate layer of black Teflon is sprayed on before the

---

<sup>3</sup>Teflon PFA coating, Precision Coating Incorporated.

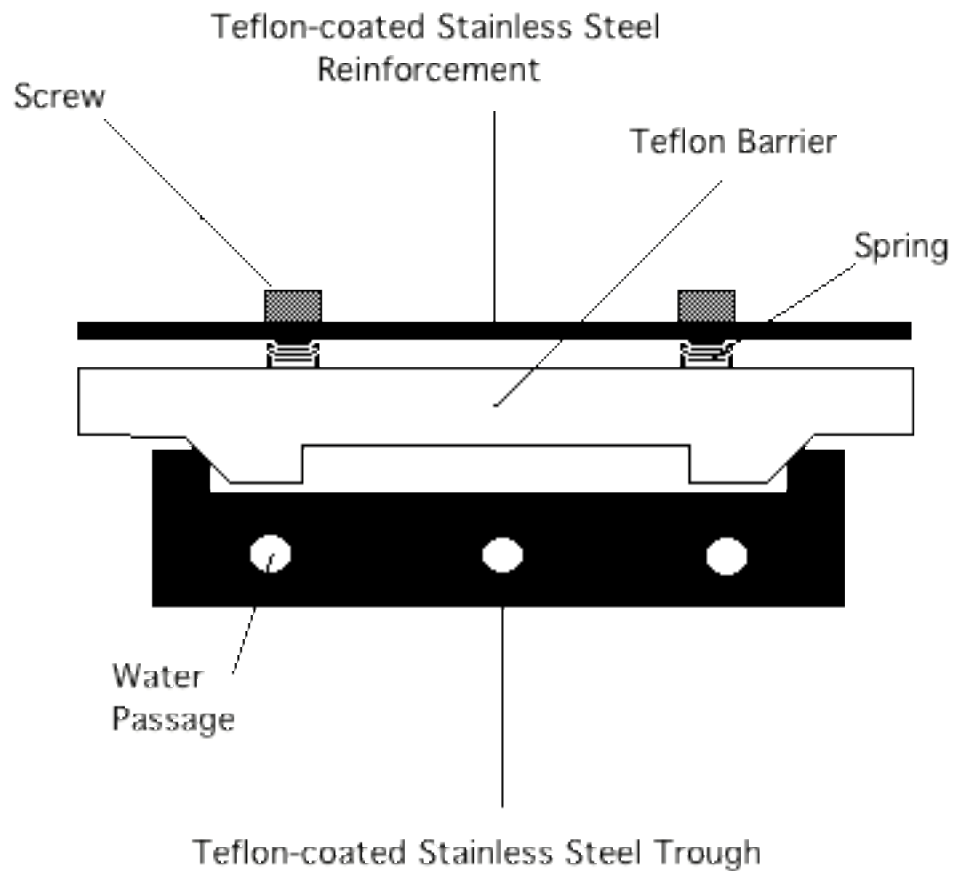


**Fig. 4.1** A cross-sectional diagram of the Langmuir trough, showing the Teflon-coated stainless steel trough with water passages for temperature control, and a solid Teflon barrier with its Teflon-coated stainless steel reinforcement.

final layer of PFA Teflon is applied. The resulting Teflon coating is between 0.25 to 0.52  $\mu\text{m}$  in thickness.

A barrier made of solid Teflon is placed across the trough to control the surface area of the surface film, see Fig. 4.1. The two ends of the barrier are cut at a 45° angle to match the side edges of the trough. The barrier has a cut-out at the bottom to ease the flow of the liquid subphase upon compression and expansion. To prevent the barrier from bending upwards, a 0.32-cm thick black Teflon-coated stainless steel reinforcement is screwed onto the barrier. The whole unit is then attached to the translation stage described in Section 4.1.2. Springs are placed between the stainless steel reinforcement and the Teflon

barrier to provide a constant vertical force pushing the barrier against the trough. This configuration helps ensure a good contact between the barrier and the trough.

## 4.1.2 Surface Area Control

The surface concentration of surfactant molecules can be adjusted in two ways: either one fixes the surface area and changes the quantity of surfactant molecules spread, or one spreads a fixed number of surfactant molecules (by adding a known amount of surfactant solution) and changes the surface area that they can occupy (by sliding the barrier along the trough). In the present setup, the sliding of the barrier is done by attaching it to a translation stage.

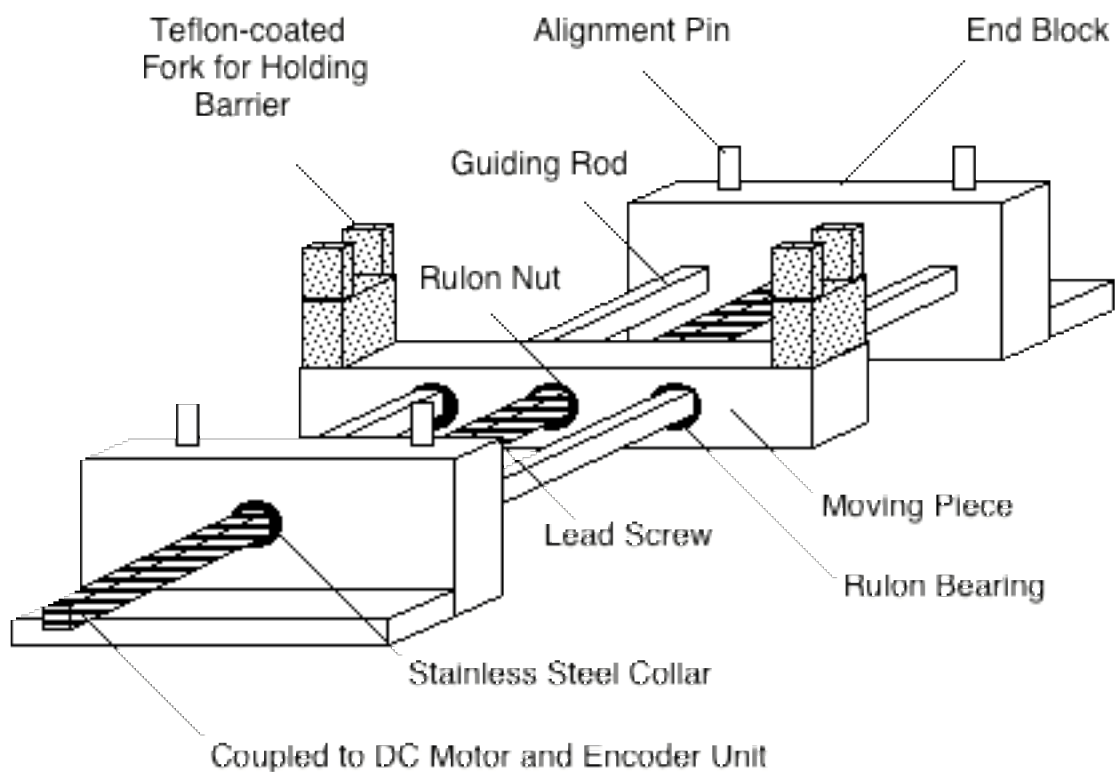


Fig. 4.2 Translation stage for controlling the surface area of the Langmuir trough.

A schematic diagram of the translation stage is shown in Figure 4.2. To minimize corrosion, the entire translation stage is made of stainless steel. It has two end pieces which are held in position by screwing them onto the chamber. On these pieces are guiding pins and screw holes for aligning and mounting the trough. Two 0.95-cm stainless steel rods connect the two end pieces and act as guiding rods for the moving piece. The moving piece is wider than the trough, and part of it extends beyond each side of the trough. Two forks are attached to these protruding ends, and the barrier unit is clamped onto these forks. Each guiding rod is connected to the moving piece via two bearings. Nylon bearings were originally used in the apparatus. The moisture-absorbing nature of nylon, however, results in the expansion of the bearings when the setup is left in a humid environment. This expansion makes the fit very tight and translation difficult. In the current setup, nylon bearings are replaced by Rulon<sup>4</sup> ones. The smooth texture and self-lubricating property of Rulon makes for bearings which allow the moving piece to slide easily in the absence of lubrication. The moving piece is driven at its center by a 24-pitch lead screw 0.95 cm in diameter, which goes through the two Rulon nuts, each attached to one end of the moving piece. By adjusting the relative position of the two Rulon nuts that are attached to the moving piece, a desired tightness of fit as well as a reduction in the backlash of the stage can be attained. Stainless steel collars are used on the outer side of the end pieces to prevent the lead screw from having any lateral motion. This, along with the long bearing for the guiding rods and the nut configuration for the lead screw, further reduce backlash of the stage.

---

<sup>4</sup>Rulon is a specially-compounded form of PTFE fluoropolymer and other inert ingredients. The combination results in a product of higher rigidity than Teflon.

The lead screw is connected to a DC motor via a flexible stainless steel coupler. The DC motor<sup>5</sup> has a built-in magnetic encoder<sup>6</sup> to determine the location of the barrier; the barrier position is read out using LED display controller<sup>7</sup>.

### 4.1.3 Surface Balance

The Wilhelmy plate [Gains, 1977] method is used to measure the surface tension of the system. Figure 4.3 shows schematically the surface balance apparatus. A 1.3 cm × 1.3 cm filter paper<sup>8</sup> is used as the Wilhelmy plate, and is held in place by a holder made of Kel-F<sup>9</sup>. The filter paper holder is connected to a tapped Kel-F rod, and the unit is suspended from a Teflon-coated leaf spring, which is connected to a stainless steel mount. When the filter paper is immersed in the liquid, it experiences a force exerted by the surface tension pulling it down. The force,  $F$ , when neglecting buoyancy effects, is given by

$$F = \sigma L \cos \theta, \quad (4.1)$$

where  $\sigma$  is the surface tension,  $L$  the perimeter of the plate, and  $\theta$  the contact angle between the plate and water. In the case of complete wetting, the contact angle becomes zero; the force exerted on the plate is then the product of the surface tension and the perimeter of the plate. Since the force is linearly

---

<sup>5</sup>CTC-323-21 with 97.3:1 gearhead ratio, and a maximum torque of 57 oz.-in., Micro Kinetics.

<sup>6</sup>CTC-322-MI, Micro Kinetics.

<sup>7</sup>Encoder Mike controller 18011, Oriel.

<sup>8</sup>Durapore type, Millipore.

<sup>9</sup>Kel-F is also a fluoropolymer with high rigidity.

proportional to the vertical displacement of the plate, one can measure the force by monitoring this displacement.

The displacement is measured using a hermetically sealed linear variation differential transformer<sup>10</sup> (LVDT) designed for use under humid conditions. The LVDT is a cylindrical electromechanical device that produces an electrical output proportional to the displacement of a separate movable rod-shaped magnetic core. It consists of a primary coil and two secondary coils (one above and one

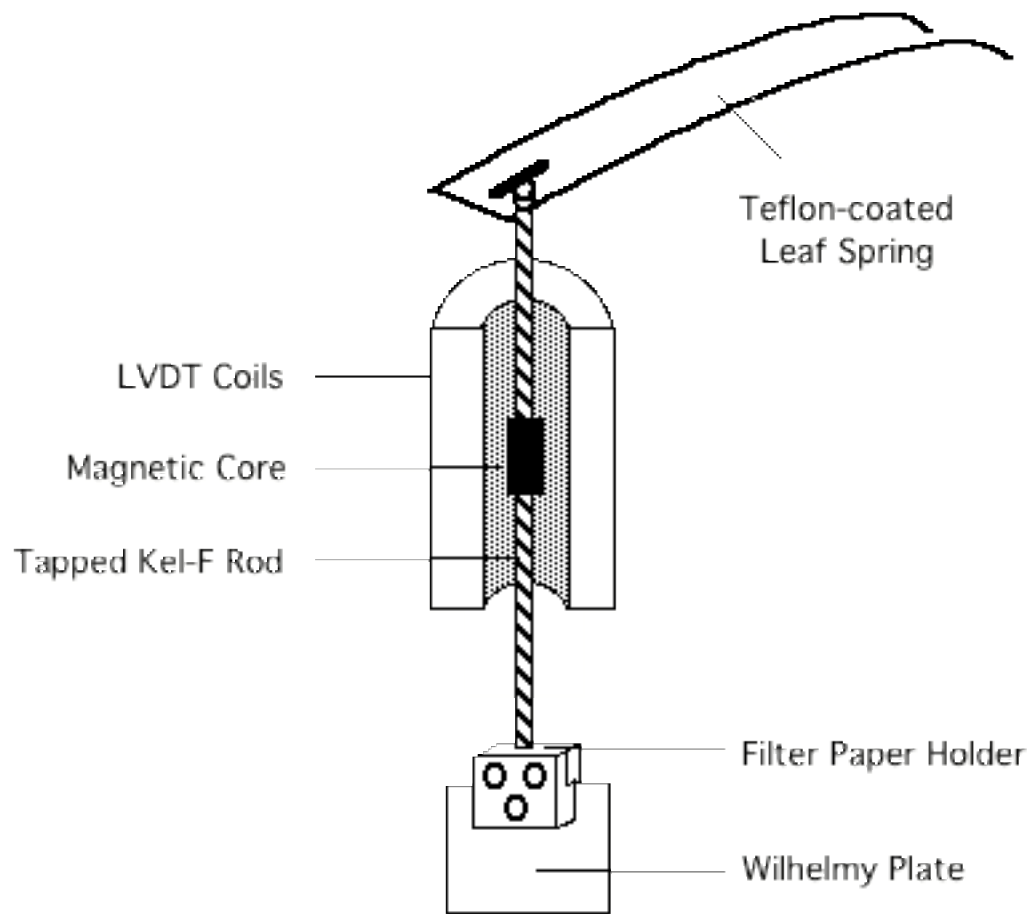


**Fig. 4.3** A surface balance unit where the Wilhelmy plate, made of filter paper, is held and suspended freely by a leaf spring. The vertical displacement of the Wilhelmy plate, and hence the surface pressure, is determined by the use of a linear variation differential transformer.

---

<sup>10</sup>HPA-50, Schaevits.

below) which are connected so that their voltages have opposite signs. The magnetic core provides the magnetic flux linking the two coils, and the LVDT measures the voltage difference between the upper and lower coils. When the magnetic core is placed at the null position, the voltages of the upper and lower coils have the same magnitude but opposite polarity, thus canceling one another. When the core is displaced downward, the voltage of the lower coil increases while that of the upper coil decreases; this results in a net negative voltage. The reverse holds when the core is displaced upward from its null position. The differential voltage output changes linearly with the core position over a nominal range. In the particular model used in this setup, the range is  $\pm 0.13$  cm.

The LVDT coil unit is held by the stainless steel mount, while the magnetic core, screwed onto the tapped rod of the filter paper holder, is suspended freely close to its null position by a leaf spring. It is very important that the magnetic core hangs freely, otherwise, the resulting voltage output will not be a good indicator of the actual displacement. The relationship between the LVDT output voltage and the force experienced by the filter paper can be obtained by adding known weights to the surface balance. With a calibrated output voltage and a known filter paper perimeter, the surface tension of the liquid can then be obtained using Eq. (4.1). The output voltage from the LVDT is connected to an analog-to-digital board<sup>11</sup> and the calibrated value is read out<sup>12</sup> by the computer after averaging 1000 data points over 0.5 s. The entire stainless steel unit is mounted onto a translation stage driven vertically by a DC motor and encoder unit<sup>13</sup>.

---

<sup>11</sup>MacADIOS, GW Instruments.

<sup>12</sup>Superscope, GW Instruments.

<sup>13</sup>Encoder Mike, Oriel.

The sensitivity of this surface balance is about 0.05 dynes/cm. To obtain the absolute value of the surface tension, the filter paper is lifted at a slow rate until it is out of the liquid. The surface tension is then the difference in the LVDT readings right before and after the plate is lifted out of the liquid surface. The surface tension of a pure water-air interface obtained in this manner agrees well with published values [Weast, 1985]. The relative changes in surface tension can also be obtained by leaving the plate at a fixed arbitrary height and monitoring the changes in the LVDT readings as, for instance, the surface area is altered.

#### **4.1.4 Water and Subphase Handling**

Ultrapure<sup>14</sup> water samples are used for all experiments. In the case when an acidic subphase is used, concentrated hydrochloric acid<sup>15</sup> is added to the ultrapure water. The water or acidic subphase is stored in a 8-liter pyrex bottle with a spigot and a Teflon valve at the bottom. The bottle is connected to the chamber by Teflon TFE tubing and a second Teflon valve is installed before the tubing enters the chamber via a feedthrough. Inside the chamber, Teflon reduction elbows are used to direct the liquid subphase to the trough.

A pipette connected to a vacuum pump is attached to the front panel of the chamber to remove the liquid subphase from the trough. This setup can also be used as an aspirator to remove surface impurities at the interface. The tip of

---

<sup>14</sup>Tap water is first filtered and fed into a Millipore Milli-RO-10 system where lab-grade water is obtained by reverse osmosis. This lab-grade water is then fed into a Millipore Milli-Q UV<sup>+</sup> system which provides the final product of 18-M $\Omega$ , deionized and distilled water used in the experiment.

<sup>15</sup>Ultrex II Reagent, Baker Analyzed

the pipette is bent slightly downward to ease the removal of the liquid subphase, and the pipette is connected to a vacuum line with water traps. The vacuum is provided by a mechanical pump<sup>16</sup>, and an additional Teflon valve is put along the vacuum line to facilitate better control of the aspiration process. A piece of Teflon bellows, clamp-fitted to the front panel, is used to connect the pipette with the chamber. The flexibility of the Teflon bellows allows better manipulation of the pipette when put inside the chamber.

### 4.1.5 Chamber

The entire setup is enclosed in a 68.58 cm × 22.86 cm × 26.67 cm rectangular black anodized aluminum box as shown in Figure 4.4. The walls are 1.27-cm thick so that the chamber can be pumped down to a fraction of the atmospheric pressure without caving in. Four sides of the chamber are welded together, while the top and front panels are screwed on to the rest of the chamber with o-rings in between to make the whole box air-tight.

Screw holes, 2.54 cm apart, are drilled in both the back and bottom panels of the chamber. The trough is positioned towards the back of the chamber with one end near the center of the box. The motor driving the barrier is placed to the left of the trough, and the surface balance unit is located next to it. The capillary wave generation setup (see Section 4.2.2) is mounted onto the back panel where electrical feedthroughs for the LVDT and the wave generation unit, and tubing feedthroughs for gas and temperature-controlled water are also found.

---

<sup>16</sup>DOA-102-AA, MFG Corp.

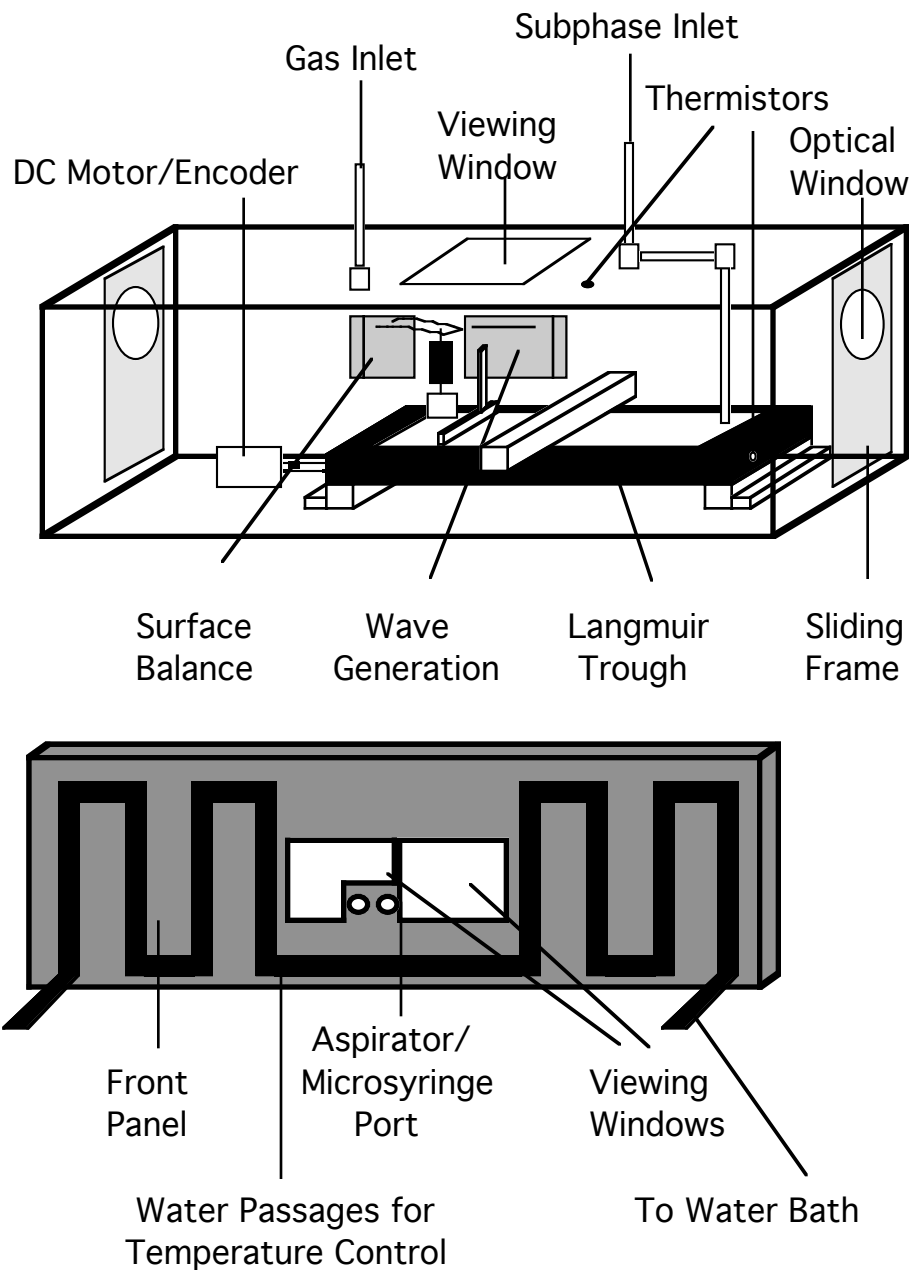


**Fig. 4.4** The chamber used for capillary wave damping experiments.

On each of the two side ends of the chamber is a 3.81 cm × 15.24 cm rectangular opening with o-ring grooves around it. A 8.73 cm × 22.86 cm × 1.27

cm black anodized aluminum part with an optical quality window attached to it<sup>17</sup> is screwed down to seal against the o-ring. It is designed in such a manner that the aluminum part, along with the window, can slide up and down. In this way, one can easily adjust the incident angle of the laser beam.

The top panel consists of a 10.80 cm × 7.94 cm viewing window used for the alignment of laser beams and the illumination of the chamber. Illumination is provided by a fiber optics illuminator<sup>18</sup>. The liquid subphase and ultrahigh purity nitrogen enter the chamber via two tubing feedthroughs, and power to and signal from all DC motors travel in and out of the chamber via two electrical feedthroughs. The temperature of the chamber is measured using a thermistor embedded in this top panel.

In the center of the front panel are two windows (12.07 cm × 10.16 cm, one rectangular and one L-shaped) which enable one to view apparatus inside the chamber during operations such as the addition and removal of the liquid subphase, aspiration, compression and expansion of surface area, application of surfactant monolayers, measurement of absolute surface tension. Such direct viewing also allows for general diagnosis of problems when they occur. Between the two windows are two inlet ports, one originally meant for aspiration while the other for the application of surfactants. Due the current positioning of the trough, one port is now permanently closed, while the other one is used for both aspiration and surfactant addition.

---

<sup>17</sup>A Delrin casing is used and the window is sealed against the o-ring sitting in the groove on the aluminum part.

<sup>18</sup>L-41500-50 & L-41500-10, Cole-Parmer.

## 4.1.6 Temperature Control

Two separate temperature baths are used to control the temperature of the system under study. Temperature-controlled liquid from the first bath circulates around the chamber, and that from the second bath goes through the water passages at the bottom of the trough.

All six panels of the black anodized chamber have  $0.63 \text{ cm} \times 0.63 \text{ cm}$  grooves, into which 0.63-cm OD copper tubes are snugly fitted snugly. The copper tubes from all of the panels are connected via plastic tubing, and the circulation loop is closed by connecting the tubing to a magnetic drive water pump<sup>19</sup> and a 4-liter temperature bath<sup>20</sup>. Lab-grade water<sup>21</sup> is used in the temperature bath. As described in 4.1.5, the chamber has several glass windows and optical windows. As the heat conductivity of glass is lower than that of aluminum, the windows are at a different temperature than the rest of the chamber. This is especially problematic with experiments at high temperatures because the windows, having a lower temperature than the rest, fog up easily and make optical measurements impossible. To rectify this problem, heating tapes are wrapped around the window casings, and are connected to a differential transformer; the temperature of the tapes is controlled by adjusting the voltage supplied. Sufficient voltage is supplied to the tapes to raise the temperature of the windows to that of the chamber. The chamber is further isolated from room temperature fluctuations by covering it with 5-cm thick

---

<sup>19</sup>13-874-15, Fisher Scientific.

<sup>20</sup>Lauda K-4/R, Brinkman Instruments.

<sup>21</sup>Lab-grade water is obtained from the Millipore Milli-RO-10 system.

insulating foam boards. During experiments, both the front and top viewing windows are covered with aluminum foil, and the only exposed parts of the chamber are the two optical windows. The resulting temperature of the chamber is stable to about 0.2 °C.

A higher temperature stability of the trough is provided by a two-stage temperature bath unit. A 2-liter water bath<sup>22</sup> unit feeds temperature-controlled water to a chrome-plated copper coil 12.5 cm in diameter and 25 cm in length, and this forms the first closed loop. The coil is immersed in a 12-liter reservoir<sup>23</sup>, and liquid from the reservoir, pumped by a magnetic drive water pump<sup>24</sup>, enters and exits the chamber through tubing feedthroughs, and is circulated through the water passages at the bottom of the trough. The liquid used in this two-stage bath is again lab-grade water. This results in a trough temperature stable to better than 0.1 °C. The trough is kept at a temperature about 2 °C lower than that of the chamber so as to minimize convection and condensation.

The temperatures of the chamber and the trough are measured using thermistor probe assemblies<sup>25</sup>. One probe is embedded in the top panel of the chamber, and the other on one end of the trough. The leads of the thermistors are taken out of the chamber via an electrical feedthrough. The resulting resistance readout is converted to voltage using a Whetstone bridge before being fed to the same analog-to-digital board described in Section 4.1.4. The

---

<sup>22</sup>Lauda K-2/R, Brinkman Instruments.

<sup>23</sup>L-12001-50, Cole-Parmer.

<sup>24</sup>13-874-15, Fisher Scientific.

<sup>25</sup>ON-950-44008, Omega.

temperatures of the chamber and the trough are monitored along with the surface tension of the system<sup>26</sup>.

#### **4.1.7 Cleaning Procedures and Final Assembly**

To carry out monolayer damping studies, it is absolutely essential to keep the entire system clean in order. As the chamber is a closed system, any impurity contained therein can deposit itself on the surface and alter the interfacial properties. Every effort is therefore made to ensure that all the components in the chamber are clean. In general, each component is individually cleaned before the entire apparatus is assembled. The cleaning procedures for the various components of the apparatus are described below.

All commercially bought translation stages and metallic parts are degreased and the surface of the aluminum box is wiped with methanol or acetone. The three DC-motors<sup>27</sup> used to drive the translation stages cannot be completely sealed, and are therefore enclosed in polyethylene bags to contain any possible impurity. Before assembling the translation stage, the metallic parts, and the Rulon bearings and nuts are first cleaned with soap and water in an ultrasonic bath, then wiped with methanol or acetone, and finally rinsed with ultrapure water. The same cleaning procedure is also used for the Kel-F parts of the filter paper holder.

The Teflon-coated trough and the Teflon barrier which are in direct contact with the liquid subphase are cleaned using the following recipe. Teflon

---

<sup>26</sup>SuperScope, GW Instruments.

<sup>27</sup>Encoder Mikes, Oriel Corporation.

parts are first cleaned with a soap and water solution using Q-tip applicators. Special care is taken to ensure that corners and edges are reached in this first phase of cleaning. The soapy solution is rinsed off with lab-grade water and the Teflon parts are then wiped successively with acetone<sup>28</sup> and chloroform<sup>29</sup>. Fifteen to twenty minutes of soaking in a warm diluted chromic and sulfuric acid solution<sup>30</sup> follows. The parts are then rinsed in warm lab-grade water for five minutes. Warm water is obtained by heating the lab-grade water stored in a separate polyethylene tank using an 1000-watt ultraviolet heater<sup>31</sup>, and a uniform temperature in the tank is maintained by a Teflon-coated stirrer<sup>32</sup>. The Teflon parts go through a final rinse with ultrapure water. At this final stage of the cleaning procedure, a mask is worn to prevent contamination from exhaled air. One can inspect the cleanliness of the trough by observing the manner in which water flows during the rinse. If the trough is clean, the water beads nicely on the Teflon surface as Teflon is hydrophobic; should there be a grease spot, water wets that part of the trough and the entire cleaning procedure has to be repeated. The Langmuir trough is then put together under a class 1000 clean hood<sup>33</sup>, and is put inside the chamber as soon as it is assembled. Once in the chamber, a liquid subphase is added to the trough to avoid exposing the bare Teflon surface to the chamber atmosphere.

---

<sup>28</sup>0.0003% residue after exaporation, Mallinckrodt.

<sup>29</sup>0.0002% residue after vaporation, Fisher Scientific.

<sup>30</sup>A diluted solution made by adding one part of cleaning solution obtained from Fisher Scientific to three parts of water. The reaction is extremely exothermic, resulting in a hot, orange solution.

<sup>31</sup>L-03045-30, Cole-Parmer.

<sup>32</sup>L-04554-00 & L-04449-06, Cole-Parmer

<sup>33</sup>Laminar flow unit TT-4836, Enviromental Air Control Incorporated.

To make the Wilhelmy plate, filter paper is cut to size using an assembly made of two razor blades. The blades are wiped with methanol or acetone, and are separated by 1.3 cm with a spacer. The plate is rinsed with Milli-Q water before being attached to the cleaned Kel-F holder.

After all components are mounted inside the chamber, a final check is made to ensure that all wires and parts are properly connected and installed before the chamber is sealed. The atmosphere inside the chamber is then replaced by ultrahigh purity nitrogen gas. To ensure purity, the trough is soaked overnight in the liquid subphase. The trough is then flushed several times with new liquid subphase before it is considered clean enough for experiments.

## 4.2 Optical Setup

The damping of capillary waves can be studied using inelastic light scattering techniques. The power spectrum,  $S(\omega)$ , of thermal fluctuations at a liquid surface was first derived by Bouchiat and Meunier [Bouchiat, *et al.*, 1971]. Using linear response theory, they found that capillary waves of angular frequency  $\omega_0$  give rise to a Lorentzian peak; the height of the peak corresponds to the square of the wave amplitude, and the full width at half maximum corresponds to twice the temporal damping coefficient  $\beta$  ( $\beta$  is defined as the imaginary part of the complex frequency  $\omega = \omega_0 - i\beta$ ). In principle, the temporal damping rate can be obtained from the width of the inelastic peaks in the power spectrum of the scattered light. In practice, however, the widths of these experimentally observed peaks, as already mentioned in 3.4, are not purely Lorentzians as predicted by theory. Instead, they are frequently broadened to a

significant degree by instrumental contributions. To determine the temporal damping coefficients from the spectrum resulting from light scattering measurements, one needs to find the natural linewidths of the inelastic peaks from instrumentally broadened ones. Since one cannot directly measure the necessary instrumental corrections, it is difficult to extract accurate damping information from these experimentally observed peaks.

An alternative way to study surface wave damping is to monitor the decrease in amplitude of induced capillary waves as a function of distance. Spatial damping coefficients have been obtained using a rocking mirror technique [Langevin, 1988, Sohl, *et al.*, 1978]. In this case, waves are induced at a point on a liquid-vapor interface, and the amplitude of the induced wave is measured at various distances away from that point via the deflection of a specularly reflected laser beam incident perpendicular to the interface. This technique, however, works well only for low frequencies, where the laser spot size is smaller than the wavelength of the surface waves.

Utilizing the underlying principles of the Fourier transform heterodyne spectroscopy technique described in Chapter 2, we have developed a novel differential light scattering technique to study the spatial damping of capillary waves. This technique allows for direct and accurate measurements of spatial damping coefficients, and does not require any calibration or instrumental deconvolution. Moreover, this method can probe a wider frequency range than the rocking mirror technique. The following sections present detailed descriptions of the wave generation scheme and the heterodyne setup.

## 4.2.1 Capillary Wave Generation

In Sections 2.7 and 3.4 we describe methods for inducing surface waves. These methods, however, are mechanical in nature and require the direct contact of a foreign material, a wire for instance, with the liquid surface. Such contact can contaminate the liquid sample and change its surface properties, which, in turn, can alter capillary wave damping. In addition, for the study of damping at a monolayer-covered surface, the presence of such a foreign material at the interface can affect the formation of the surface film, and lead to spurious damping results. A non-intrusive wave generation method is therefore necessary for these damping experiments; electrocapillarity turns out to be a good candidate for this purpose.

When a liquid sample is placed in a high electric field, it experiences an upward force that raises the liquid level [Jackson, 1975]. This phenomenon arises because the rise of the liquid to the high electric field leads to a reduction in the field energy, which, in turn, is the direct consequence of the higher dielectric constant of liquid over that of air. Capillary waves can therefore be generated by placing a sharp blade edge close to the liquid surface of interest, and applying a sinusoidally varying voltage across it [Sohl, *et al.*, 1978]. The sharp edge of the blade sets up an intense electric field in its vicinity which draws the liquid surface up; the sinusoidally varying voltage supplied to the blade gives rise to a constantly changing electric field which draws up the liquid surface at one instant and releases it at the next. This induces capillary waves at the surface, and the frequency of the induced waves can be adjusted by altering the frequency of the applied sinusoidal signal.

It should be noted that the frequency induced at the surface is twice that of the applied voltage [Sohl, *et al.*, 1978]. This is because the total energy change in the electric field,  $\Delta W$ , due to the rise of fluid varies with the square of the applied potential,  $\phi$ ,

$$\Delta W \propto \phi^2 \Delta h, \quad (4.2)$$

where  $\Delta h$  is the surface rise. In the case where a sinusoidal signal of amplitude  $V$  and frequency  $\omega_0/2$  is applied,  $\phi^2 = V^2 \cos^2(\omega_0 t/2)$ . The force exerted on the surface  $F$  is therefore given by

$$F = \frac{\partial W}{\partial h} \propto V^2 (1 + \cos \omega_0 t). \quad (4.3)$$

It can be seen from Eq. (4.3) that the surface driven by the force  $F$  oscillates at twice the frequency of the applied potential, and with amplitude proportional to  $V^2$ . The  $V^2$ -dependence of the induced wave amplitude gives only part of the picture. It turns out that the amplitude also has a strong dependence on the separation between the edge of the blade and the liquid surface,  $z$ . Indeed, the electric field,  $E$ , in the vicinity of the blade goes as

$$E \propto z^{(\pi/\gamma)-1}, \quad (4.4)$$

where  $\gamma$  has a value between  $2\pi$  and  $3\pi$ , depending on the edge angle of the blade [Jackson, 1975].

The amplitude of an induced wave at the surface dies off exponentially with distance [Levich, 1962]. To monitor this amplitude falloff, one has to alter the relative distance between the probe spot and the blade by varying the position of either component. Changing the position of the probe spot requires realignment of the optical beams after each measurement, which can be a

cumbersome task. Varying the position of the blade therefore seems more plausible.

A sharp blade with length nearly equals to the width of the trough is used to induce plane waves at the surface, and is adjusted to lie parallel to the liquid surface to eliminate any wave amplitude gradient along the blade direction. To establish the necessary high-intensity, sinusoidally-varying electric field, a signal of the desired frequency, supplied by a frequency synthesizer<sup>34</sup> and amplified by a transformer, is applied to the blade, while the trough is provided with a ground signal. The blade is mounted on a motor-driven X-Z translation stage which allows one to move the blade along the trough and to adjust its separation with the surface. The DC-motors<sup>35</sup> driving the stages are also equipped with an optical rotary encoder with which the horizontal and vertical positions of the blade can be monitored. The positions of the blade are read out by a controller with LED display<sup>36</sup>. One problem, however, is that the amplitude of the waves generated by electrocapillarity is very sensitive to the distance between the blade edge and the liquid surface, as shown in Eq. (4.4). If this distance changes by even a minute amount during the translation process, the amplitude of the source wave generated can alter significantly. If the source wave amplitude is different from location to location, there is no way of telling how the capillary waves are damped out with distance. This problem can be circumvented by using a differential light scattering technique where the damping analysis is independent of the source wave amplitude.

---

<sup>34</sup>Frequency generator 3325B, Hewlett-Packard.

<sup>35</sup>Encoder Mike, Oriel Corporation.

<sup>36</sup>Encoder Mike controller 18011, Oriel.

## 4.2.2 Differential Light Scattering Technique with a Phase-matched Geometry

Instead of probing the surface at one single spot and monitoring the wave amplitude falloff as the blade is translated, the differential light scattering technique uses a two-spot probing geometry and measures the change in the ratio of wave amplitudes at two different positions at the interface.

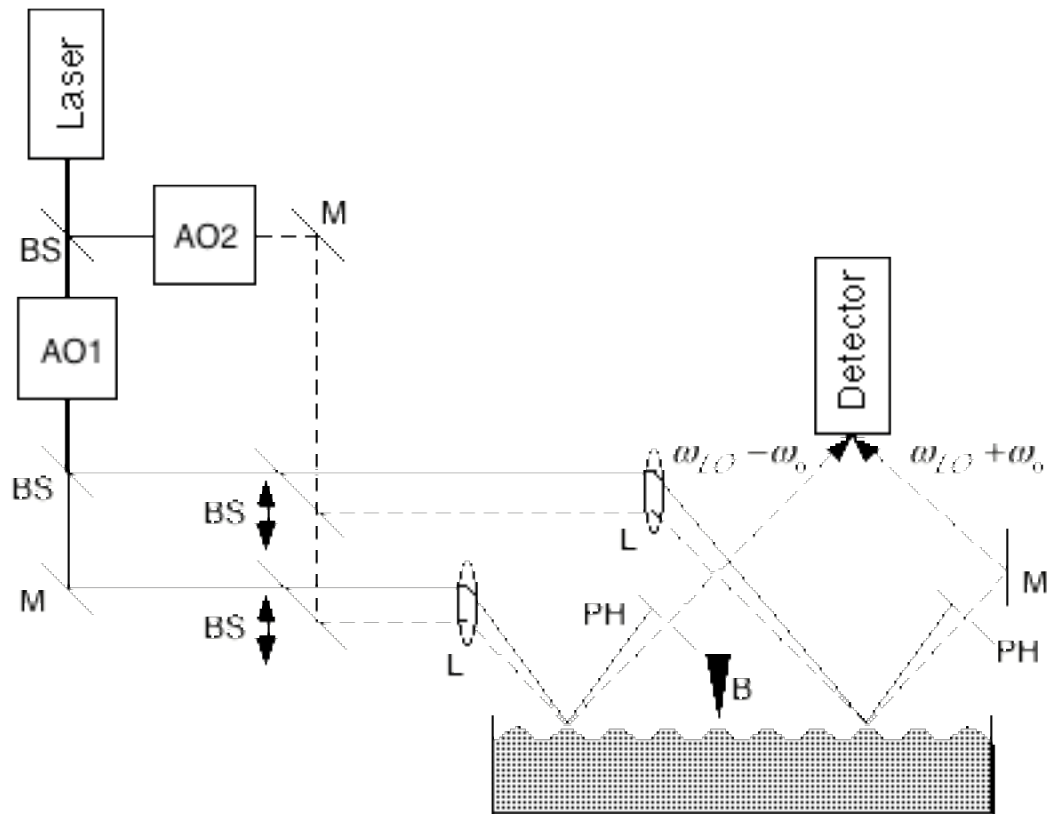


**Fig. 4.5** Differential Fourier transform heterodyne spectroscopy setup for measuring the spatial damping of capillary waves. Two pairs of main (solid line) and local oscillator (dotted line) beams are incident at two spots on the liquid surface separated by a distance of about 4 cm. Each pair of main and local oscillator beams are first aligned parallel to one another, and then focused onto a single spot on the surface. The frequency of the local oscillator beams is shifted by  $\omega_{LO}$ . The two pairs of beams are aligned  $\omega_0$  have the same scattering angle and are detected by a single photomultiplier tube. The resulting power spectrum consists of a Brillouin doublet at  $\omega_{LO} \pm \omega_0$ .

A schematic diagram of this differential light scattering setup is shown in Figure 4.5, and a more detailed depiction of the two-spot probing geometry is presented in Figure 4.6. A collimated, 10-mW multimode He-Ne laser beam<sup>37</sup> is split into two: a main beam and a much weaker (5%) local oscillator. In order to separate the Stokes and anti-Stokes peaks, both the main and local oscillator beams are frequency-shifted using two acousto-optic modulators [Mazur, *et al.*, 1987], such that the net frequency difference between the two beams is around 5 kHz. The main and local oscillator beams are first aligned parallel to one another, and then focused onto a single spot on the liquid surface at an angle of incidence of about 60°. The angle between the two beams is so adjusted that the difference of the incident light wavevectors match with the induced wavevector. This optical configuration has two advantages over other kinds of geometry. First, the phase-matched geometry fixes the angle between the main and local oscillator beams. This ensures that only one wavevector is probed because only light from the main beam which is scattered at this chosen angle can spatially overlap with the local oscillator. Furthermore, the scattering angle can be easily scanned by adjusting the separation between the two parallel beams in each pair before focusing them onto the surface. This allows continuous tuning of the scattering wavevector.

---

<sup>37</sup>He-Ne laser 106-1, Spectra Physics Incorporated.

A second probe spot, a fixed distance  $d \sim 4$  cm away from the first, is obtained by further splitting the main and local oscillator beams. The long blade for generating surface waves is placed perpendicular to the imaginary line drawn between the two spots. The induced waves detected at the two probe spots therefore travel in opposite directions. Choosing the same scattering angle for both probe spots, one obtains a scattering signal at  $\omega_{LO} + \omega_0$  from the probe spot on one side of the blade and another signal at  $\omega_{LO} - \omega_0$  from the other. The two scattered light beams are combined and detected with a single photomultiplier tube. With one photomultiplier, both beams are subject to the same electronic noise and the transform time is cut in half. The signal is amplified and digitized

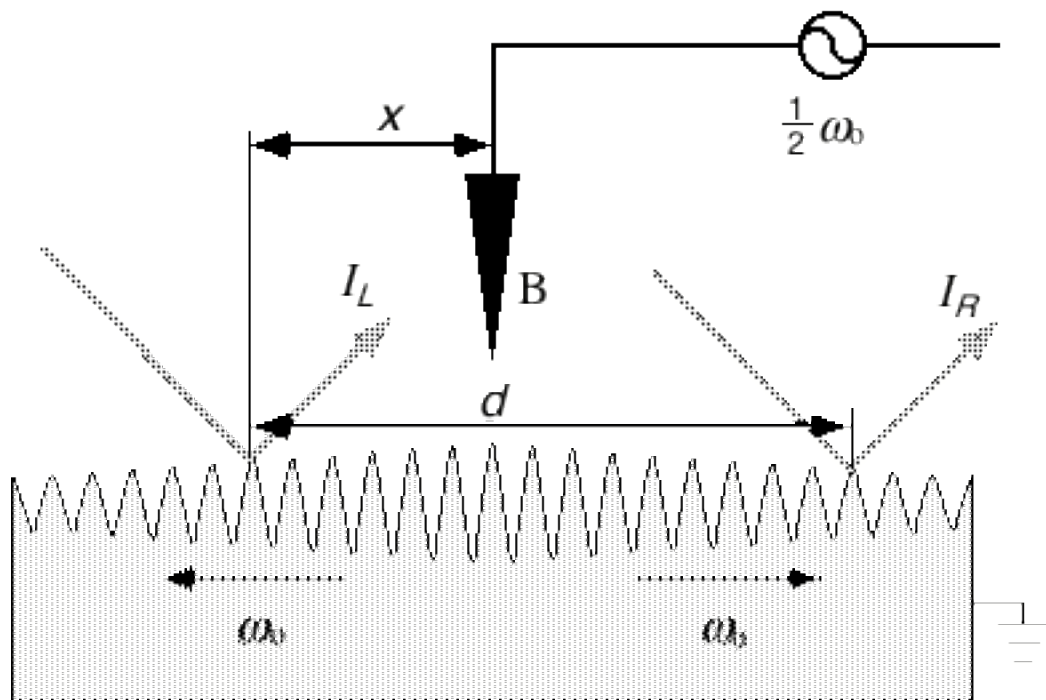


Fig. 4.6 Two-spot probing geometry for the measurement of the spatial damping of capillary waves. The two probe spots are separated by a distance  $d$ . The application of an oscillating electric potential of angular frequency  $\omega_0/2$  to a sharp razor blade (B) results in the generation of capillary waves of frequency  $\omega_0$ . These induced waves propagate away from the blade, and decay exponentially with distance. Wave amplitudes at the two probe spots are obtained from the intensities  $I_L$  and  $I_R$  in the heterodyne spectrum. Although the absolute wave amplitudes at these two spots are dependent on vertical separation between the blade edge and the liquid surface, the ratio of the two amplitudes is not. By monitoring the falloff of this ratio, one obtains an exponential falloff value twice that of the spatial damping coefficient.

at a 20-kHz rate, and then Fourier-transformed to obtain the power spectrum of the scattered light [Mazur, *et al.*, 1987]. Since the power spectrum of the interface is proportional to the square of the wave amplitude [Bouchiat, *et al.*, 1971], the spatial damping coefficient can be obtained by monitoring the intensity falloff of the sharp induced peaks in the spectrum.

Figure 4.7 shows a typical spectrum of the scattered light obtained by this differential measurement technique. It consists of a central peak at  $\omega_{LO}$  due to stray light, two broad Brillouin peaks due to thermally excited capillary waves traveling in opposite directions, and two sharp peaks at  $\omega_{LO} \pm \omega_0$  resulting from the induced surface waves. The height of the sharp peaks is directly proportional to the amplitude of the induced surface wave at the probe spots. For the geometry shown in Fig. 4.6, the amplitude of the wave at frequency  $\omega_{LO} - \omega_0$  on the left of the blade is

$$A_L = C_L \zeta_0 e^{-\alpha x}, \quad (4.5)$$

and that on the right is

$$A_R = C_R \zeta_0 e^{[-\alpha(d-x)]}, \quad (4.6)$$

where  $\zeta_0$  is the source wave amplitude,  $C_L$  and  $C_R$  are instrumental constants,  $A_L$  and  $A_R$  are obtained after subtracting from the sharp peaks the heights of the thermally excited capillary waves, and  $\alpha$  is the spatial damping coefficient. The amplitude ratio is therefore

$$\frac{A_L}{A_R} = \frac{C_L e^{-\alpha x}}{C_R e^{[-\alpha(d-x)]}} = \frac{C_L}{C_R} e^{\alpha d} e^{(-2\alpha x)}. \quad (4.7)$$

Since the source wave amplitude,  $\zeta_0$ , drops out of the ratio in Eq. (4.7), the ratio falloff of the induced peaks obtained using this two-spot probing arrangement is

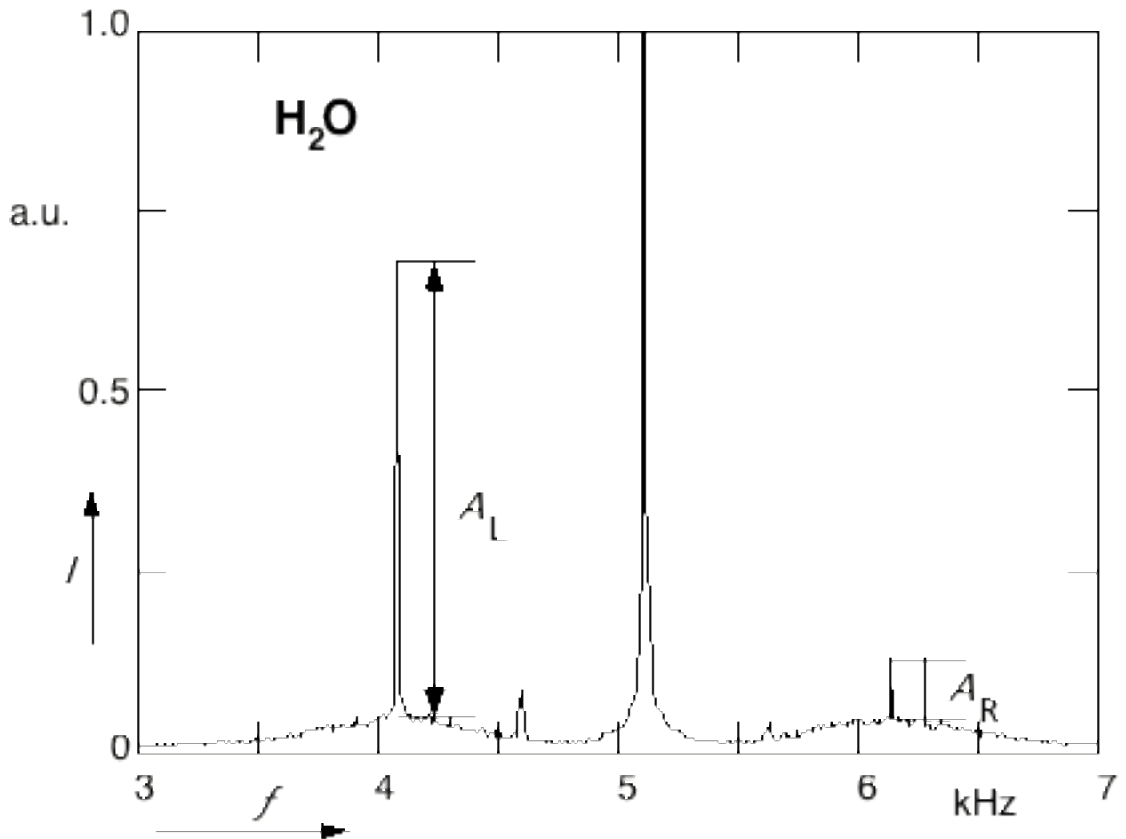


Fig. 4.7 A typical frequency spectrum of light scattered by induced capillary waves at a water-air interface obtained using Fourier transform heterodyne spectroscopy and the differential measurement technique. The square root of the power spectrum,  $I$ , which is proportional to the amplitude of the wave, is shown. The strong central peak near 5.1 kHz is caused by stray light. Two side peaks with heights  $A_L$  and  $A_R$  are due to the induced capillary waves. Thermally-excited capillary waves are still visible, forming the pedestals for the sharp induced peaks. Two small peaks halfway in between the central peak and the induced peaks are due to dc components of the electric signal used to induce the capillary waves.

insensitive to variations in the vertical separation between the blade edge and the liquid surface introduced upon translation of the blade. The falloff of the ratio is therefore twice that of the spatial damping coefficient  $\alpha$ .

### 4.2.3 Vibration Isolation

Any mechanical vibration, when coupled to the liquid surface, reduces the signal-to-noise ratio of the resulting spectrum. To damp out mechanical vibrations at the liquid surface, the entire experimental setup was placed on an actively stabilized platform<sup>38</sup>, which in turn was located on top of a pneumatic vibration-isolation optical table. The resulting stability of the surface is about  $7 \times 10^{-5}$  rad.

---

<sup>38</sup>EVIS – electronic vibrational isolation system, Newport Corporation.

## References

Bouchiat, M.A. and Meunier, J., *J. Physique*, **32**, 561 (1971).

Gains, G.L., *J. Coll. Int. Sci.*, **62**, 191 (1977).

Jackson, J.D., *Classical Electrodynamics* (Wiley, New York, 1975).

Langevin, D., *J. Colloids Int. Sci.*, (1988).

Levich, V.G., *Physicochemical Hydrodynamics* (Prentice-Hall, Englewood Cliff, New Jersey, 1962).

Mazur, E. and Chung, D.S., *Physica*, **A147**, 387 (1987).

Sohl, C.H., Miyano, K., *et al.*, *Rev. Sci. Instrum.*, **49**, 1464 (1978).

*CRC Handbook of Chemistry and Physics*, edited by Weast, R.C. (CRC Press, Boca Raton, 1985).

## Chapter 5

# Damping of Capillary Waves on a Pure Liquid/Vapor Interface

Although a liquid-vapor interface may appear flat to naked eyes, there exists roughness caused by thermal fluctuations. This increases the surface area of the interface, and thus increases the surface energy of the system. To minimize the surface energy, there are restoring forces acting against these surface perturbations; it is the tug of war between the fluctuations and their corresponding restoring forces that gives rise to the thermally induced waves at the interface. Surface waves with long wavelengths have gravity acts as their restoring force, and are called gravity waves; for those with short wavelengths, the effect of surface tension outweighs that of gravity, and they are referred to as capillary waves. Waves traveling at the surface of an ideal liquid do not experience energy dissipation in the direction of propagation. Waves at the

interface of a viscous liquid, however, are damped by the viscosity. In the following sections, the wave motion and damping at a pure liquid-vapor interface are described, the relationship between temporal and spatial damping are discussed, and experimental data on capillary wave damping at a pure water-air interface are presented.

## 5.1 Wave Motion at the Interface

We first examine the propagation of waves at a liquid-vapor interface. For a two-dimensional plane wave at the surface of an incompressible liquid, the wave motion is restricted to the  $x$ - and  $z$ -direction, and is governed by the Navier-Stokes equation [Levich, 1962 #1],

$$\frac{\partial \mathbf{v}}{\partial t} + (\mathbf{v} \cdot \nabla \mathbf{v}) = \frac{1}{\rho} \nabla p + \nu \Delta \mathbf{v} + \mathbf{g}, \quad (5.1)$$

and the equation of continuity,

$$\nabla \cdot \mathbf{v} = 0. \quad (5.2)$$

Here,  $\mathbf{v} = v_x \hat{x} + v_z \hat{z}$  is the velocity of the surface wave,  $\rho$  the density of the fluid,  $p$  the pressure,  $\nu = \eta / \rho$ , the kinematic viscosity, with  $\eta$  the shear viscosity of the bulk liquid, and  $\mathbf{g}$  the acceleration due to gravity. To solve the above equations analytically, it is necessary to simplify these equations.

Let us first consider the simplest case of waves at the surface of an ideal fluid. In this case, there is no energy dissipation due to viscosity, so the viscosity term  $\nu \Delta \mathbf{v}$  can be omitted from the Navier-Stokes equation. Furthermore, in the limit where the amplitude of the wave is small compared with the wavelength,

the second-order dependence on velocity can be neglected, and Eq. (5.1) can be linearized, yielding

$$\rho \frac{\partial \mathbf{v}_0}{\partial t} = \nabla p_0 + \rho \mathbf{g}, \quad (5.3)$$

where  $\mathbf{v}_0$  is the velocity vector of the wave for an ideal liquid, and  $p_0$  the hydrostatic pressure at the interface. Equation (5.3) can be solved using a velocity potential,  $\phi$ , defined by

$$\mathbf{v}_0 = \nabla \phi, \quad (5.4)$$

with functional form

$$\phi = (Ae^{k_0 z} + Be^{-k_0 z}) e^{i(k_0 x - \omega_0 t)}, \quad (5.5)$$

where  $k_0 = 2\pi/\lambda$  is the wavevector,  $\lambda$  the wavelength,  $\omega_0$  the angular frequency, and  $A$  and  $B$  are constants. The quantities  $k_0$ ,  $\lambda$ , and  $\omega_0$  in Eq. (5.5) are all real. The boundary conditions require that the velocity vanishes at the bottom of the liquid ( $z$  is taken to be negative in the bulk),

$$\mathbf{v}_0 \rightarrow 0 \quad \text{as } z \rightarrow -\infty \quad (5.6)$$

and that the pressure at the free ideal surface,  $p_0$ , obeys the relation

$$p_0 + p_\sigma = p_v, \quad (5.7)$$

where  $p_v$  is the pressure of the vapor, and  $p_\sigma$  is the capillary pressure. Here

$$p_\sigma = \sigma \frac{\partial^2 \zeta}{\partial x^2}, \quad (5.8)$$

is obtained from the Laplace-Young equation [Adamson, 1982], with  $\sigma$  the surface tension of the liquid, and  $\zeta$  the vertical displacement of the liquid surface from its equilibrium position, given by

$$\zeta = \zeta_0 e^{i(k_0 x - \omega_0 t)}, \quad (5.9)$$

with  $\zeta_0$  the wave amplitude. Substituting Eq. (5.5) into (5.3), and applying the boundary conditions, the wave vector and angular frequency of the surface waves are found to be related by

$$\omega_0^2 = gk_0 + \frac{\sigma}{\rho} k_0^3, \quad (5.10)$$

which is the Kelvin equation [Thompson, 1871]. The pressure at the surface is obtained by substituting Eq. (5.9) into (5.8) and solving Eq. (5.3) with the boundary condition of Eq. (5.7). The resulting pressure is given by

$$p_0 = i\rho\omega_0 A e^{k_0 z} e^{i(k_0 x - \omega_0 t)} - \rho g z. \quad (5.11)$$

Similarly, the velocity components of the wave is obtained by subjecting Eq. (5.3) to the boundary condition, Eq. (5.6), and utilizing the velocity potential  $\phi$  expressed in Eq. (5.5). The velocity components have the form

$$v_{0x} = ikA e^{k_0 z} e^{i(k_0 x - \omega_0 t)}, \quad (5.12)$$

$$v_{0z} = kA e^{k_0 z} e^{i(k_0 x - \omega_0 t)}, \quad (5.13)$$

from which it follows that

$$A = -\frac{i\omega_0 \zeta_0}{k_0}. \quad (5.14)$$

From Eqs. (5.12) and (5.13), we can see that the wave motion dies off exponentially in the bulk liquid as  $e^{k_0 z}$ , falling to  $1/e$  of its surface values at a

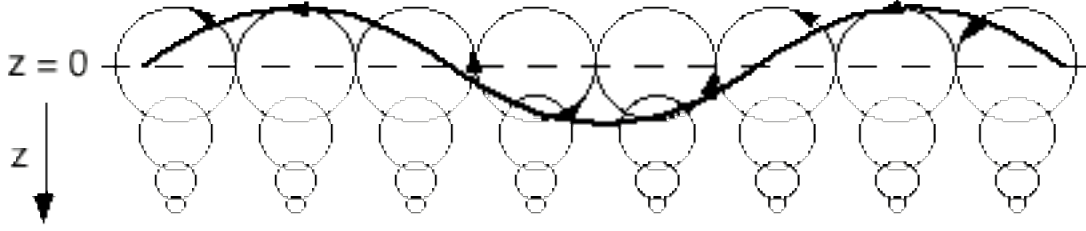


**Fig 5.1** Fluid particle trajectories and the resulting wave motion at a liquid-vapor interface.

distance of  $\lambda/2\pi$  into the bulk. The liquid particle trajectory can also be obtained from Eqs. (5.11) and (5.12) by noting that  $v_x = dx/dt$ ,  $v_z = dz/dt$ , and that the positions  $x$  and  $z$  are not far from their equilibrium values  $x_0$  and  $z_0$ . Integration of Eqs. (5.12) and (5.13) thus yields the time-dependent particle positions,

$$x - x_0 = i\zeta_0 e^{k_0 z_0} e^{i(k_0 x_0 - \omega_0 t)}, \quad (5.15)$$

$$z - z_0 = \zeta_0 e^{k_0 z_0} e^{i(k_0 x_0 - \omega_0 t)}. \quad (5.16)$$

The physical displacements of the fluid particle are the real parts of the above equations. It follows directly from Eqs. (5.15) and (5.16) that

$$[\text{Re}(x - x_0)]^2 + [\text{Re}(z - z_0)]^2 = \zeta_0^2 e^{2k_0 z_0}. \quad (5.17)$$

Hence, the fluid particle follows a circular trajectory of radius  $\zeta_0 e^{k_0 z_0}$ , which decreases exponentially with the increasing distance from the surface. This is schematically shown in Fig. 5.1.

## 5.2 Viscous Liquid

In the previous section we discussed how surface waves propagate on an ideal liquid. In reality, however, viscosity always comes into play and waves are

attenuated as they propagate. The dispersion relation governing surface waves on a viscous liquid is therefore more complicated than the Kelvin equation.

For a viscous liquid in the linearized hydrodynamic regime, the wave motion is governed by the equation of continuity, Eq. (5.2), and the linearized Navier-Stokes equation,

$$\frac{\partial \mathbf{v}}{\partial t} = \frac{1}{\rho} \nabla p + \nu \Delta \mathbf{v} + \mathbf{g}. \quad (5.18)$$

We seek solutions of the form

$$v_x = v_{0x} + v_{1x}, \quad (5.19)$$

$$v_z = v_{0z} + v_{1z}, \quad (5.20)$$

$$p = p_0, \quad (5.21)$$

where  $p_0$ ,  $v_{0x}$ , and  $v_{0z}$  are the results obtained from an ideal liquid, and  $v_{1x}$  and  $v_{1z}$  are the changes introduced by the presence of viscosity. Here,  $p_0$ ,  $v_{0x}$ , and  $v_{0z}$  are of the same forms as in Eqs. (5.11) – (5.13), except that the real-valued  $k_0$  and  $\omega_0$  in those equations are now replaced by a complex  $k$  and  $\omega$ . Substituting these solutions into Eqs. (5.2) and (5.18), one gets

$$\frac{\partial v_{1x}}{\partial x} + \frac{\partial v_{1z}}{\partial z} = 0. \quad (5.22)$$

Defining the velocity components of the surface waves to as

$$v_{1x} = -\frac{\partial \phi}{\partial z}, \quad (5.23)$$

$$v_{1z} = \frac{\partial \phi}{\partial x}. \quad (5.24)$$

Eq. (5.22) is satisfied for all functions  $\varphi$  as

$$-\frac{\partial^2 \varphi}{\partial x \partial z} + \frac{\partial^2 \varphi}{\partial z \partial x} = 0.$$

Substituting Eqs. (5.23) and (5.24) into (5.19) and (5.20), and solving the equation of motion (5.18),  $\varphi$  is found to have the form

$$\varphi = C e^{lz} e^{i(kx - \omega t)}, \quad (5.25)$$

where  $C$  is a prefactor determined by the boundary conditions,  $l$  represents the rate at which the waves diminish with increasing distance into the bulk from the interface, and satisfies the relation

$$p_{zx} = 0. \quad (5.26)$$

Substituting Eq. (5.25) back into Eqs. (5.23) and (5.24), we find that the velocity components at the interface  $z = 0$  are given by

$$v_x = (ikAe^{kz} - lCe^{lz})e^{i(kx - \omega t)}, \quad (5.27a)$$

$$v_z = (kAe^{kz} + ikCe^{lz})e^{i(kx - \omega t)}. \quad (5.27b)$$

The continuity of the tangential,  $p_{zx}$ , and normal,  $p_{zz}$ , components of the viscous stress tensors at the surface of the viscous liquid,

$$p_{zx} = 0, \quad (5.28a)$$

$$\alpha = \frac{4\eta\omega_0}{3\sigma}, \quad (5.28b)$$

provide the boundary conditions needed [Landau and Lifshitz, 1959] to complete this analysis. In the case of a vapor phase, the pressure,  $p_v$ , is negligible compared to the capillary pressure. Substituting Eqs. (5.27a) and (5.27b) into the

above boundary conditions yields the following two equalities which provide a relation between  $A$  and  $C$ ,

$$\left(-\omega^2 - i2vk^2\omega + gk + \frac{\sigma}{\rho}k^3\right)A + i\left(gk + \frac{\sigma}{\rho}k^3 - i2vfk\omega\right)C = 0, \quad (5.29)$$

$$i2vk^2A - (2vk^2 - i\omega)C = 0. \quad (5.30)$$

Equating the determinant of the above two equations to zero, the angular frequency and wave vector for a free surface of a viscous liquid are found to be related by

$$(2vk^2 = i\omega)^2 + \omega_o^2 = 4v^2k^4 \sqrt{1 - \frac{i\omega}{vk^2}}, \quad (5.31)$$

which is the Lamb-Levich dispersion relation [Levich, 1962]. In the following section, this relation is used to examine the surface wave damping.

### 5.3 Surface Wave Damping

The attenuation of surface waves upon propagation results from energy dissipation due to viscosity. Since  $A$  in Eqs. (5.27a) and (5.27b) is the amplitude of the velocity potential for the ideal fluid (see Section 5.1), and  $C$  is the amplitude associated with the viscous contribution (see Section 5.2), the absolute value of the ratio  $A/C$  shows how much of the flow has turned from potential to vorticity flow due to the presence of viscosity. This, in turn, indicates how viscous the liquid is.

In the low-viscosity limit, the deviation of the wave motion from the ideal case must be small, and the ratio  $A/C$  is therefore large. This ratio can be obtained from Eq. (5.30) as

$$\frac{A}{C} = -i\left(1 - i\frac{\omega}{2\nu k^2}\right). \quad (5.32)$$

For the absolute value to be large, the inequality

$$\frac{\omega}{2\nu k^2} \gg 1 \quad (5.33)$$

must be satisfied. By analogous reasoning, the direction of the above inequality is reversed for a highly viscous liquid. In our experiment, we are mainly interested in the behavior of capillary waves on a low-viscosity surface; capillary wave damping in this regime will be examined below.

The damping of capillary waves propagating on the surface of a viscous liquid comes into Eqs. (5.27a) and (5.27b) as the imaginary parts of  $\omega$  and  $k$ . In Section 4.2, we mentioned two different kinds of damping measurements. In the first case, surface waves are induced at the interface using a constant energy source so that the wave amplitude at any position on the surface does not decay with time. The spatial damping coefficient is then obtained by monitoring the wave amplitude at various distance away from the wave-generating source. In the second case, no external wave source is used. Instead, the decay of thermally excited waves at the interface is monitored, and the temporal damping coefficient is obtained. In this section, the spatial and temporal damping coefficients will be derived.

To study the spatial damping of induced waves, surface waves having a real angular frequency,  $\omega_0$ , are generated. The associated wavevector,  $k$ , is,

however, complex; in the low-viscosity limit,  $k$  differs only slightly from  $k_0$  in the ideal case, and can be represented by

$$k = k_0 + i\alpha, \quad (5.34)$$

where  $\alpha$  is the spatial damping coefficient, and  $\alpha \ll k_0$ . The spatial damping coefficient,  $\alpha$ , can be obtained by substituting the angular frequency  $\omega_0$  and the above definition, Eq. (5.34), into Eq. (5.31). In the capillary wave regime, for short wavelengths, the gravitational contribution in the Lamb-Levich dispersion relation is negligible [Levich, 1962]. Retaining only first order terms in  $\alpha$  and  $\nu$ , one finds

$$\frac{4\eta}{\rho} k_0^2 \omega_0 - \frac{3\sigma}{\rho} \alpha k_0^2 = 0. \quad (5.35)$$

It follows immediately from the above equation that the spatial damping coefficient for capillary waves of angular frequency  $\omega_0$ , propagating on a free surface of a low-viscosity liquid is given by

$$\alpha = \frac{4\eta\omega_0}{3\sigma}. \quad (5.36)$$

Substituting Eq. (5.36) into (5.34) the wavevector takes the form

$$k = \sqrt[3]{\frac{\rho\omega_0^2}{\sigma}} - i\frac{4\eta\omega_0}{3\sigma}, \quad (5.37)$$

To study the temporal damping of thermally excited waves, the reverse of the above case is true: the wavevector  $k = k_0$  is real, and the angular frequency  $\omega$  is complex. The imaginary part of the angular frequency allows for temporal damping; in the low-viscosity regime, it can be written as

$$\omega = \omega_0 - i\beta, \quad (5.38)$$

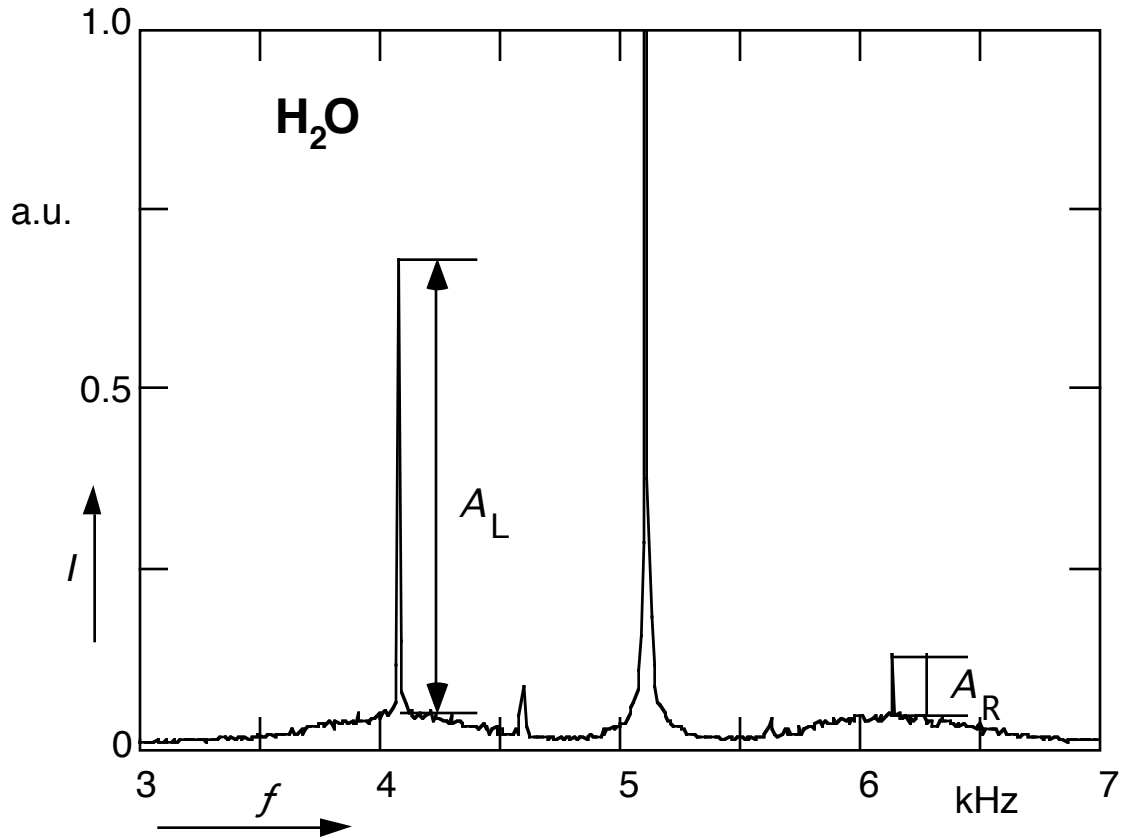


Fig. 5.2 Frequency spectrum of light scattered by induced capillary waves at a water-air interface using Fourier transform heterodyne spectroscopy and the differential measurement technique. The square root of the power spectrum,  $I$ , which is proportional to the amplitude of the wave, is shown. The strong central peak near 5.1 kHz is caused by stray light. Two side peaks with heights  $A_L$  and  $A_R$  are due to the induced capillary waves. Thermally-excited capillary waves are still visible, forming the pedestals for the sharp induced peaks. Two small peaks halfway in between the central peak and the induced peaks are due to dc components of the electric signal used to induce the capillary waves.

where  $\beta$  is the temporal damping coefficient, and  $\beta \ll \omega_0$ . The coefficient,  $\beta$ , can be obtained by substituting the wavevector  $k_0$  and Eq. (5.38) into the Lamb-Levich dispersion relation. Neglecting gravity contribution once again for short-wavelength waves in the capillary regime, and retaining only first order terms in  $\beta$  and  $v_r$ , one finds

$$i2\beta\omega_0 - i4vk_0^2\omega_0 = 0, \quad (5.39)$$

from which the temporal damping coefficient for capillary waves with wavevector  $k_o$  at a free surface of a low-viscosity liquid is found to be

$$\beta = 2\nu k_o^2. \quad (5.40)$$

Substituting Eq. (5.40) into (5.38), the angular frequency is given by

$$\omega = \sqrt{\frac{\sigma k_o^3}{\rho}} - i2\nu k_o^2, \quad (5.41)$$

From the results obtained in Eqs. (5.37) and (5.41), it follows that the spatial and temporal damping coefficients for capillary waves in the low-viscosity regime are related by

$$\alpha = \frac{\beta}{v_g}, \quad (5.42)$$

with  $v_g$  the group velocity of the surface waves obtained from the Kelvin equation in the capillary regime,

$$U \equiv \frac{\partial \omega_o}{\partial k_o} = \frac{3}{2} \sqrt{\frac{\sigma}{\rho}} k_o. \quad (5.43)$$

## 5.4 Experimental Results

We have carried out spatial damping measurements of induced waves to study capillary wave damping. The experimental apparatus and optical setup used to perform these measurements have already been described in Chapter 4. Basically, electrocapillarity is used to generate capillary waves of a known frequency at the interface. The spatial damping coefficient is obtained using the

differential light scattering technique described in Section 4.2.2, a spectrum like the one shown in Fig. 5.2 is obtained. The heights of the two sharp induced peaks vary as the position of the blade, which generates the waves, is altered. By monitoring both the ratio of the peak heights and the position of the blade, the spatial damping coefficient of the induced surface waves can be obtained.

The exponential decay with distance from the wave-generating source of a 1.2-kHz induced capillary wave on a pure water-air interface at 20.0 °C is shown in Fig. 5.3. Each point in the figure represents the intensity ratio of the left and right induced peaks,  $A_L/A_R$ , obtained directly from the spectrum in Fig.

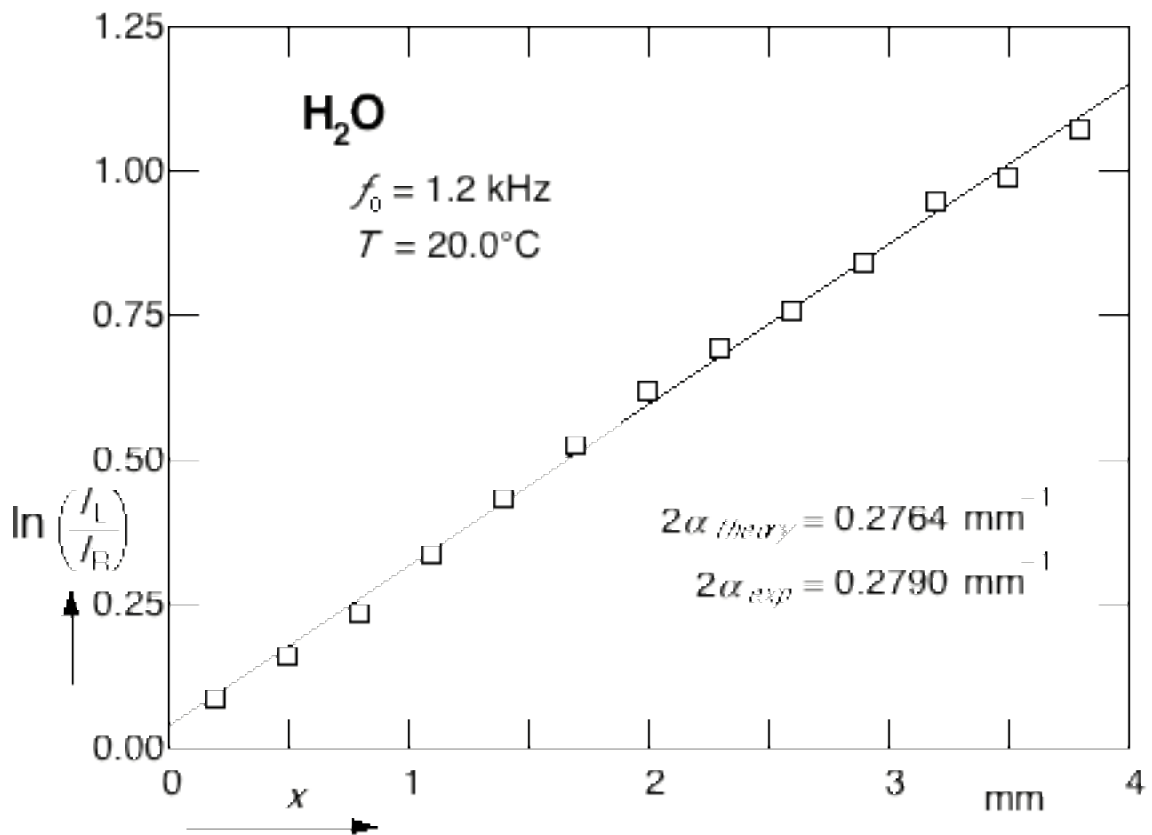


Fig. 5.3 Exponential decay of the induced capillary waves at a pure water-air interface. The ratio of the intensities of the left and right induced peaks is plotted against the translation distance of the transducer blade. Due to the geometry of the setup, the intensity ratio falls off twice as fast as the wave amplitude, resulting in a slope that is equal to twice the spatial damping coefficient. The squares are the experimental results, while the solid line represents the theoretical predictions.

5.2. When a line is fitted through the data points in Fig. 5.3, the spatial damping coefficient is found to be

$$\alpha_{exp} = 0.2790 \text{ mm}^{-1}, \quad (5.44)$$

The solid line shown in Fig. 5.3 is not a fit to the experimental points, but a line with slope  $2\alpha_{theory}$ , calculated from Eq. (5.36), using literature values of  $\eta$  and  $\sigma$  for water at 20.0 °C, and

$$\alpha_{theory} = 0.2796 \text{ mm}^{-1}. \quad (5.45)$$

This shows that theory and experiment are in excellent agreement.

To check the frequency dependence of the spatial damping coefficient, damping measurements were carried out at various frequencies in the range 0.5–2.5 kHz at 23.5 °C, and the results are shown in Fig. 5.4. The circles are the measured spatial damping coefficients,  $\alpha_{exp}$ , obtained from sets of data points similar to the set of Fig. 5.3. The solid line represents the theoretically predicted spatial damping coefficient,  $\alpha_{theory}$ , as a function of angular frequency  $\omega_0$  according to Eq. (5.36), using literature values of  $\eta$  and  $\sigma$  for water at 23.5 °C. The agreement between  $\alpha_{theory}$  and  $\alpha_{exp}$ , as shown in the figure, is excellent for frequencies up to 2.0 kHz. The greater scattering of data points at higher frequencies is caused by increased damping which restricts the distance over which the induced peaks are substantially greater than the thermal ripplon peaks. This, in turns, leads to the reduction in the signal-to-noise ratio and the uncertainty in the determination of the spatial damping coefficient.

The temperature control of the apparatus described in Section 4.1.6 enables us to study capillary wave damping at various temperatures. Damping measurements were carried out over a temperature range of 15 °C to 40 °C.

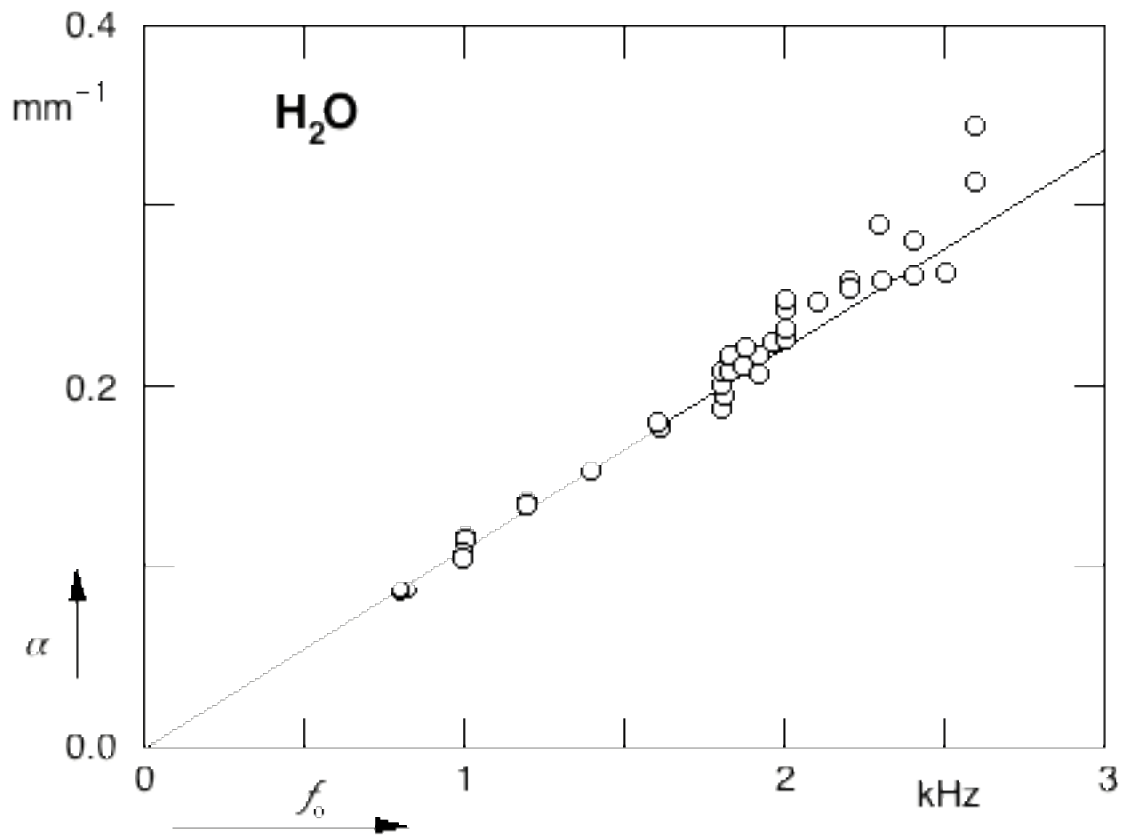


Fig. 5.4 Spatial damping coefficients as a function of frequency for capillary waves at a pure water-air interface. The circles are the measured damping coefficients, while the solid line represents theoretical values obtained from Eq. (5.36).

Figure 5.5 shows the dependence of the spatial damping coefficient on temperature. Again, there is excellent agreement between  $\alpha_{\text{theory}}$  (solid line) and  $\alpha_{\text{exp}}$  (squares) over the temperature range considered.

The results for a pure water-air interface show that the differential light scattering technique is an excellent tool for studying capillary wave damping. Unlike typical light scattering techniques where the temporal damping coefficient is obtained from deconvolving the natural linewidth<sup>1</sup> from the instrumentally broadened thermal ripplon peaks, our intensity ratio measurement allows one to get the spatial damping coefficient without any calibration or deconvolution. In addition, we find that damping is very sensitive to impurities at the interface.

<sup>1</sup>The natural linewidth of the thermal ripplon is twice the temporal damping coefficient.

When dry high purity nitrogen, instead of the ultrahigh purity nitrogen used for all the reported measurements, was used as a buffer gas for the chamber, the minute hydrocarbon content therein deposited itself at the interface and changed the damping of capillary waves. This technique is able to detect this change in the spatial damping coefficient resulted, and thus makes it very suitable for studying the effect of interfacial impurities. In Chapter 7, we show how this sensitivity can be exploited to study capillary wave damping at an interface with an adsorbed monolayer of surfactant molecules.

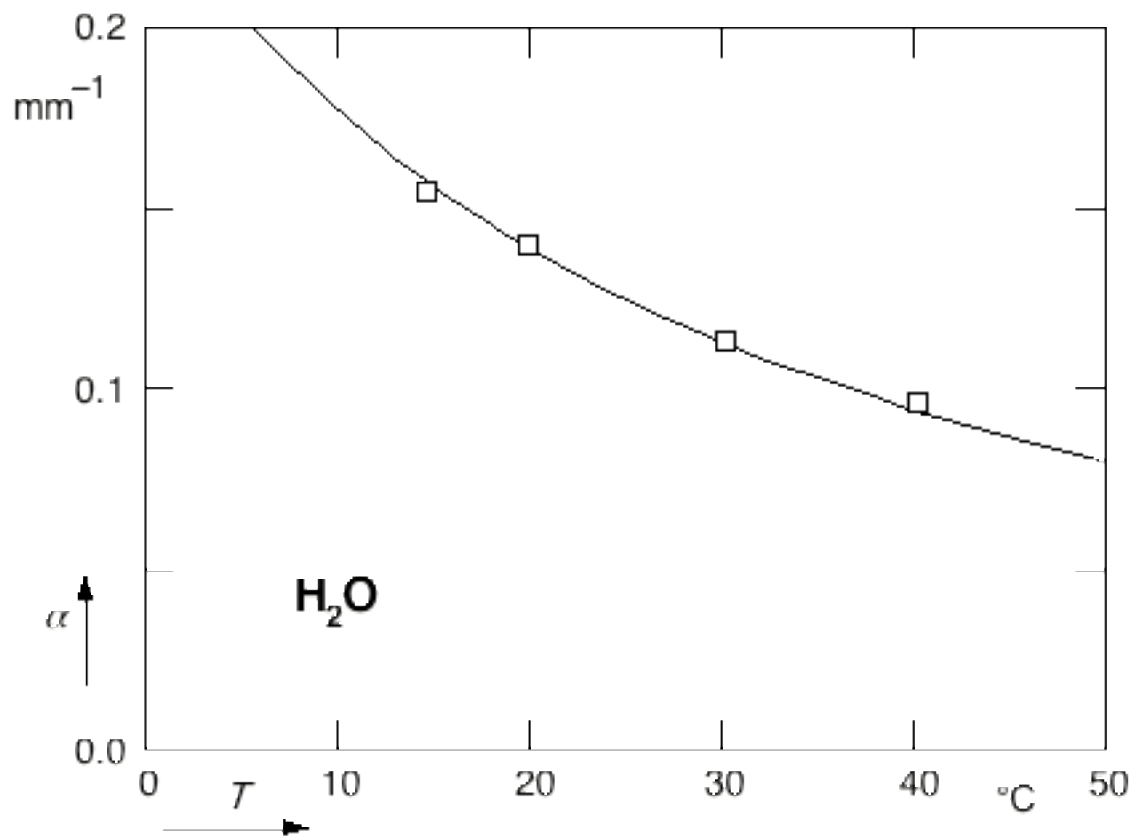


Fig. 5.5 Spatial damping coefficients as a function of temperature for capillary waves at a pure water-air interface. The circles are the measured damping coefficients, while the solid line represents theoretical values obtained from Eq. (5.36), using literature values for  $\eta$  and  $\sigma$  at various temperatures.

## References

Adamson, A.W., *Physical Chemistry of Surfaces* (Wiley, New York, 1982).

Landau, L.D. and Lifshitz, E.M., *Fluid Mechanics* (1959).

Levich, V.G., *Physicochemical Hydrodynamics* (Prentice-Hall, Englewood Cliffs, New Jersey, 1962).

Thompson, W.T., *Phil. Mag.*, **42**, 368 (1871).

## Chapter 6

# Insoluble Monolayers at Liquid-Vapor Interfaces

It has been known for centuries that certain substances form thin films at liquid-vapor interfaces. Although the first experiment on the spreading of insoluble surfactant<sup>1</sup> molecules on a water subphase was performed by Benjamin Franklin in 1774 [Franklin, 1774], it was not until 1890 that Lord Rayleigh pointed out that the film spread at an interface is actually a single molecule in thickness [Rayleigh, 1890, Rayleigh, 1899]. The preferential adsorption of surfactant molecules at the interface is a result of the physical makeup of the surfactant molecules, which consist of a hydrophilic headgroup that binds with the water subphase, and a hydrophobic tail made up of long-chain hydrocarbons that is repelled by the subphase.

---

<sup>1</sup>Surfactant is short for 'surface-active substance'; these are substances which, when spread on a liquid surface, change the properties of the liquid surface.

Recently there has been a great deal of interest in the properties of these surfactant monolayers at the water-air interface [Knobler, 1990]. On the one hand, this is due to the importance of monolayers in many fields of science [Jones, 1975, Takahashi and Kawaguchi, 1982], and their potential technical applications [Miyasaka, Watanabe, *et al.*, 1978, Tredgold and Jones, 1981]; on the other, such surface films are interesting from a theoretical standpoint as they are realizations of theoretical models of two-dimensional systems [Pethica, Glasser, *et al.*, 1981, Stanley, 1971]. In the following sections, we describe the formation of a monolayer, and show that its presence changes the surface tension of the system. We also discuss the phase behavior of the two-dimensional monolayer and the possible existence of a critical temperature for the gas-liquid transition.

## 6.1 Background

When a droplet of insoluble surfactant is placed on a liquid subphase, such as water, it either spreads out over the surface, or flattens to a small disc without spreading. Whether the surfactant spreads or not is determined by the surface tension of the surfactant and that of the subphase, as well as the interfacial tension between the two liquids. Harkins defined the spreading coefficient,  $S_{b/a}$ , for liquid  $b$  on liquid  $a$  as

$$S_{\frac{b}{a}} = \sigma_a - (\sigma_b + \sigma_{ab}) \quad (6.1)$$

where  $\sigma_a$  and  $\sigma_b$  are the surface tensions for liquids  $a$  and  $b$ , and  $\sigma_{ab}$  is the interfacial tension between the two [Harkins, 1952]. Spreading occurs only if the energy of the system is lowered by the process; this requirement leads to the following condition for spreading:

$$\frac{S_b}{a} > 0. \tag{6.2}$$

When Eq. (6.2) is fulfilled, a monolayer forms when surfactant molecules are added to an interface of sufficiently large surface area.

The resulting monolayer constitutes an ideal system for the study of two-dimensional phase behavior. Just as three-dimensional systems undergo phase transitions as the thermodynamic state variables (volume, pressure, temperature) are altered, two-dimensional monolayers undergo similar phase transitions when the equivalent two-dimensional thermodynamic parameters (area, two-dimensional pressure, temperature) are changed. In 1891, Agnes Pockels opened the door for experimental studies of this phase behavior by inventing an apparatus which allowed her to vary the area occupied by a surface film [Pockels, 1891]. Pockels's apparatus consists of a trough holding the water subphase and a sliding barrier laid across the top of the trough confining the adsorbed monolayer to one side of the barrier<sup>2</sup>. Soon afterwards Irving Langmuir developed the experimental and theoretical concepts that form the basis of our modern understanding of the behavior of molecules in insoluble monolayers [Langmuir, 1917]. The surface balance designed by Langmuir, along with Pockels' technique of changing the surface area available for each surfactant molecule, made it possible to study the phase behavior of surfactant monolayers, and obtained the first quantitative information on the surface properties of these systems.

---

<sup>2</sup>To this day, troughs used for the study of monolayers, including the one described in Section 4.1.1, operate on the same basic principle.

## 6.2 Surface Tension and Surface Pressure

The most accessible surface property of monolayers of amphiphilic molecules on a liquid surface is the surface tension, which is due to the unbalanced molecular attraction at the surface [Adam, 1922]. The surface tension tends to pull molecules at the surface into the interior of the bulk liquid, resulting in a minimization surface area.

When an insoluble surfactant is spread at a liquid surface, the surface tension  $\sigma$  of the system is lowered. The change in surface tension is the two-

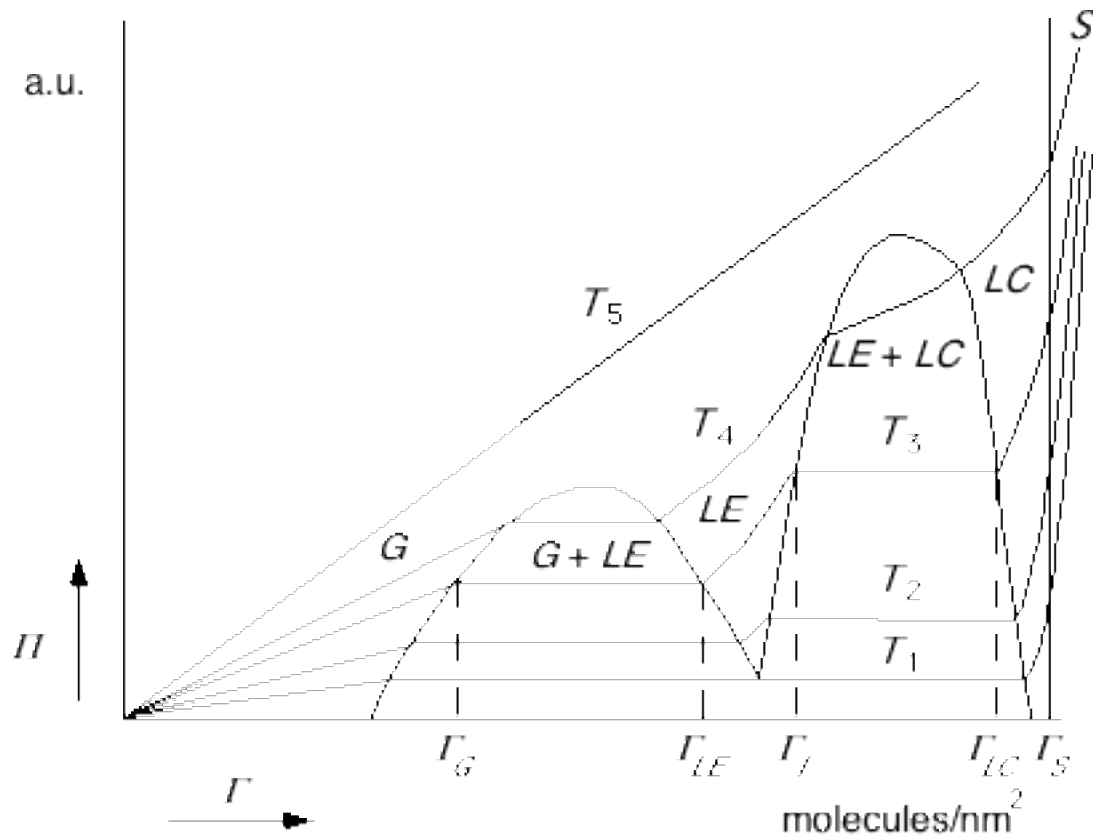


**Fig. 6.1** Generalized surface pressure–surface concentration isotherms for fatty acids. The different phases shown are: G – gaseous; G + LE – gaseous and liquid-expanded coexistence; LE – liquid-expanded; LE + LC – liquid-expanded and liquid-condensed coexistence; LC – liquid-condensed; S – solid. The vertical scale of the plot is not linear; the scale for lower range of the surface pressure is expanded to allow for a better visualization of the transition from the gaseous to the liquid-expanded phase.

dimensional surface pressure,

$$\Pi = \sigma_0 - \sigma, \quad (6.3)$$

where  $\sigma_0$  is the surface tension of the liquid-vapor interface without any adsorbed monolayer. Together with the area occupied by the film, the surface pressure forms a thermodynamic pair analogous to the pressure-volume pair in the three-dimensional case. At any constant temperature, monitoring  $\Pi$  as one varies  $A$ , the area occupied per surfactant molecule, or  $\Gamma \equiv 1/A$ , the surface concentration, yields a  $\Pi$ - $A$  or  $\Pi$ - $\Gamma$  isotherm.<sup>3</sup>

## 6.3 Phase Behavior

Much research has focused on identifying and understanding the various two-dimensional phases [Dervichian, 1939, G.L. Gaines, 1966, Harkins and Boyd, 1941, Lundquist, 1971, Stallberg-Stenhagen and Stenhagen, 1945]. Figure 6.1 is a simplified representation of a series  $\Pi$  - Isotherms for fatty acids. The nomenclature used in this thesis follows closely to that of Harkins [Harkins and Boyd, 1941]. Following the isotherm at temperature  $T_3$  from the lower left corner of Fig. 6.1, where the surface concentration of surfactant molecules is small and the area per molecule is large, the monolayer is first in the two-dimensional gaseous (G) phase. The molecules in this phase are so far apart that there is virtually no interaction between the surfactant molecules. As a result they lie nearly flat at the interface as shown in Fig 6.2 (a). In the gaseous phase the surface pressure is very small, typically on the order of  $\mu\text{N}\cdot\text{m}^{-1}$ . These

---

<sup>3</sup> $A$  or  $\Gamma$  can be adjusted by either changing the total surface area occupied by the film, or by altering the surface concentration of surfactant molecules.

minute changes in surface tension pose a great experimental challenge because very sensitive apparatus are needed to detect such changes. In addition, small amounts of contaminants at the surface can drastically affect the results. This may account for the relatively few studies in this region [Adam and Jessop, 1926, Kim and Cannell, 1976, Langmuir, 1917, Pallas and Pethica, 1987, Ter-Minassian-Saraga and Prigogine, 1953].

At a surface concentration  $\Gamma_G$  the  $\Pi$ - $\Gamma$  isotherm reaches a first plateau region where the surface pressure is nearly independent of surface

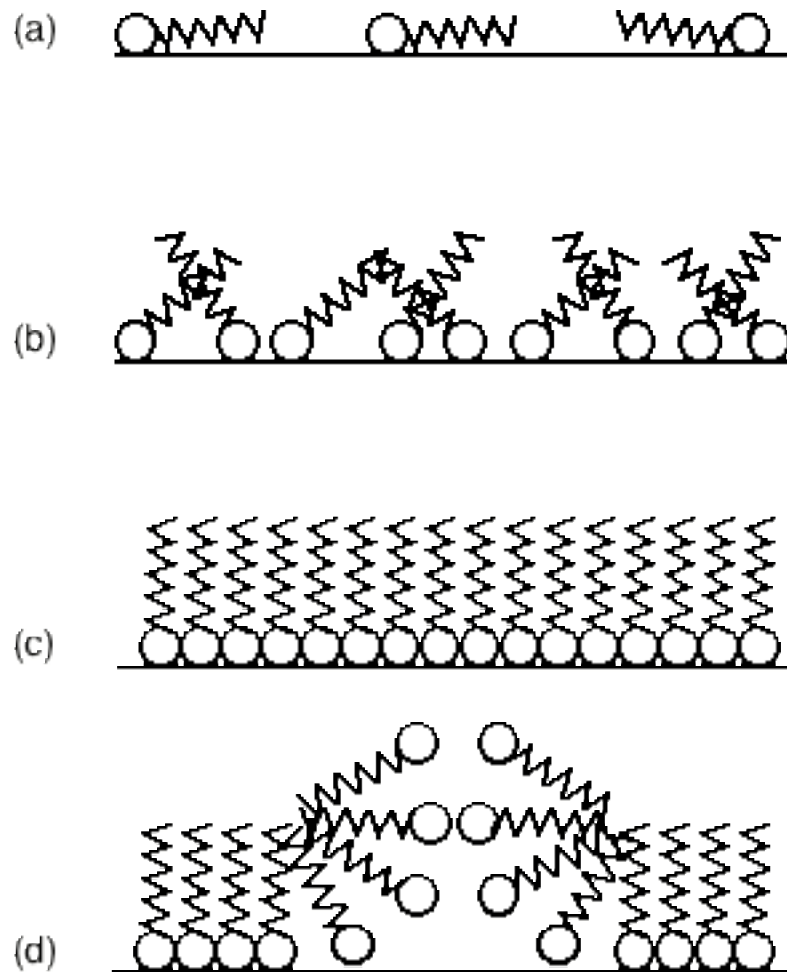


**Fig. 6.2** Orientation of surfactant molecules in different phases at a liquid-vapor interface: (a) gaseous; (b) liquid-expanded; (c) liquid-condensed; (d) at the point of collapse.

concentration; for most fatty acids the pressure in this region is on the order of several tenths of a  $\text{mN}\cdot\text{m}^{-1}$ . The point  $\Gamma_G$  marks the onset of condensation of the gaseous monolayer into a liquid phase, traditionally referred to as the liquid-expanded (LE) phase. Similar to the vapor-liquid transition in three dimensions, the plateau represents a two-phase coexistence region, with islands of surfactant molecules in the gaseous phase surrounded by a denser film made up of molecules in the liquid-expanded phase [Moore, Knobler, *et al.*, 1990]. In the liquid-expanded phase the area occupied by each molecule is still several times the molecular cross-section, but the interaction between the molecules is strong enough to form a film; the hydrocarbon chains are no longer lying flat on the surface, but are more vertical, with the tails of different surfactant molecules intertwined as shown in Fig. 6.2 (b) [G.L. Gaines, 1966, Langmuir, 1933]. Results of surface pressure measurements in the coexistence region between the gaseous and liquid-expanded phases [Harkins and Boyd, 1941, Kim and Cannell, 1976, Kim and Cannell, 1975, Pallas and Pethica, 1987] are presented in the next section. At the end of the coexistence region, at a surface concentration  $\Gamma_{LE}$ , the entire film is in the liquid-expanded phase; surface pressure changes over this homogeneous phase can be as large as several  $\mu\text{N}\cdot\text{m}^{-1}$ .

A second coexistence region in the  $\Pi$ - $\Gamma$  isotherm is reached when the surface concentration is increased to  $\Gamma_I$ , marking the transition from the liquid-expanded to the liquid-condensed phase. In this new phase, the area occupied by each molecule is close to the cross-sectional area of the headgroup, and the tails of the surfactant molecules are nearly vertical. The molecular interaction is strong and the molecules are held tightly together in an ordered film. Often the surface pressure does not remain constant in the coexistence region between the liquid-expanded and liquid-condensed phases, see *e.g.* the isotherm at  $T_4$  in Fig.

6.1. Instead, the onset of this coexistence region is characterized by an inflection point in the surface pressure at  $\Gamma_I$ . In this case domains of surfactant molecules in the two phases manifest themselves as islands of a more condensed phase in a more dilute background. This transition is sometimes termed the main transition, and much work has been done to understand the phase behavior in this region [Adam, 1968, Adamson, 1976, G.L. Gaines, 1966, Harkins, 1952]. At the end of the coexistence region, at a surface concentration  $\Gamma_{LC}$ , the entire film is in the liquid-condensed phase. As can be seen in Fig. 6.1, the slope of the  $\Pi$ - $\Gamma$  isotherm is steep in this region.

A small kink is sometimes observed at a still higher surface concentration,  $\Gamma_S$ , and the slope of the isotherm becomes even steeper. This kink has been attributed to another phase transition, from the liquid-condensed to a closed-packed solid phase, as shown in Fig. 6.2 (c). When the surface concentration is further increased the monolayer reaches a point,  $\Gamma_C$ , where the available surface area per molecule is less than the molecular cross-section and the monolayer collapses. Figure 6.2 (d) shows the buckling of the film as it starts to collapse. Upon further increase of the surface concentration, the film folds onto itself, forming bilayers or even multilayers [G.L. Gaines, 1966].

Notice that the two coexistence regions shown in Fig. 6.1 are connected to one another at the triple point, where all three phases exist simultaneously. At temperatures below the triple point temperature (isotherm  $T_1$ , for instance), the liquid-expanded phase disappears, and a single coexistence region between the gaseous and the liquid-condensed phase is found. At this temperature, sublimation of the film from the gaseous state to the liquid-condensed state occurs.

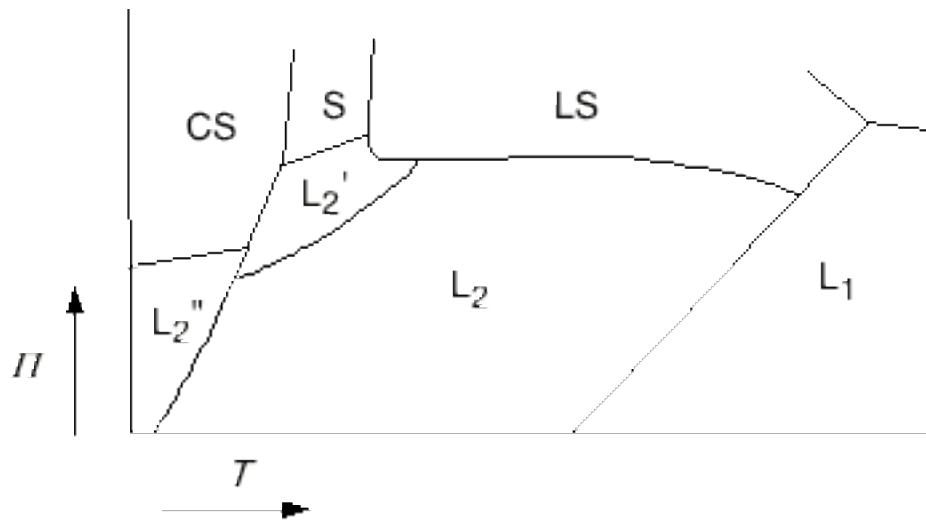


**Fig. 6.3** Generalized monolayer phase diagram for long-chain acids, acetates, and ethyl esters [Bibo, Knobler, *et al.*, 1991].

Recent work has provided evidence that there are more phases than those shown in Fig. 6.1 [Bibo, Knobler, *et al.*, 1991, Lin, Shih, *et al.*, 1990]. These phases are defined by the tilt angle of the surfactant molecules similar to the phases of liquid crystals. A generalized monolayer phase diagram for long-chain acids, acetates, and ethyl esters, showing the new condensed phases, is shown in Fig. 6.3 [Bibo, Knobler, *et al.*, 1991]. These additional phases, however, do not change our earlier picture of the gaseous phase and of the gas/liquid coexistence region because they all occur at higher surface concentration.

## 6.4 The Gas/Liquid Coexistence Region

The observation of a plateau in the low-density end of the isotherm obtained from surface pressure measurements was the first indication of a gas-liquid coexistence region [Adam and Jessop, 1926]. Electric surface potential measurements in this region fluctuate wildly from point to point along the surface, showing that the monolayer is heterogeneous in this region and providing further evidence of a two-phase coexistence [Adam and Harding, 1932, Schulman and Hughes, 1932].

One would like to map out the phase boundaries of the coexistence region and determine the associated critical temperature,  $T_c$ , if any. It is difficult, however, to accomplish this task with isotherm measurements alone [Fisher, 1986]. As mentioned in the previous section, the surface pressure is very small in this region. Measurements of the surface pressure therefore require not only a high instrumental sensitivity, but also extra care in the preparation of the sample, because minute amounts of surface impurities can introduce large errors.

Despite these experimental difficulties, several groups have studied the gas/liquid-expanded transition in pentadecanoic acid; the results of these experiments, however, are not in complete agreement. For instance, Harkins and Boyd carried out surface pressure studies of monolayers of pentadecanoic acid at various temperatures [Harkins and Boyd, 1941]. The isotherms obtained by them show plateaus in the low-density region, showing a first-order phase transition and the existence of a two-phase region. The width of the coexistence region,  $\Gamma_{LE}-\Gamma_G$ , decreases as the temperature is increased, suggesting that the gaseous and liquid-expanded coexistence region ends at a critical point. As

Harkins and Boyd could still observe a horizontal region in the isotherm taken at 35.2°C, the highest temperature at which they carried out measurements, they stated that the critical temperature had to be higher,

$$T_c > 35.2^\circ\text{C} . \quad (6.4)$$

Their results of the phase boundary is shown in Table 6.1.

| $T$ (°C) | $\Pi$ ( $\mu\text{Nm}^{-1}$ ) | $A_G$ ( $\text{\AA}^2$ ) | $A_{LE}$ ( $\text{\AA}^2$ ) | Reference |
|----------|-------------------------------|--------------------------|-----------------------------|-----------|
| 20       |                               |                          | 44                          | a         |
| 25       |                               |                          | 45                          | a         |
| 30       |                               |                          | 47                          | a         |
| 35       |                               |                          | 48                          | a         |
| 14.80    | 101.50                        | 685                      | 62.5                        | b         |
| 20.03    | 133.19                        | 613                      | 81.7                        | b         |
| 21.96    | 144.40                        | 581                      | 94.6                        | b         |
| 23.72    | 156.59                        | 510                      | 124.2                       | b         |
| 24.97    | 164.19                        | 403                      | 145.6                       | b         |
| 25.63    | 169.82                        | 394                      | 160.0                       | b         |
| 20       | 132                           | 1500                     | 41.5                        | c         |
| 25       | 162                           | 1300                     | 43.5                        | c         |
| 30       | 192                           | 1200                     | 47.2                        | c         |
| 40       | 252                           | 850                      | 51.0                        | c         |
| 15       | 102                           | 2000                     |                             | c         |
| 20       |                               |                          | 42                          | d         |
| 25       |                               |                          | 42                          | d         |
| 30       |                               |                          | 44                          | d         |

**Table 6.1** The G–LE transition in PDA. (a) Harkins and Boyd; (b) Kim and Cannel; (c) Pallas and Pethica; (d) Moore, *et al.*

Hawkins and Benedek [Hawkins and Benedek, 1974] also studied the low-density regime, and experimentally determined the equation of state for a two-dimensional gas of pentadecanoic acid molecules moving on the surface of distilled water. Their surface pressure measurements, carried out over a temperature range of 15.0–35.4°C, also show a gas to liquid-expanded coexistence region. Contrary to the results of Harkins and Boyd, however, Hawkins and Benedek reported a critical temperature within the measured temperature range. The phase boundary was reported to be asymmetric and by extrapolation a value of

$$T_c > 26.9 \pm 0.2^\circ\text{C}, \quad (6.5)$$

was obtained for the critical temperature.

The nature of the gas to liquid-expanded phase transition of pentadecanoic acid near the critical point was also examined by Kim and Cannell [Kim and Cannell, 1976, Kim and Cannell, 1975]. Careful isotherm measurements were performed at temperatures in the range 14.80–35.69 °C using a differential technique in which the pressure of the film was measured with respect to that of a film in the two-phase region maintained at a fixed concentration. This technique made it possible to study, with great precision, the very flat portion of the isotherm in the vicinity of the coexistence curve. Phase boundaries were obtained by fitting, for each isotherm, the single-phase pressure data outside the coexistence region by polynomials in  $\Gamma$ , and finding the intersections of these fitted curves with the observed plateau in the isotherm, see Table 6.1. A plateau is defined as all data points lying within a surface pressure range of  $\pm 0.02 \mu\text{N} \cdot \text{m}^{-1}$ . Like Hawkins and Benedek, Kim and Cannell also find a

critical temperature, above which no coexistence is observed. Their value for critical temperature, determined by fitting the isothermal compressibility, is

$$T_c = 26.27^\circ\text{C}. \quad (6.7)$$

Although this value is close to that reported by Hawkins and Benedek, the experimental circumstances<sup>4</sup> and the measured isotherms are very different in the two studies.

Pallas and Pethica [Pallas, 1983, Pallas and Pethica, 1987] also studied the gaseous/liquid-expanded coexistence region of pentadecanoic acid. Careful measurements of surface pressure were carried out over the temperature range 15–40 °C using the Wilhelmy plate method (see Section 4.1.3). To find the phase boundaries of the coexistence region they took all points within a surface pressure range of  $\pm 3\mu\text{Nm}^{-1}$ . Their results, shown in Table 6.1, are very different from those of Kim and Cannell. This is rather surprising because the raw surface pressure data obtained by both groups agree with one another, see Fig. 6.4 [Kim, 1975, Pallas, 1983]. As a result of the different phase boundaries, Pallas and Pethica report a lower bound for the critical temperature at 40°C,

$$T_c > 40^\circ\text{C}, \quad (6.8)$$

which is over 13°C higher than that predicted by Kim and Cannell. Since the surface pressure data are in agreement, the discrepancies in the phase boundaries and the critical temperature must be attributed to the interpretation of the data.

---

<sup>4</sup>While Kim and Cannell carried out their experiment on an acidic subphase with pH = 2, Hawkins and Benedek used pure, distilled water as a subphase. Since PDA dissociates above a pH of 5, the PDA concentration in Hawkins and Benedek's experiment is not well controlled.

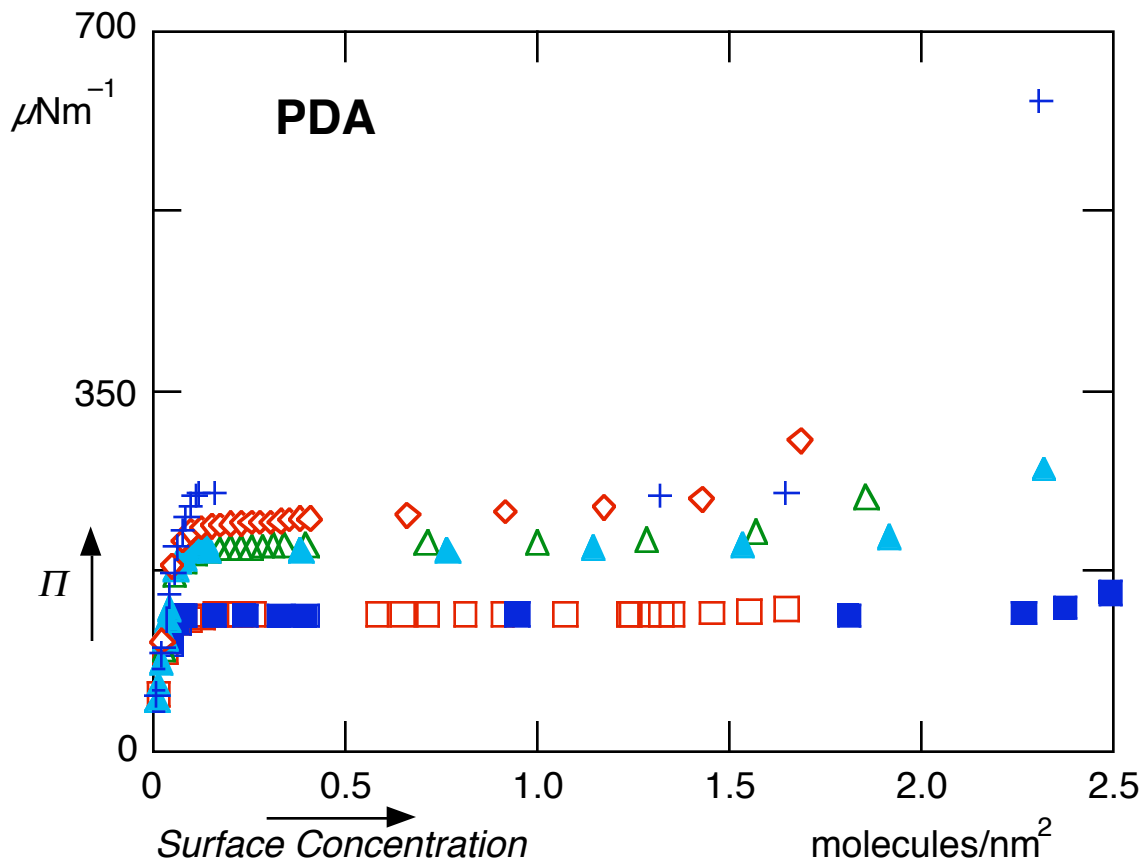


Fig. 6.4 Isotherms of pentadecanoic acid in the coexistence region of the gaseous and liquid-expanded phase. The open symbols represent data taken from the thesis of Kim [Kim, 1975], and the solid symbols and vertical crosses represent data taken from that of Pallas [Pallas, 1983]: solid squares – 20 °C; open squares – 20.03 °C; solid triangles – 30 °C; open triangles – 30.10 °C; open rhombuses – 34.69 °C; vertical crosses – 40 °C.

The above results demonstrate how difficult it is to obtain reliable phase boundary and critical point information from surface pressure measurements. A better understanding of the phase behavior of monolayer can be attained if one can directly view the various phases. Such viewing is possible with fluorescent microscopy<sup>5</sup> [Losche, Sackmann, *et al.*, 1983, Tschärner and McConnell, 1981]. By adding a fluorescent dye that has a high solubility in the liquid-expanded phase, one can distinguish the various phases. In the coexistence region, dark domains

<sup>5</sup>Fluorescent dyes that can be chemically bonded to specific substances and that have high solubility in only one monolayer phase provide optical contrast between different phases.

in the gaseous phase can be seen on a bright continuous background formed by the liquid-expanded phase, clearly showing the heterogeneity of the system. When the monolayer is compressed, the dark domains decrease in size and eventually disappear, giving way to a uniform bright homogeneous liquid-expanded phase. The disappearance of the dark domains marks the end of the coexistence region, and allows one to determine the phase boundary,  $\Gamma_{LE}$ . Moore *et al.* used this technique to study the gaseous to liquid-expanded phase transition of pentadecanoic acid over the temperature range 17-70 °C [Moore, Knobler, *et al.*, 1990]. Their results, also listed in Table 6.1, show that the coexistence of the gaseous and liquid-expanded phase persists all the way up to 70 °C. Their claim, therefore, is that the critical temperature lies above their range of temperature,

$$T_c > 70^\circ\text{C} . \tag{6.9}$$

The use of a dye in fluorescent microscopy adds a surface impurity to the system. This may affect the phase behavior of the monolayer and alter the phase boundary. Although this effect is claimed to be small [Moore, Knobler, *et al.*, 1990], the results obtained by this technique may not accurately reflect the behavior of a pure pentadecanoic acid monolayer. In the following chapter, we present data on the damping of capillary waves on a monolayer-covered liquid surface. Results obtained in the gaseous/liquid-expanded coexistence region provide information on the phase boundary and critical temperature of a pure pentadecanoic acid monolayer. Unlike surface pressure measurements where the changes is small in this low-density region, substantial changes in damping can be seen in this coexistence region. In addition, contrary to fluorescent microscopy, these damping measurement technique does not require the introduction of impurities onto the monolayer.

## References

- Adam, N., *Proc. R. Soc. (London) A*, **101**, 516 (1922).
- Adam, N.K., *The Physics and Chemistry of Surfaces* (Dover Publications, Inc., New York, 1968).
- Adam, N.K. and Harding, *Proc. R. Soc. A*, **138**, 419 (1932).
- Adam, N.K. and Jessop, G., *Proc. R. Soc. (London)*, **A110**, 423 (1926).
- Adamson, A.W., *Physical Chemistry at Surfaces* (Wiley Interscience, New York, 1976).
- Bibo, A.M., Knobler, C.M. and Peterson, I.R., *J. Ohys. Chem.*, **95**, 5591 (1991).
- Dervichian, D.G., *J. Chem. Phys.*, **7**, 931 (1939).
- Fisher, M.E., *J. Chem. Soc. Faraday Trans. II*, **82**, 1824 (1986).
- Franklin, B., *Roy. Soc. London, Phil. Trans.*, **64**, 44 5 (1774).
- G.L. Gaines, J., *Insoluble Monolayers at Liquid-Gas Interfaces* (Interscience Publishers, New York, 1966).
- Harkins, W.D., *The Physical Chemistry of Surface Films* (Reinhold Publishing Corporation, New York, 1952).
- Harkins, W.D. and Boyd, E., *J. Phys. Chem.*, **45**, 20 (1941).
- Hawkins, G.A. and Benedek, G.B., *Phys. Rev. Lett.*, **32**, 524 (1974).
- Jones, M.N., *Biological Interfaces* (Elsevier, New York, 1975).
- Kim, M.W., Ph.D. thesis: *Experimental Study of a Two-Dimensional Fluid Near Its Critical Point* (UC Santa Barbara, 1975).
- Kim, M.W. and Cannell, D., *Phys. Rev. A*, **13**, 411 (1976).

- Kim, M.W. and Cannell, D.S., *Phys. Rev. Lett.*, **35**, 889 (1975).
- Knobler, C.M., *Adv. Chem. Phys.*, **77**, 397 (1990).
- Langmuir, I., *J. Am. Chem. Soc.*, **39**, 1848 (1917).
- Langmuir, I., *J. Am Chem. Soc.*, **29**, 1848 (1917).
- Langmuir, I., *J. Chem. Phys.*, **1**, 756 (1933).
- Lin, B., Shih, M.C., Bohanon, T.M., Ice, G.E. and Dutta, P., *Phys. Rev. Lett.*, **65**, 191 (1990).
- Losche, M., Sackmann, E. and Mohwald, H., *Ber. Bunsenges. Phys. Chem.*, **87**, 848 (1983).
- Lundquist, M., *Chem. Scr.*, **1**, 5 (1971).
- Miyasaka, T., Watanabe, T. and Fujishima, A., *Am. Chem. Soc.*, **100**, 6657 (1978).
- Moore, B.G., Knobler, C.M., Akamatsu, S. and Rondelez, F., *J. Phys. Chem.*, **94**, 9588 (1990).
- Pallas, N.R., *Phase Transitions in Insoluble Monolayers at the Air/Water Interface*, Pages (Clarkson College of Technology, City, 1983).
- Pallas, N.R. and Pethica, B.A., *J. Chem Soc., Fara. Trans1*, **83**, 585 (1987).
- Pethica, B.A., Glasser, M.L. and Mingins, J., *J. Coll. Int. Sci.*, **81**, 41 (1981).
- Pockels, A., *Nature*, **43**, 437 (1891).
- Rayleigh, L., *Proc. Roy. Soc. London*, **47**, 364 (1890).
- Rayleigh, L., *Phil. Mag.*, **48**, 337 (1899).
- Schulman and Hughes, *Proc. R. Soc. A*, **138**, 430 (1932).
- Stallberg-Stenhagen, S. and Stenhagen, E., *Nature*, **156**, 239 (1945).
- Stanley, H.E., *Introduction to Phase Transitions and Critical Phenomena* (Oxford University Press, New York, 1971).

Takahashi, A. and Kawaguchi, M., *Adv. Polym. Sci.*, **46**, 1 (1982).

Ter-Minassian-Saraga, L. and Prigogine, I., *Mem. Serv. Chim. Etat (Paris)*, **38**, 109 (1953).

Tredgold, R.H. and Jones, R., *I.E.E. Proc.*, **128**, 202 (1981).

Tscharner, V.v. and McConnell, H.M., *Biophys. J.*, **36**, 409 (1981).

## Chapter 7

# Damping of Capillary Waves at Liquid Surfaces covered with Insoluble Monolayers

The damping of capillary waves on the surface of a pure liquid of low viscosity is presented in Chapter 5. Surfactants can have a drastic effect on this damping. These changes occur because of the viscous and elastic properties of the adsorbed monolayer, which resists the periodic expansion and compression of the surface. Below we present a theory for the damping of capillary waves on a liquid surface covered by a surfactant monolayer. Next, we show experimental data taken on a water-air interface covered by a monolayer of pentadecanoic acid and obtain from the data a phase boundary for the gas-liquid transition.

## 7.1 Background

The effect of surfactants on the wave motion of a liquid surface has been known since antiquity. The calming effect of oil on a rough sea was first noted by Pliny the Elder [Plinius] in the first century, and has since been common knowledge to seamen. In fact, most of the early observations on the effect of surface-active substances on ocean waves were made by sailors under trying conditions.

The first recorded experiment on the effect of oil on surface wave damping was carried out by Benjamin Franklin on the pond of Clapham Common in the late eighteenth century. In 1774, he described this famous experiment to his colleagues at the Royal Society in London [Franklin, 1774]:

*... the oil, though not more than a teaspoonful, produced an instant calm over a space several yards square, which spread amazingly, and extended itself gradually till it reached the lee side, making all that quarter of the pond, perhaps half an acre, as smooth as a looking glass. ...*

Franklin subsequently also carried out a number of experiments on the damping of surface wave by monolayers of oil. Since then, many experimental and theoretical studies have focused on the effect of surface-active substances on the damping of surface waves. It was not until 1883, however, that Aiken showed that the increase of surface wave damping by a surface film is due to the film's resistance to compression [Aiken, 1883].

It took over a hundred years after Franklin's experiments before it was realized that Franklin's oil film had a thickness on the order of molecular dimensions [Rayleigh, 1890]. Aiken was first to associate the increased damping

with the film's resistance to compression [Aiken, 1883]. Later work shows that the presence of a monomolecular film at a liquid-vapor interface changes the viscoelastic properties of the surface. This alters the boundary condition of the problem and leads to an increased damping of surface waves [Levich, 1941]. Theoretical studies have also shown that the calming of surface waves in the presence of a monolayer with finite dilational compressibility is due to the suppressed capillary wave generation, which, in turn, results in a reduced coupling between the liquid surface and the wind [Nelson, 1985].

In Section 5.2, we showed that for a pure interface, the boundary imposes the condition that the stresses from within the liquid balance out any stresses due to surface forces. As shown in Eqs. (5.28a) and (5.28b), the boundary condition thus requires that both the tangential and normal components of the viscous stress tensor be continuous. The normal components of the stress tensor is equal to the capillary pressure of the deformed surface as given by Laplace-Young's law (5.8), and is the same for both a pure interface and one with an adsorbed monolayer. A tangential component arises only when there is a surface tension gradient at the interface. For a pure interface the tangential component vanishes, since there can be no gradients in surface tension, see Eq. (5.28b). The picture is different for a monolayer-covered surface because the wave motion causes the monolayer to contract and expand and thus results in surface tension variations [Dorrestein, 1951, Goodrich, 1961, Hansen and Mann, 1964, Levich, 1941, Tempel and Riet, 1965].

The non-zero tangential components of the stress tensor depend on the extent and rate of surface deformation, and represent the resistance of the surface film to changes in both area and shape. The new surface viscoelastic properties introduced by the presence of a monolayer can therefore be

expressed by two moduli [Lucassen-Reynders and Lucassen, 1969]: 1) the surface dilational modulus, which is a measure of the surface film's resistance to changes in surface area, represented by a surface dilational elasticity,  $\varepsilon_d$ , and a surface dilational viscosity  $\eta_d$ ; 2) the surface shear modulus, which is the resistance to changes in the shape of the surface, represented by a surface shear elasticity,  $\varepsilon_s$ , and a surface shear viscosity  $\eta_s$ . In general, the effects of the surface shear modulus are assumed to be small compared those of the dilational modulus [Lucassen-Reynders and Lucassen, 1969]. If both the surface shear elasticity and viscosity are neglected, the only new viscoelastic coefficients are  $\varepsilon_d$  and  $\eta_d$ .

For the case where the surface dilational viscosity  $\eta_d$  is zero,<sup>1</sup> the surface dilational modulus is given by the surface dilational elasticity alone,

$$\varepsilon = \varepsilon_d(\omega). \quad (7.1)$$

In the static limit, the surface dilational elasticity is frequency independent, and is equivalent to the static elasticity,  $\varepsilon_d = \varepsilon_0$ . This static elasticity follows from the equilibrium relationship between surface tension  $\sigma$  and surface concentration of surfactant molecules,  $\Gamma_0$ , and is given by [Davies and Vose, 1965],

$$\varepsilon_0 = -\frac{\partial \sigma}{\partial \ln \Gamma_0}. \quad (7.2)$$

The surface dilational modulus is therefore directly related to measurable equilibrium surface properties in the purely elastic case.

These new viscoelastic properties alter the boundary conditions that constrain the wave motion. In the next section, we use these boundary

---

<sup>1</sup>The case of negligible surface dilational viscosity has been observed with a number of insoluble monolayers [Lucassen-Reynders, 1969 #10].

conditions to derive the velocity components of the surface wave and obtain a dispersion relation for waves on a surface covered with an insoluble monolayer.

## 7.2 Wave Motion at an Interface Covered with an Insoluble Monolayer

As for the case of a pure surface of an incompressible liquid, we start from the general solutions for the velocity components and pressure, which follow from the equation of continuity and the linearized Navier-Stokes equation,

$$v_x = \left( ikAe^{kz} - lCe^{lz} \right) e^{i(kx - \omega t)}, \quad (7.3)$$

$$v_z = \left( kAe^{kz} + ikCe^{lz} \right) e^{i(kx - \omega t)}, \quad (7.4)$$

$$p_o = i\rho\omega_o A e^{k_o z} e^{i(k_o x - \omega_o t)} - \rho g z, \quad (7.5)$$

see Chapter 5. The boundary conditions which constrain these solutions are, however, different from the pure case.

In the normal direction the boundary condition is still given by the Laplace-Young equation (see Eq. 5.28b). Neglecting, again, the pressure due to the vapor phase above the liquid, this condition becomes

$$p_{zz} = \sigma(\Gamma) \frac{\partial^2 \zeta}{\partial x^2}. \quad (7.6)$$

Note that the surface tension,  $\sigma(\Gamma)$ , is now a function of the surface concentration,  $\Gamma$ , and that  $\zeta$ , the vertical displacement of the liquid surface from its equilibrium position, is related to  $v_z$  by

$$\frac{\partial \zeta}{\partial t} = v_z. \quad (7.7)$$

Using  $v_z$  in Eq. (7.4), we can write  $\zeta$  in the form,

$$\zeta = \frac{kA + ikC}{-i\omega} e^{i(kx - \omega t)}. \quad (7.8)$$

A second boundary condition is given by the tangential component of the stress tensor, which is now no longer zero because of the additional viscoelastic properties introduced by the monolayer,

$$p_{zx} = \frac{\partial \sigma}{\partial \Gamma} \frac{\partial \Gamma}{\partial x}, \quad (7.9)$$

where  $\Gamma$  is a function of position on the surface.

Assuming the motion of the surface waves causes only small deviations of the surface concentration from its equilibrium value, the surface concentration can be written as

$$\Gamma = \Gamma_0 + \Gamma', \quad (7.10)$$

where  $\Gamma_0$  is the equilibrium surface concentration and  $\Gamma' \ll \Gamma_0$  the deviation from the equilibrium value. The surface concentration must obey conservation of mass [Levich, 1962]:

$$\frac{\partial \Gamma}{\partial t} + \frac{\partial}{\partial x} (\Gamma v_x) = D_s \frac{\partial^2 \Gamma}{\partial x^2}, \quad (7.11)$$

with  $D_s$  is the surface diffusion coefficient. Substituting Eqs. (7.3) and (7.10) into (7.11) and seeking a solution for the surface concentration deviation of the form,

$$\Gamma' = E e^{i(kx - \omega t)}, \quad (7.12)$$

the following expression is obtained for the constant  $E$ ,

$$E = \frac{-ik\Gamma_o(ikA - lC)}{-i\omega + k^2 D_s}, \quad (7.13)$$

where we have neglected all terms of second order contribution. For frequencies in the capillary wave regime, the term containing the diffusion coefficient in the denominator is small compared to the wave frequency, and the surface concentration reduces to

$$\Gamma = \Gamma_o + \frac{ik\Gamma_o(ikA - lC)}{i\omega} e^{i(kx - \omega t)}. \quad (7.14)$$

Substituting Eqs. (7.14) and (7.8) into (7.6), and approximating the value of  $\sigma(\Gamma) \approx \sigma(\Gamma_o)$ , the normal boundary condition in Eq. (7.11) now becomes

$$p_{zz} = \sigma(\Gamma_o) \frac{kA + ikC}{-i\omega} e^{i(kx - \omega t)}. \quad (7.15)$$

By a similar substitution of Eq. (7.14) into (7.12), the tangential boundary condition can be re-expressed as

$$p_{zx} = \frac{\varepsilon k^2}{i\omega} (ikA - lC) e^{i(kx - \omega t)}, \quad (7.16)$$

where the surface dilational modulus  $\varepsilon$  is defined as

$$\varepsilon \equiv -\frac{\partial \sigma}{\partial \Gamma} \Gamma_o. \quad (7.17)$$

Equating Eqs. (7.15) and (7.16) to the definitions of the normal and tangential boundary conditions given by

$$p_{zz} \equiv -p + 2\eta \frac{\partial v_z}{\partial z}, \quad (7.18)$$

$$p_{zx} \equiv \eta \left( \frac{\partial v_x}{\partial v_z} + \frac{\partial v_z}{\partial v_x} \right), \quad (7.19)$$

and substituting into them Eqs. (7.3) and (7.4), we obtain the following two equations relating the unknown quantities  $A$  and  $C$  :

$$\left(-\omega^2 - i\omega 2vk^2 + gk + \frac{\sigma}{\rho}k^3\right)A + i\left(gk + \frac{\sigma}{\rho}k^3 - i\omega 2vkl\right)C = 0, \quad (7.19)$$

$$i\left(-i\omega 2vk^2 + \frac{\varepsilon}{\rho}k^3\right)A - \left(-i\omega 2vk^2 - \omega^2 + \frac{\varepsilon}{\rho}k^2l\right)C = 0. \quad (7.20)$$

In the capillary wave regime, the terms due to gravity  $gk$  are negligible. Neglecting these terms and setting the determinant of the equations to zero, we obtain the following dispersion relation between the angular frequency and wavevector for a monolayer-covered surface:

$$\begin{aligned} & \left(\frac{\sigma}{\rho}k^3 - i\omega 2vkl\right)\left(-i\omega 2vk^2 + \frac{\varepsilon}{\rho}k^3\right) \\ & - \left(-i\omega 2vk^2 - \omega^2 + \frac{\varepsilon}{\rho}k^2l\right)\left(-\omega^2 - i\omega 2vk^2 + \frac{\sigma}{\rho}k^3\right) = 0 \end{aligned} \quad (7.21)$$

Setting  $\varepsilon$  to zero in the above equation, we recover the Lamb-Levich dispersion relation for a pure liquid,

$$(2vk^2 - i\omega)^2 + \omega_0^2 = 4v^2k^4 \sqrt{1 - \frac{i\omega}{vk^2}}. \quad (7.22)$$

In the general case, however, the dispersion relation is now a sixth-order polynomial in  $k$ ,

$$-\frac{\varepsilon\sigma}{\rho^2}k^6 + \omega^4 + i4vk^2\omega - \frac{\varepsilon}{\rho}k^2l\omega^2 - \frac{\sigma}{\rho}k^3\omega^2 + \frac{\varepsilon\sigma}{\rho^2}k^5l = 0. \quad (7.23)$$

The above dispersion relation for a surface covered with a monolayer is considerably more complicated than the Lamb-Levich equation, and cannot generally be solved analytically.

### 7.3 Damping

As for a pure surface, the angular frequency  $\omega$  and wavevector  $k$  in the dispersion equation (7.23) are complex quantities, with the imaginary parts representing damping of the wave motion. In evaluating damping in the monolayer-covered system, we will, as in the case of the pure liquid, be concerned only with liquids of low viscosity, where the following inequality

$$\frac{\omega}{2\nu k^2} \gg 1, \quad (7.24)$$

is satisfied.

Let us first evaluate the spatial damping coefficient of surface waves produced by a source of fixed amplitude. In this case, the amplitude of the wave at a given distance from the source does not decay with time; the falloff of the wave amplitude at different positions gives the spatial damping coefficient. For a surface wave of angular frequency  $\omega_0$  generated at some point on the surface, the associated wavevector  $k$  is complex. In the low-viscosity limit,  $k$  differs only slightly from the real value  $k_0$  of the pure case, given by Eq. (5.10), and can be written as

$$k = k_0 + k', \quad (7.25)$$

where  $k' = k'' + i\alpha$  represents the change in wavevector from the pure case. The real part of  $k'$  represents changes in the wavelength of the surface wave in the presence of a monolayer; the imaginary part  $\alpha \ll k_0$  is the spatial damping coefficient.

The spatial damping coefficient  $\alpha$  can be obtained by substituting Eq. (7.25) into the dispersion relation (7.23) and setting  $\omega = \omega_0$ . In the low-viscosity limit given by Eq. (7.24) the factor  $l$ , which is defined in Eq. (5.26) and which appears in the dispersion relation, reduces to

$$l \approx k_0 \sqrt{\frac{-i\omega_0}{\nu k_0^2}}. \quad (7.26)$$

Retaining only first order terms in  $\alpha$ , the dispersion relation yields a general solution for  $k'$ . The imaginary part  $\alpha$  of this solution, which accounts for the spatial damping of the waves is given by

$$\alpha = \frac{2k_0}{3\omega_0} \frac{\frac{\omega_0}{2\sqrt{2}} \left(\frac{\varepsilon}{\sigma}\right)^2 \sqrt{\frac{\omega_0}{\nu k_0}} - \frac{\varepsilon}{\sigma} \sqrt{2\nu k_0 \omega_0} + 2\nu k_0^2}{1 - \sqrt{2} \frac{\varepsilon}{\sigma} \sqrt{\frac{\omega_0}{\nu k_0^2}} + \left(\frac{\varepsilon}{\sigma}\right)^2 \frac{\omega_0}{\nu k_0^2}}, \quad (7.27)$$

while the real part  $k''$  has the form,

$$k'' = \frac{k_0}{3} \frac{\varepsilon}{\sigma} \frac{1 - \frac{\varepsilon}{\sigma} \sqrt{\frac{\omega_0}{2\nu k_0^2}} - \frac{2}{\omega_0} \sqrt{2\nu k_0^2 \omega_0}}{1 - \sqrt{2} \frac{\varepsilon}{\sigma} \sqrt{\frac{\omega_0}{\nu k_0^2}} + \left(\frac{\varepsilon}{\sigma}\right)^2 \frac{\omega_0}{\nu k_0^2}}. \quad (7.28)$$

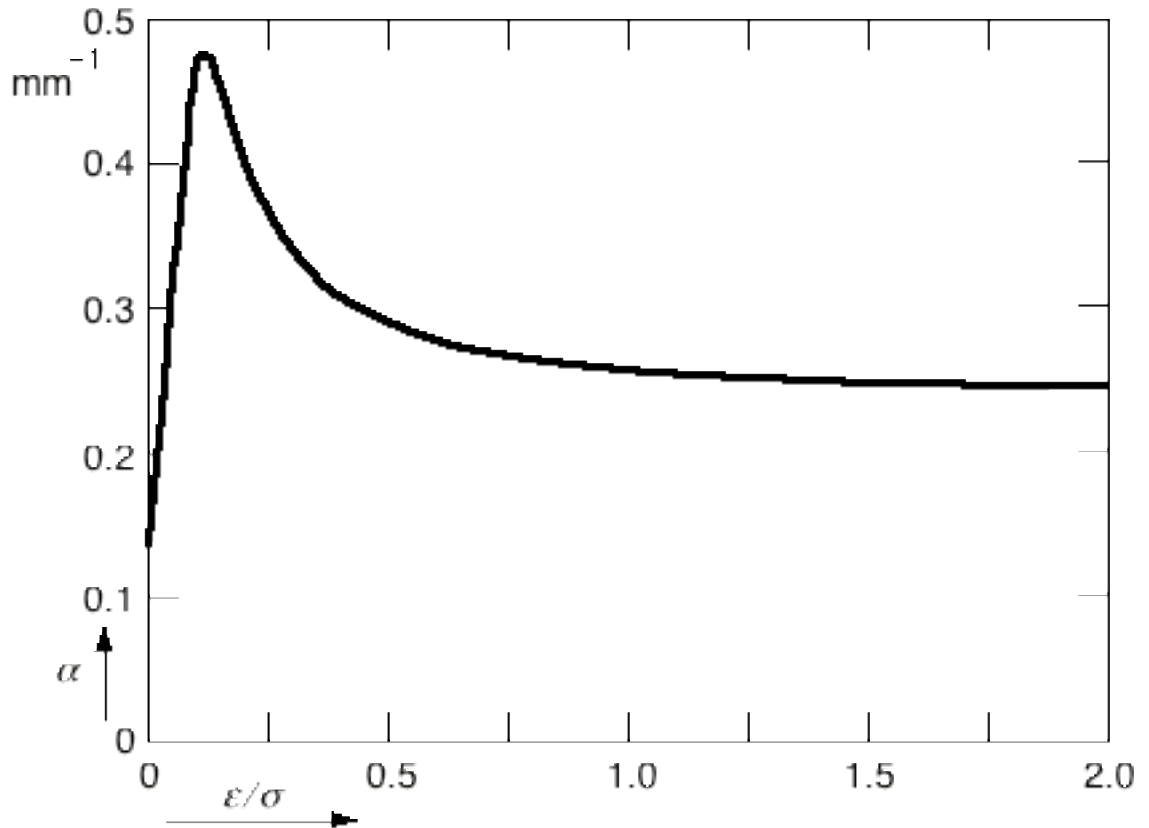


**Fig. 7.1** Calculated spatial damping coefficient as a function of the ratio between surface elasticity and surface tension using Eq. (7.27).

Equation (7.27) relates the spatial damping coefficient and the surface dilational modulus,  $\epsilon$ . In the limiting case of zero elasticity, the coefficient reduces to Stokes' value for a pure liquid, Eq. (5.37)

$$\alpha_0 = \frac{4\eta\omega_0}{3\sigma}. \quad (7.29)$$

Another limiting case is obtained for a totally inelastic surface, when  $\epsilon \rightarrow \infty$ . The damping coefficient then correctly reduces to the damping coefficient obtained by Reynolds [Reynolds, 1880],

$$\alpha_\infty = \frac{2k_0}{3\omega_0} \frac{\sqrt{vk_0^2\omega_0}}{2\sqrt{2}}. \quad (7.30)$$

The ratio of the coefficients in the two extreme limits is,

$$\frac{\alpha_{\infty}}{\alpha_0} = \frac{1}{4\sqrt{2}} \sqrt{\frac{\omega_0}{\nu k_0^2}}. \quad (7.31)$$

From the functional form of the spatial damping coefficient in Eq. (7.27) we see that the coefficient does not rise monotonically from its zero-elasticity value,  $\alpha_0$ , to its inelastic value,  $\alpha_{\infty}$ . Figure 7.1 shows the behavior of the spatial damping coefficient as a function of the ratio  $\varepsilon/\sigma$ . As can be seen the spatial damping goes through a maximum at a rather low value of the surface dilational modulus. The exact location of the maximum can be calculated by setting the partial derivative of  $\alpha$  with respect to  $\varepsilon$  to zero. The maximal value is thus found to be

$$\alpha_{max} = \frac{1}{3} k_0^2 \sqrt{\frac{2\nu}{\omega}}. \quad (7.32)$$

This maximum is achieved when the dilational modulus assumes the value,

$$\varepsilon_{max} = \frac{\sqrt{2\nu\rho^2\omega_0^3}}{k_0^2}. \quad (7.33)$$

Notice that the maximum spatial damping coefficient is twice as large as that for an inelastic surface, Eq.(7.30).

Now we turn to the temporal decay of thermally excited capillary waves. Consider a thermally excited wave with a fixed, real wavevector  $k_0$ . The associated angular frequency is now complex and its imaginary part represents the temporal damping of the waves. In the low-viscosity regime, the angular frequency in the presence of a monolayer can be written as

$$\omega = \omega_0 + \omega', \quad (7.34)$$

where  $\omega' = \omega'' - i\beta$  represents the change in frequency from the frequency  $\omega_0$  of a surface wave of wavevector  $k_0$  in the absence of a monolayer. The imaginary part  $\beta \ll \omega_0$  is the temporal damping coefficient. The coefficient,  $\beta$ , is obtained by substituting the wavevector,  $k_0$ , and the angular frequency,  $\omega$ , in Eq. (7.34) into the dispersion relation given by Eq. (7.23). Using Eq. (7.26), neglecting small terms in accordance with inequality (7.24), and retaining only first order terms in  $\beta$ , the dispersion relation yields a general solution for  $\omega'$ . The imaginary part of this solution, which accounts for the temporal damping of the waves is given by

$$\beta = \frac{\frac{\omega_0}{2\sqrt{2}} \left(\frac{\varepsilon}{\sigma}\right)^2 \sqrt{\frac{\omega_0}{\nu k_0^2}} - \frac{\varepsilon}{\sigma} \sqrt{2\nu k_0^2 \omega_0} + 2\nu k_0^2}{1 - \sqrt{2} \frac{\varepsilon}{\sigma} \sqrt{\frac{\omega_0}{\nu k_0^2}} + \left(\frac{\varepsilon}{\sigma}\right)^2 \frac{\omega_0}{\nu k_0^2}}, \quad (7.35)$$

while the real part has the form

$$\omega'' = \frac{\omega_0}{2} \frac{\varepsilon}{\sigma} \frac{1 - \frac{\varepsilon}{\sigma} \sqrt{\frac{\omega_0}{2\nu k_0^2}} - \frac{2}{\omega_0} \sqrt{2\nu k_0^2 \omega_0}}{1 - \sqrt{2} \frac{\varepsilon}{\sigma} \sqrt{\frac{\omega_0}{\nu k_0^2}} + \left(\frac{\varepsilon}{\sigma}\right)^2 \frac{\omega_0}{\nu k_0^2}}. \quad (7.36)$$

The temporal damping coefficient for a pure liquid surface,

$$\beta_0 = 2\nu k^2, \quad (7.37)$$

is recovered from Eq. (7.35) by setting the dilational modulus  $\varepsilon$  to zero.

Notice that the spatial damping coefficient  $\alpha$  in Eq. (7.27) and the temporal damping coefficient  $\beta$  in (7.35) are related by,

$$\alpha = \frac{\beta}{\left(\frac{3\omega_0}{2k_0}\right)}. \quad (7.38)$$

The denominator in the above relation is the group velocity derived from the Kelvin equation. Notice that Eq. (7.38) is formally identical to (5.42) which relates the two damping coefficients in the case of a pure liquid surface. That this simple relation between the coefficients is true even for a monolayer-covered surface, and that the proportionality constant is the group velocity derived from the Kelvin equation may seem surprising. However, if one examines the wavevector (or frequency) corrections introduced by  $k''$  (or  $\omega''$ ), one finds that the changes are small<sup>2</sup>; therefore, to first order, the Kelvin equation is still an excellent approximation.<sup>3</sup>

## 7.4 Experimental Results

In Section 5.4, we presented data on the spatial damping coefficient for capillary waves on a pure liquid-vapor interface obtained using the differential Fourier transform heterodyne technique (see Section 4.2.2); the results are in excellent agreement with predictions given by hydrodynamic theory. We used the same experimental apparatus and optical setup to study spatial damping of capillary waves at a liquid-vapor interface in the presence of an adsorbed monolayer. As before, the measurements were carried out in a sealed chamber and capillary waves of a known frequency are induced using electrocapillarity. The resulting spectra are similar to the one shown in Fig. 4.7.

---

<sup>2</sup>For a capillary wave of frequency  $f = 1200$  Hz propagating on a water surface, the wavelength correction according to Eq. (7.28) is less than 3%.

<sup>3</sup>Substituting, for a completely inelastic surface,  $\varepsilon \rightarrow \infty$  into the dispersion relation (7.23) and retaining only terms containing  $\varepsilon$ , one recovers the Kelvin equation (with the gravity term omitted).

The surfactant used in this experiment is pentadecanoic acid (PDA), which is a fatty acid with a polar –OH headgroup and a 15-carbon hydrophobic tail, represented by the chemical formula,



This weak acid dissociates in water by undergoing the following reaction,



The dissociation constant of PDA,  $\text{p}K_a$ , is given by<sup>4</sup>

$$\text{p}K_a = -\log \frac{[\text{CH}_3(\text{CH}_2)_{13}\text{COO}^-][\text{H}^+]}{[\text{CH}_3(\text{CH}_2)_{13}\text{COOH}]}, \quad (7.41)$$

and is related to the  $\text{pH}$ <sup>5</sup> of the subphase by the following equation,

$$\text{p}K_a - \text{pH} = -\log \frac{[\text{CH}_3(\text{CH}_2)_{13}\text{COO}^-]}{[\text{CH}_3(\text{CH}_2)_{13}\text{COOH}]}. \quad (7.42)$$

Since the dissociation constant for PDA is 5.6 [Dippy, 1939], one finds, that 96% of the surfactant molecules dissociate when PDA is spread on a neutral water subphase ( $\text{pH} = 7$ )<sup>6</sup>. An acidic subphase is therefore necessary to minimize the dissociation of surfactant molecules. From Eq. (7.42) one finds that only 0.03% of the molecules dissociate when the acid is spread on a subphase with a  $\text{pH}$  of 2<sup>7</sup>,

---

<sup>4</sup>Square brackets in the equation denote the concentration of the bracketed compound.

<sup>5</sup> $\text{pH}$  is related to the concentration of  $\text{H}^+$  ions by the relation [Atkins, 1982]

$$\text{pH} = -\log[\text{H}^+].$$

<sup>6</sup>Using Eqn. (7.42), one finds that for  $\text{pH} = 7$ ,

$$\frac{[\text{CH}_3(\text{CH}_2)_{13}\text{COO}^-]}{[\text{CH}_3(\text{CH}_2)_{13}\text{COOH}]} = 10^{1.4} = 25.12.$$

<sup>7</sup>For  $\text{pH} = 2$ ,

and the percentage further reduces by an order of magnitude when the pH of the subphase is 1. The acidic aqueous subphase used in the experiment, described in Section 4.1.4, is a solution made by adding concentrated hydrochloric acid<sup>8</sup> to the ultrapure water sample<sup>9</sup>. A subphase of pH 2 is used for low temperature (< 30 °C) measurements, and a pH-1 subphase for high temperatures (>30 °C).

A solution of PDA<sup>10</sup> of known concentration is made with ultrahigh purity chloroform<sup>11</sup>. The monolayer is spread by carefully applying a small amount of the chloroform solution onto the surface of the aqueous subphase using a microliter syringe<sup>12</sup>. Access of the syringe to the sealed chamber is provided by one of the inlet ports on the front panel (see Section 4.1.5), and a 9-inch needle<sup>13</sup> is connected to the syringe to allow the point of application to be directly above the trough. The chloroform is allowed to evaporate for at least 20 minutes before the chamber is flushed several times with ultrahigh purity nitrogen<sup>14</sup>. Measurements are made only after the system is left undisturbed for at least two hours to assure complete mechanical and thermal equilibrium of the monolayer.

---

$$\frac{[\text{CH}_3(\text{CH}_2)_{13}\text{COO}^-]}{[\text{CH}_3(\text{CH}_2)_{13}\text{COOH}]} = 10^{-3.6} = 0.0002 .$$

<sup>8</sup>Ultrex II Reagent, Baker Analyzed

<sup>9</sup>Throughout 18-M $\Omega$ , deionized and distilled water from a Milli-Q UV+ system, by Millipore Corporation, is used.

<sup>10</sup>Pentadecanoic acid 99+%, F.W. = 242.40, Aldrich Chemical Company

<sup>11</sup>Reagent, Baker Analyzed

<sup>12</sup>100- $\mu$ l Gastight® high-performance syringe with Teflon Luer lock, Hamilton Company

<sup>13</sup>9-inch sharp-point 22s-gauge needle for 100- $\mu$ l syringe volume, Hamilton Company

<sup>14</sup>99.999% purity with < 0.5 ppm total hydrocarbon content, Igo's

We studied the effect of monolayers on capillary wave damping as a function of surface concentration over a range of temperatures. The surface concentration is varied by either reducing the surface area, or by successively spreading a known amount of chloroform solution of PDA onto the subphase surface. The surface tension of the system is monitored by the surface balance described in Section 4.1.3. All measurements were carried out at a frequency of 1.2 kHz. The temperature ranges from 14.9 °C, which lies below the triple point for PDA [Harkins, 1952, Moore, Knobler, *et al.*, 1990, Pallas and Pethica, 1987],

$$T_{TP} \approx 17^\circ\text{C}, \quad (7.43)$$

to 40.2 °C. Because of convection, increased humidity inside the chamber<sup>15</sup>, and increased solubility of surfactant molecules into the aqueous subphase, it is difficult to carry out measurements above 40 °C. The experimental results are plotted in Figs. 7.2 – 7.5, which show surface pressure and spatial damping as a function of surface concentration at the various temperatures.

The data in Fig. 7.2 were measured at 20.1 °C, a temperature above the triple point of PDA. As discussed in Section 6.3, we expect two plateau regions in the  $\Pi$ - $\Gamma$  isotherm at this temperature, one corresponding to the G-LE coexistence region, and the other to the LE-LC coexistence region. These plateaus can indeed be seen in the surface pressure data of Fig. 7.2 (a). The G-LE coexistence plateau

---

<sup>15</sup>The increased humidity leads to condensation on the windows and on the motors and encoders.

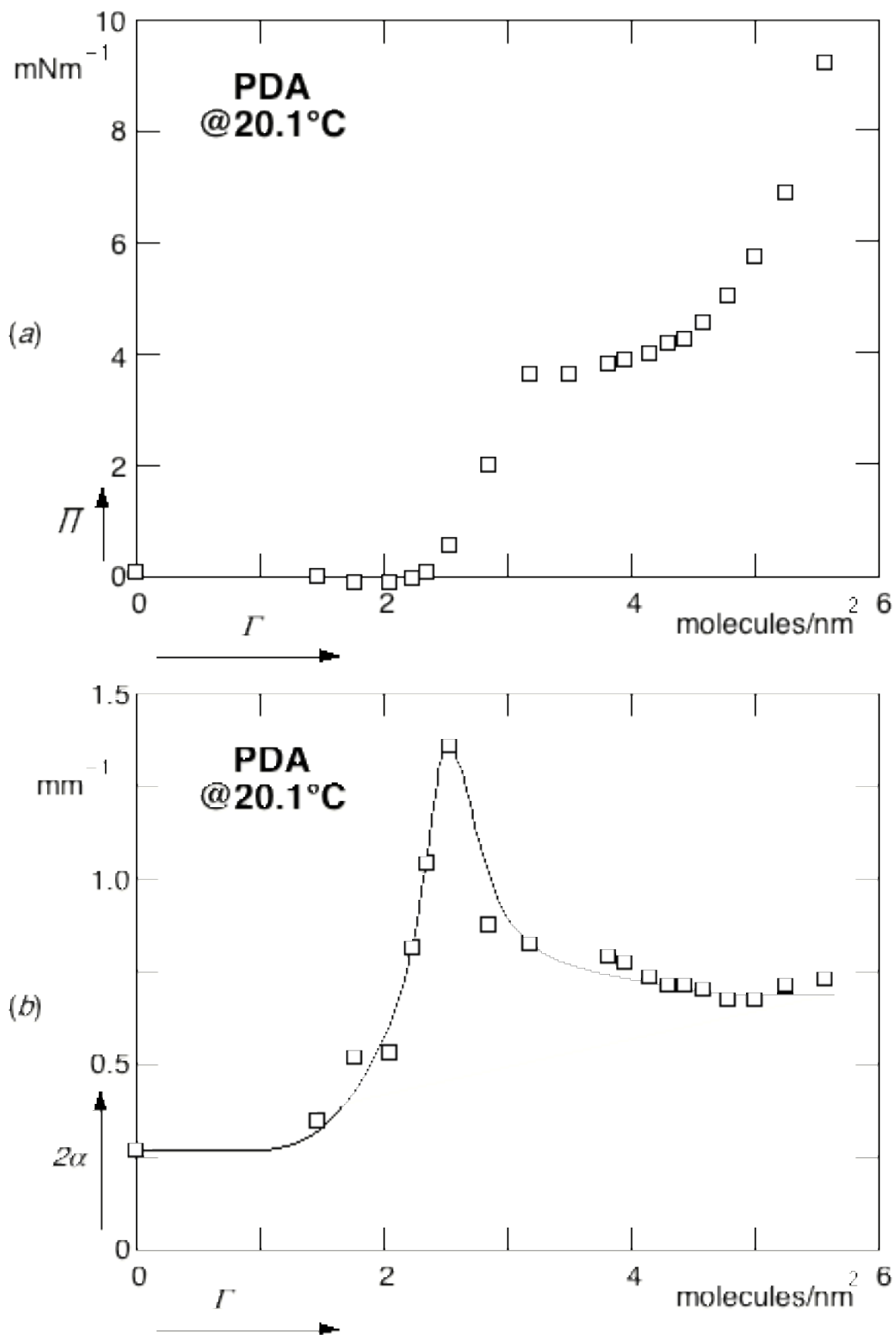


**Fig. 7.2** (a) Surface pressure  $\Pi$  and (b) damping coefficient  $\alpha$  as a function of surface concentration  $\Gamma$  for pentadecanoic acid adsorbed at a water-air interface at 20.1 °C. Capillary waves of frequency 1200 Hz were induced at the interface for the damping measurements.

occurs at low surface concentrations, and the measured surface pressure is essentially zero. The end of the G-LE transition occurs at a surface concentration,  $\Gamma_{LE}$ , of about 2.4 molecules/nm<sup>2</sup><sup>16</sup>. The LE-LC coexistence plateau is found at higher surface concentrations, spanning the range from 3.2 to 3.9 molecules/nm<sup>2</sup>.

The corresponding spatial damping coefficients are shown in Fig. 7.2 (b). Each point in this figure is determined by measuring the exponential decay of the induced capillary waves from a plot of wave amplitude ratio *vs.* distance, as in Fig. 5.3. Each value of this wave amplitude ratio is, in turn, obtained from a spectrum analogous to that in Fig. 5.2. Up to a surface concentration of 1.4 molecules/nm<sup>2</sup> the spatial damping coefficient is nearly constant and, within experimental error, identical to the one for pure water. Beyond 1.4 molecules/nm<sup>2</sup>, the spatial damping coefficient shows a sharp increase and a maximum is reached at a surface concentration of  $\Gamma_{max} = 2.5$  molecules/nm<sup>2</sup>. As the surface concentration is further increased, the damping coefficient decreases and levels out.

At 1.4 molecules/nm<sup>2</sup>, when the rise in the damping sets in, the monolayer is in the G-LE coexistence region. Recall that this region is

---

<sup>16</sup>We have not investigated at what surface concentration the transition from the gaseous phase to the LE phase begins, but other workers find that this takes place at a surface concentration of < 0.16 molecules/nm<sup>2</sup> [Pallas, 1987 #14; Kim, 1976 #19].

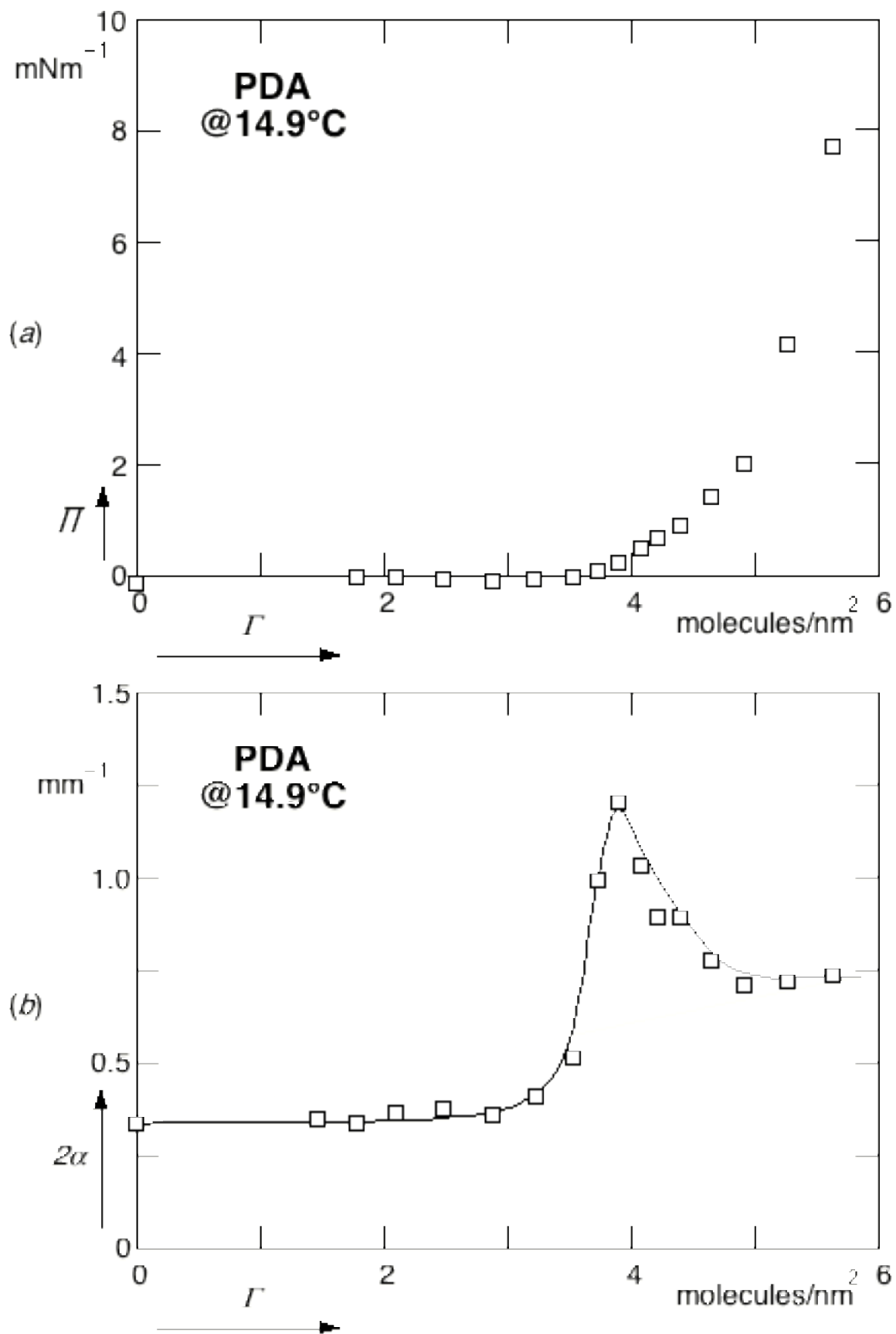


**Fig. 7.3** (a) Surface pressure  $\Pi$  and (b) damping coefficient  $\alpha$  as a function of surface concentration  $\Gamma$  for pentadecanoic acid adsorbed at a water-air interface at 14.9 °C. Capillary waves of frequency 1200 Hz were induced at the interface for the damping measurements.

characterized by islands of surfactant molecules in the gaseous phase surrounded by surfactant molecules in the LE phase (see Section 6.3). The data in Fig. 7.2 (b) indicate that the damping is unaffected when the fraction of molecules in the gaseous phase is high. The maximum in the damping occurs near the end of the G-LE coexistence region at a surface concentration of  $\Gamma_{LE}$ .

Figure 7.3 shows data obtained at 14.9 °C, which lies below the triple point of PDA. Isotherms below the triple point have only one plateau; the LE phase is no longer observed as the film sublimates from the gas phase to the more condensed LC phase. The  $\Pi$ - $\Gamma$  isotherm in Fig. 7.3 (a) indeed shows only a single plateau and the surface pressure remains zero up to much higher surface concentration than above the triple point. The surface pressure starts to rise at  $\Gamma_{LC} = 3.9$  molecules/nm<sup>2</sup>, indicating the end of the transition and the emergence of a pure LC phase.

Unlike the measurements at 20.1 °C, where the rise in the damping sets in at  $\Gamma = 1.4$  molecules/nm<sup>2</sup>, below the triple point a rise is not observed until a much higher surface concentration of 3.0 molecules/nm<sup>2</sup> is reached, see Fig. 7.3 (b).<sup>17</sup> The maximum now occurs at a surface concentration  $\Gamma_{max} = 3.9$  molecules/nm<sup>2</sup>. As before, when the surface concentration is further increased, the damping coefficient decreases and levels out.

It is believed that the surface morphology in the G-LC coexistence region is similar to that in the G-LE region, where islands of surfactant molecules in the gaseous phase float in a sea of molecules in the condensed LC phase [Moore, Knobler, *et al.*, 1990]. The spatial damping results of Fig. 7.3 (b) show that the damping coefficient remains close to that of a pure water interface at low surface

---

<sup>17</sup>At this concentration the monolayer is well within the G-LC coexistence region.

concentrations. In this case the maximum coincides with the end of the G-LC transition at  $\Gamma_{LC}$ .

Figures 7.4 (a) and 7.4 (b) show the results obtained at 30.3 °C. The G-LE and LE-LC coexistence regions are now smaller. The first plateau extends to a surface concentration,  $\Gamma_{LE} = 1.9$  molecules/nm<sup>2</sup>, while the second plateau spans the range 2.4–2.7 molecules/nm<sup>2</sup>. The rise in damping sets in at 1.1 molecules/nm<sup>2</sup> and achieves a maximum at  $\Gamma_{max} = 1.9$  molecules/nm<sup>2</sup>, at the point where the surface pressure begins to increase. As before the coefficient decreases and then levels out as the surface concentration is increased further.

The results obtained at 40.2 °C are shown in Figs. 7.5 (a) and 7.5 (b). At this high temperature the solubility of PDA increases and not all PDA molecules remain at the interface; the actual surface concentration is therefore probably lower than the one shown in the figures, which is calculated assuming no solubility. The isotherm in Fig. 7.5 (a) shows much more scatter than those obtained at lower temperatures, but the damping data, shown in Fig. 7.5 (b), remains very clean. Ignoring the solubility of the PDA, the rise in surface pressure occurs at  $\Gamma = 2.6$  molecules/nm<sup>2</sup>; the one in the spatial damping at  $\Gamma = 2.3$  molecules/nm<sup>2</sup>; the maximum in the damping occurs at  $\Gamma_{max} = 2.6$  molecules/nm<sup>2</sup>. Although the location of the maximum cannot be determined exactly, once again we note that the maximum occurs near the point where the surface pressure starts to increase.

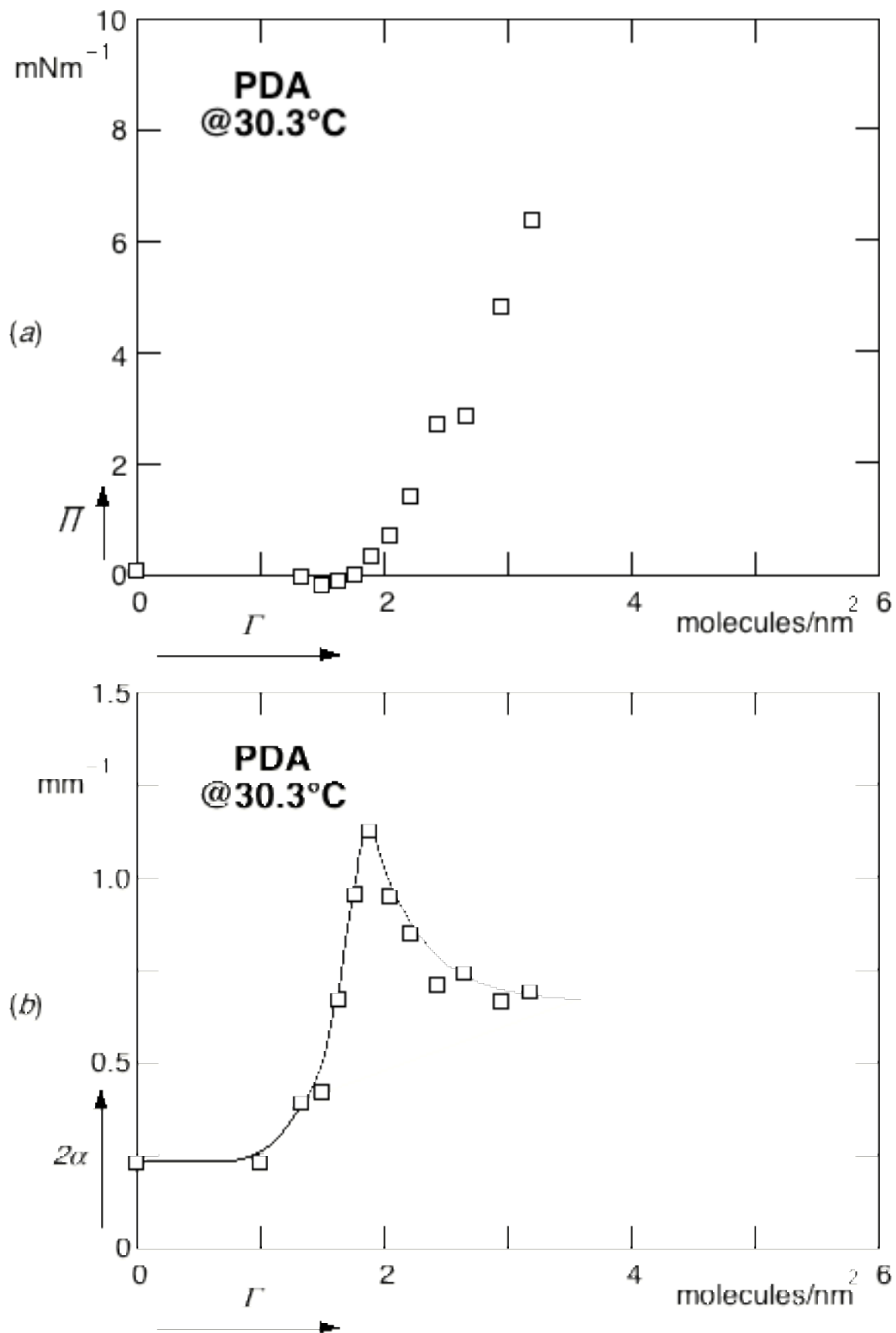


**Fig. 7.4** (a) Surface pressure  $\Pi$  and (b) damping coefficient  $\alpha$  as a function of surface concentration  $\Gamma$  for pentadecanoic acid adsorbed at a water-air interface at 30.3 °C. Capillary waves of frequency 1200 Hz were induced at the interface for the damping measurements.

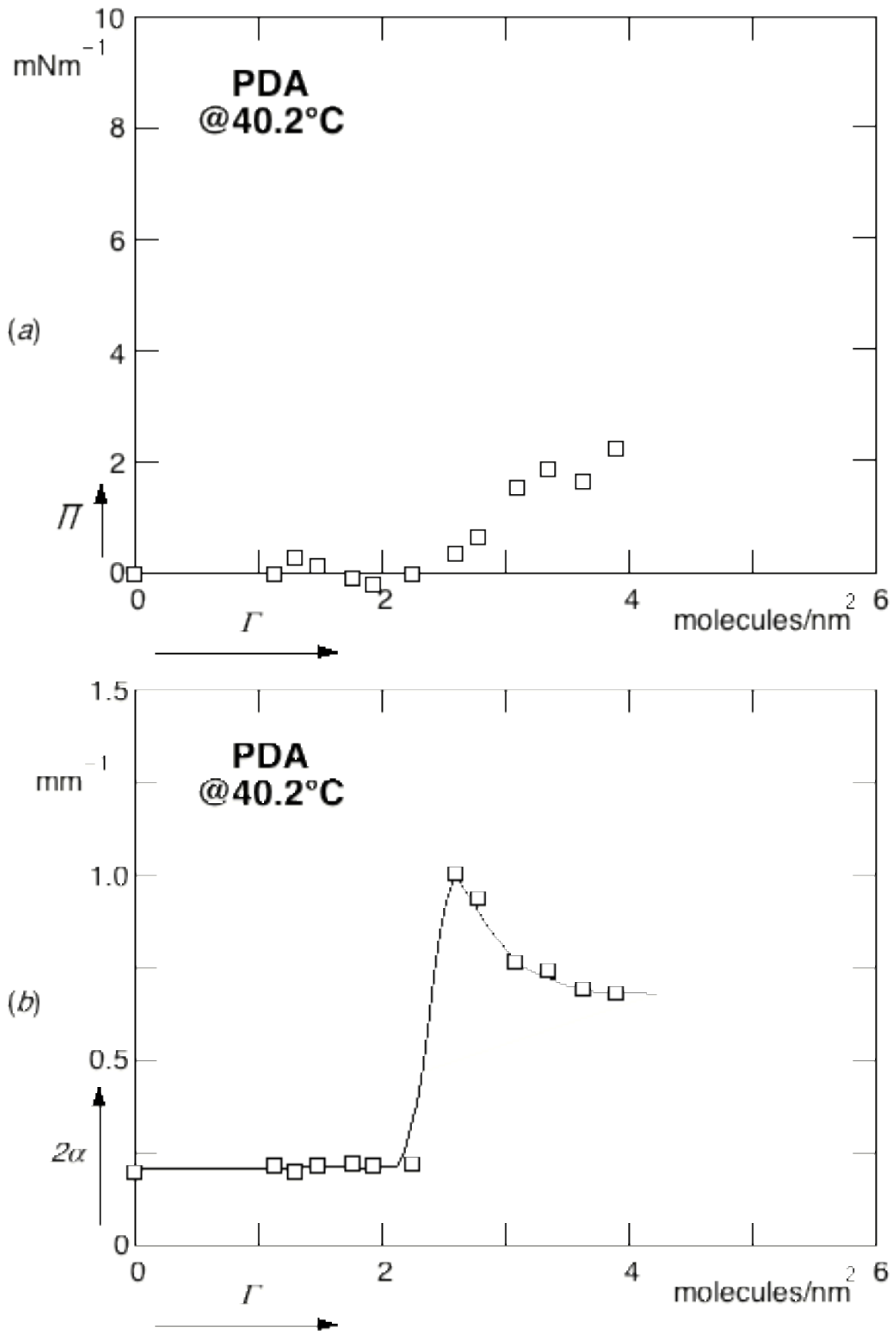


**Fig. 7.5** (a) Surface pressure  $\Pi$  and (b) damping coefficient  $\alpha$  as a function of surface concentration  $\Gamma$  for pentadecanoic acid adsorbed at a water-air interface at 40.2 °C. Capillary waves of frequency 1200 Hz were induced at the interface for the damping measurements.

## 7.5 Discussion

The experimental results presented above indicate that at every temperature studied, a maximum in the damping occurs at the surface concentration where the surface pressure begins to rise. We will now examine if the observed maximum can be adequately explained by the theory outlined in Section 7.3.

We recall first that the experimentally determined spatial damping coefficients  $\alpha_o$  of a pure water-air interface (see Figs. 5.4 and 5.5) agree well with the theoretical predictions. Using Eqs. (7.33), (7.34), (7.36), and (7.37), one can calculate the spatial damping coefficient  $\alpha_o$  for a pure surface, the value for a completely inelastic surface,  $\alpha_\infty$ , the maximum value of the damping,  $\alpha_{max}$ , and the surface dilational modulus at which the maximum is reached,  $\varepsilon_{max}$ . The calculated values are tabulated along with the experimental values in Table 7.1. These tabulated values reaffirm the good agreement between

| $T$ ( $^{\circ}\text{C}$ ) | $\alpha_o$ |      | $\alpha_\infty$ |      | $\alpha_{max}$ |      | $\varepsilon_{max}$ |      |
|----------------------------|------------|------|-----------------|------|----------------|------|---------------------|------|
|                            | theory     | exp  | theory          | exp  | theory         | exp  | theory              | exp  |
| 14.9                       | 1.56       | 1.67 | 2.44            | 3.59 | 4.89           | 6.01 | 11.74               | 3.43 |
| 20.1                       | 1.38       | 1.36 | 2.30            | 3.45 | 4.60           | 6.78 | 10.91               | 8.53 |
| 30.3                       | 1.12       | 1.09 | 2.08            | 3.37 | 4.16           | 5.63 | 9.58                | 4.75 |
| 40.2                       | 0.94       | 0.98 | 1.91            | 3.42 | 3.82           | 5.02 | 8.55                | 4.36 |

**Table 7.1** Theoretical and experimental values for spatial damping at three limiting cases:  $\alpha_o$  for a pure interface;  $\alpha_\infty$  for completely inelastic surface film;  $\alpha_{max}$  for the maximal damping value occurring at  $\varepsilon_{max}$ .

theory and experiments in the case of a pure interface. In the other two limits, however, consistently higher experimental damping values are found. These higher values suggest that there might be other dissipative processes present. In the theory outlined in Sections 7.2 and 7.3, effects due to surface dilational viscosity and the surface shear modulus have been ignored. These dissipative quantities may partly account for the additional capillary wave observed.

The above comparison is restricted to only three limiting cases. The spatial damping at other surface concentrations can be obtained using Eq. (7.27), but this requires the knowledge of the surface dilational modulus  $\varepsilon$  as a function of surface concentration. In the following analysis, we use, for the surface dilational modulus, static elasticity values obtained from the isotherm measurements using the relation,

$$\varepsilon_o = \frac{\partial \Pi}{\partial \Gamma_o} \Gamma_o, \quad (7.44)$$

which is equivalent to Eq. (7.2) because the surface tension and surface pressure differ from one another by a constant. Figures 7.6 (a) and 7.7 (a) show the static elasticity obtained using Eq. (7.44) from a polynomial fit to surface pressure measurements made at 14.9 °C and 20.1 °C respectively. As mentioned before, 14.9 °C is below the triple point temperature for PDA, and there is only one plateau in the isotherm, see Eq. (7.43). This translates into a flat region with zero elasticity for surface concentrations up to approximately 3.5 molecules/nm<sup>2</sup>. Beyond this value, the elasticity rises steadily, see Fig. 7.6(a). Above the triple point temperature, at 20.1 °C, there are two plateaus in the isotherm resulting in two zero elasticity regions, see Fig. 7.7 (a).

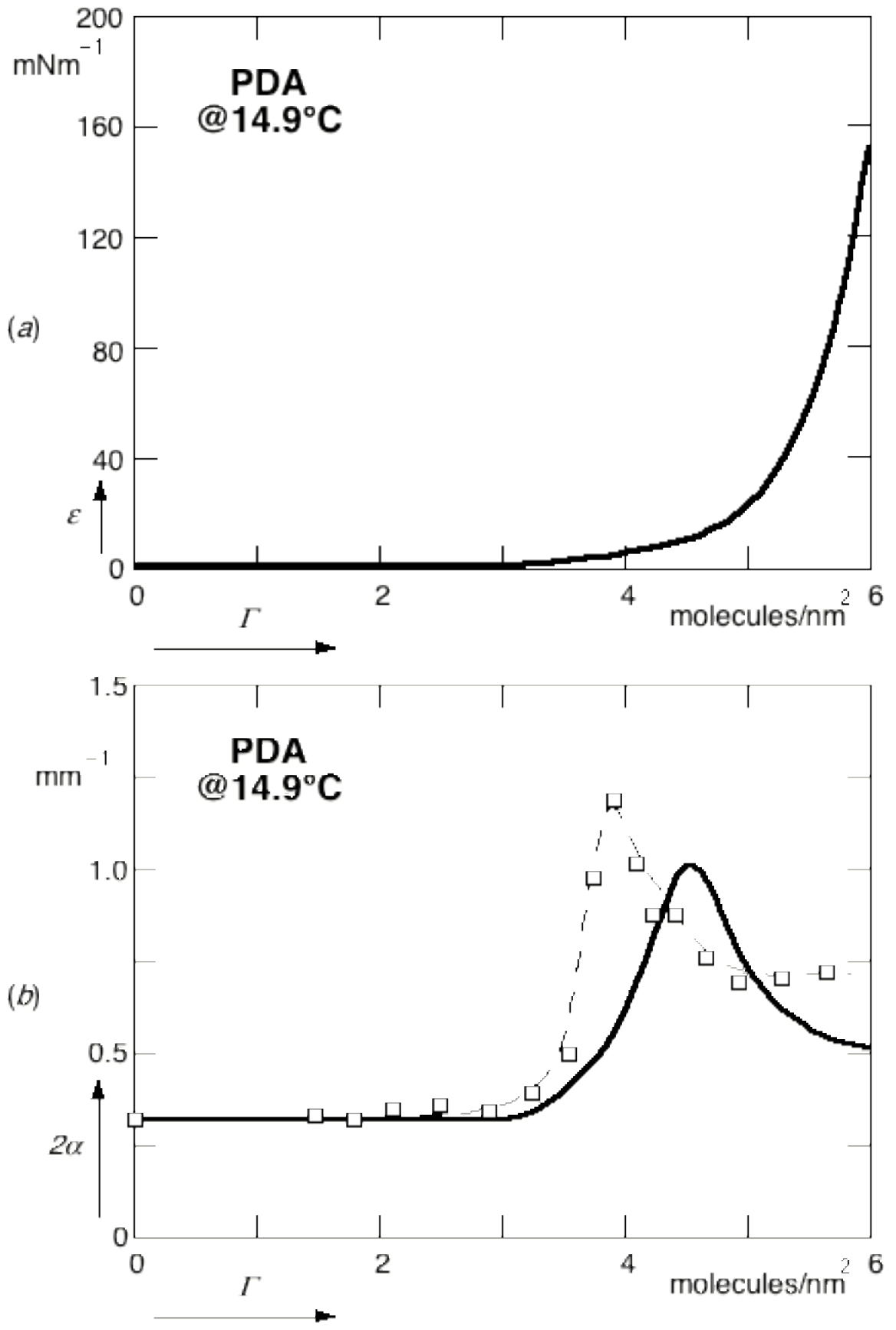


**Fig. 7.6** Plotted against the surface concentration are: (a) the static elasticity values obtained from isotherm measurements; (b) experimentally observed damping coefficients (squares) and the corresponding predictions (solid line) obtained using Eq. (7.27)

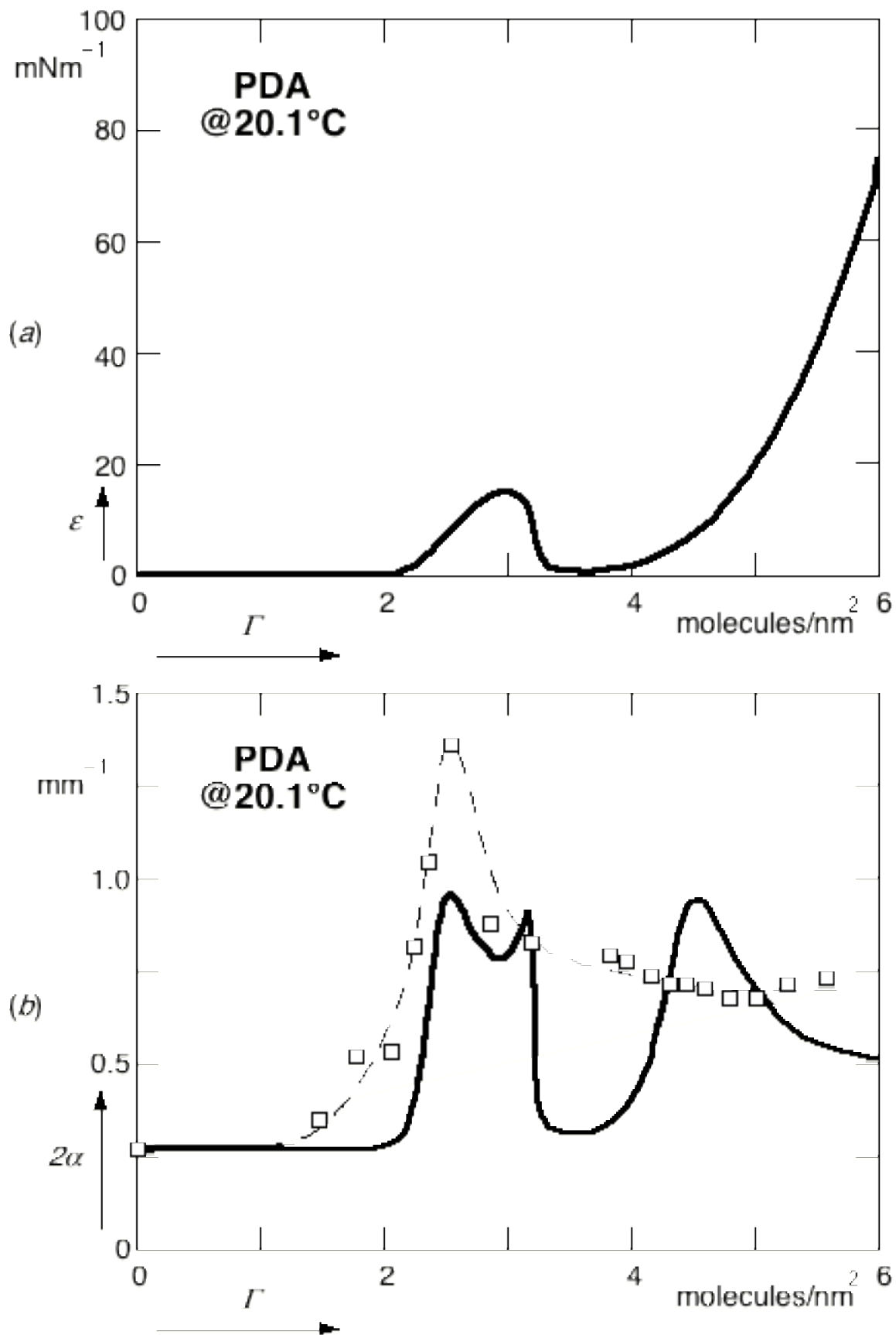


Fig. 7.7 Plotted against the surface concentration are: (a) the static elasticity values obtained from isotherm measurements; (b) experimentally observed damping coefficients (squares) and the corresponding predictions (solid line) obtained using Eq. (7.27)

Using Eq. (7.27) we can now obtain the spatial damping coefficient as a function of surface concentration from the calculated elasticity. The results are shown in Figs. 7.6 (b) and 7.7 (b). Comparing the measured spatial damping results at 14.9 °C, with the calculated values in Fig. 7.6 (b), we find that the results agree qualitatively. Although both plots show a maximum in damping, the exact location and size of the maximum are different. The discrepancy in the peak location may be due to uncertainty in the surface pressure measurement as well as accuracy of the polynomial fit used to obtain the elasticity curve, while that in the damping value may be due to additional dissipative processes. Above the triple point the agreement is not as good, see Fig. 7.7(b). Instead of a single maximum in the spatial damping curve, as observed experimentally, the theory predicts three peaks. This prediction is due to the existence of the second plateau which causes the elasticity curve to fall back to zero from some finite value at the low concentration end of the LE–LC coexistence region, and rise up again at the high concentration end. As a result, the curve in Fig. 7.7 (a) coincides with the calculated value  $\varepsilon_{max} = 10.91 \text{ mN}\cdot\text{m}^{-1}$  (see Table 7.1) in three different locations. Although the first of the three peaks agrees well with the experimental one, see Fig. 7.7(b), the hydrodynamic theory as outlined here cannot fully account for the observed damping.

One explanation for the damping peak has its basis on the coupling between different modes of surface waves. Apart from the transverse capillary waves at the interface, Lucassen discovered that there exists another kind of surface waves, a longitudinal surface wave [Lucassen, 1968], which obeys the same boundary conditions. He and his co-worker explained the maximal spatial damping as a resonance phenomenon involving these two types of wave motion. The resonance condition is satisfied when the wavelength of the

transverse capillary wave at a given frequency equals that of the longitudinal surface wave [Lucassen-Reynders and Lucassen, 1969]. and their computer calculations indicate that this resonance condition is met only when the surface dilational modulus assumes the value  $\varepsilon_{max}$  in Eq. (7.33). In other words, this argument, like the theory in Section 7.2 and 7.3, also predicts a peak in damping to occur when  $\varepsilon = \varepsilon_{max}$ . While the coupling between longitudinal surface waves and transverse capillary waves may exist and account for the extra damping observed experimentally (see Table 7.1), this argument still predicts three peaks to occur for a system with a elasticity curve like the one in Fig. 7.7 (a) and cannot explain the single peak observed experimentally as indicated in Fig. 7.7 (b).

The hydrodynamic theory described in Sections 7.2 and 7.3 describes surface wave propagation at a liquid-vapor interface in the presence of a homogeneous monolayer. From fluorescent microscopy, we learn that the monolayer is inhomogeneous in the coexistence regions [Moore, Knobler, *et al.*, 1990], but as far as we know, there exists no theoretical treatment of surface wave propagation at an interface covered with an inhomogeneous monolayer. The existence of domain structures in the coexistence region, unaccounted for in the above theory, may help explain the location of the maximum, as well as consistently higher damping value obtained experimentally.

Surface waves propagating at an interface cause periodic contraction and expansion. This periodic change in surface area translates into a periodic change in the surface concentration of surfactant molecules. In the G-LE coexistence region, such a variation modifies the ratio of surfactant molecules in the gaseous phase to those in the LE phase. In the low surface concentration end of the region, this change does not affect the inhomogeneous nature of the surface film. At higher concentrations near the coexistence phase boundary, where the G-LE

transition is approaching completion<sup>18</sup>, oscillations in the surface concentration may drive the monolayer back and forth between a homogeneous and inhomogeneous film. With a fixed wave amplitude, this effect is expected to be most pronounced around the coexistence phase boundary. Recent work by Miyano and Tamada on capillary wave propagation at an interface covered with an inhomogeneous monolayer in the G-LE coexistence region also demonstrates the lack of surface film influence until a 90 % coverage of the LE phase is attained [Miyano and Tamada, 1992]. Repeated switching back and forth between a homogeneous and inhomogeneous film leads to the continuous breakage and formation of island domains in the monolayer. Such a process is not be described by the hydrodynamic theory previously discussed. The additional energy dissipated<sup>19</sup> by this switching mechanism may account for the increased damping observed at higher concentrations in the G-LE coexistence region, as well as the discrepancy between the theoretical and experimental values of  $\alpha_{\max}$  (see Table 7.1). In addition, this process may also explain the correspondence between the maximal spatial damping coefficient and the initiation of surface pressure growth. One should note that this effect comes into play only when the domain response time is shorter than the period of the capillary wave.

Similar to the G-LE coexistence region, the LE-LC coexistence region is also inhomogeneous, exhibiting domain structures. If the damping peak is sensitive to the conversion process of a homogeneous film to an inhomogeneous one, and vice-versa, one would expect damping peaks to be located at the beginning and end of the LE-LC transition. Our experimental findings, however,

---

<sup>18</sup>When the monolayer enters the LE phase, a complete liquid film coverage is attained, and a homogeneous film is resulted.

<sup>19</sup>This energy can be thought of as equivalent to the latent heat in first-order phase transitions.

show otherwise. The absence of damping peaks may be due to the difference in phase characteristics, like compressibility, for instance, between the two coexistence regions.

## 7.6 Damping as a Probe of Phase Transitions

In Section 6.4, we described the difficulties encountered in mapping out the phase boundaries and finding the critical temperature,  $T_c$ , of the G-LE coexistence region of PDA. Because the surface pressure changes in this region are small, isotherm measurements require great care, and similar experimental data can lead to very different conclusions depending on the criteria used to interpret the data. Fluorescence microscopy, on the other hand, provides clear pictures of the surface morphology, but requires the addition of fluorescent dyes which may alter the phase behavior of the film. The damping results discussed in Section 7.4 indicates that peaks in the spatial damping coefficient occur at the surface concentrations which signify the initiation of surface pressure growth. Analogous results have been observed in temporal damping measurements [Chen, Sano, *et al.*, 1986]. Such results suggest that capillary wave damping measurements provide a sensitive tool for locating the phase transitions of a monolayer. In the case of PDA, damping results allow us to identify the high concentration end of the G-LE phase boundary. Table 7.2 shows the experimentally determined values of surface area for which maximal damping occurs at various temperatures. These values agree well with the phase boundary on the high surface concentration end of the G-LE coexistence region obtained by other workers (see Table 6.1).

| $T$ (°C) | $\mathcal{A}_{LE}$ or $\mathcal{A}_{LC}$ (Å <sup>2</sup> ) |
|----------|--|
| 14.9     | 25   |
| 20.1     | 40   |
| 30.3     | 51   |

**Table 7.2** Experimentally determined values of surface area at which maximal damping occurs at various temperatures.

Although our damping results do not allow us to locate the low concentration end of the G-LE phase boundary, the observed increase in surface area,  $\mathcal{A}_{LE}$ , with increasing temperature indicates that the coexistence region diminishes in size with increasing temperature until the critical temperature,  $T_c$ , for the formation of the LE phase is reached. The determination of the critical temperature from capillary wave damping measurements is, however, not as simple as we do not completely understand the damping mechanism or the behavior of the isotherms above the critical point. If as outlined in Section 7.5, the damping peak can be attributed to the additional energy dissipated involved in the forming of a coherent film, one would expect the peak to disappear above the critical temperature. If, on the other hand, one subscribes to the hydrodynamic theory in Sections 7.2 and 7.3, a peak should exist above  $T_c$ , at the surface dilational modulus given by Eq. (7.33). Depending on the specific shape of the isotherm<sup>20</sup>, this peak may be broadened or occur at a much lower surface

---

<sup>20</sup>For temperatures well above the critical point, the surface film is expected to behave like an ideal-gas; for an isotherm with a small slope, the damping peak is expected to be significantly broadened, and for an isotherm with a large slope, the damping peak is expected to occur at a much lower surface concentration. For temperatures above but close to the critical temperature, it is well-known that the isotherms may have inflection points which can result in damping behavior similar to that observed below the critical point.

concentration. With the information available, it is not possible to determine  $T_c$  exactly.

## 7.7 Conclusion and Future Work

Using hydrodynamic theory, we reviewed the damping of capillary waves at a liquid-vapor interface in the presence of a homogeneous monolayer of surfactant molecules. We also carried out direct measurements of the spatial damping coefficient for such waves traveling on a water-air interface with an adsorbed monolayer of PDA, at temperatures ranging from below the PDA triple point to 40 °C. A maximum in spatial damping as a function of surface concentration is observed at all temperatures, and occurs at a concentration which marks the initial rise of the surface pressure from its zero value. The discrepancies between hydrodynamic predictions and experimental results may be explained by the inhomogeneous nature of the film in the coexistence region. The simple hydrodynamic theory presented in Sections 7.2 and 7.3 does not allow for an inhomogeneous surface configuration. In Section 7.5, we give a heuristic argument which may explain the additional dissipation observed at the coexistence phase boundary. Comparison between the position at which maximal spatial damping occurs and measurements of the phase boundary surface area,  $A_{LE}$ , found by other workers, shows good agreement, suggesting that the spatial damping of capillary waves can be used as an indicator of phase transitions. Our search for a critical temperature of the G-LE transition was, however, inconclusive.

A better understanding of damping in the vicinity of the critical temperature is necessary to determine if capillary wave damping measurements

can provide useful information in this regime. Damping measurements with monolayers of esters of different chain length (some with established critical temperature below room temperature) will be performed and may elucidate the physics near the critical temperature. The effects of inhomogeneous monolayer films on capillary wave damping are still not well understood. The ability to observe the structure of the monolayer while carrying out spatial damping measurements may lead to better understanding. A Brewster angle microscopy<sup>21</sup> setup is being built to allow such direct observation of the surface morphology.

The study of surface wave damping has a long history, yet various aspects of the observed behavior and underlying mechanisms are not well understood. It is my hope that this set of experiments will stimulate new theoretical and experimental efforts in the field, leading to insights into the viscoelastic properties of surface films, and elucidating the basic concepts of surface wave damping.

---

<sup>21</sup>This microscope employs the characteristics that *p*-polarized light has zero reflectivity at Brewster angle. The formation of a monolayer at the interface slightly modifies the Brewster angle, and different domains give different reflectivities for the incident light. The Brewster angle microscopy therefore allows one to detect monolayer inhomogeneity [Henon and Meunier, 1991, Honig and Mobius, 1991].

## References

- Aiken, *Proc. Roy. Soc., Edin. (V)*, **12**, 56 (1883).
- Atkins, P.W., *Physical Chemistry* (W.H. Freeman & Co., San Francisco, 1982).
- Chen, Y.-L., Sano, M., M. Kawaguchi, H.Y. and Zografis, G., *Langmuir*, **2**, 349 (1986).
- Davies, J.T. and Vose, R.W., *Proc. Roy. Soc.*, **A286**, 218 (1965).
- Dippy, J.A.G., *Chem. Rev.*, **25**, 151 (1939).
- Dorrestein, R., *Koninkl. Ned. Akad. Wetenschap. Proc.*, **B45**, 260 (1951).
- Franklin, B., *Roy. Soc. London, Philos. Trans.*, **64**, 445 (1774).
- Goodrich, F.C., *Proc. Roy. Soc. (London)*, **A260**, 481 (1961).
- Hansen, R.S. and Mann, J.A., *J. Appl. Phys.*, **35**, 152 (1964).
- Harkins, W.D., *The Physical Chemistry of Surface Films* (Reinhold Publishing Corporation, New York, 1952).
- Henon, S. and Meunier, J., *Rev. Sci. Instrum.*, **62**, 936 (1991).
- Honig, D. and Mobious, D., *J. Phys. Chem.*, **95**, 4590 (1991).
- Levich, V.G., *Act. Phys. U.R.S.S.*, **14**, 307 (1941).
- Levich, V.G., *Physicochemical Hydrodynamics* (Prentice-Hall, Englewood Cliff, New Jersey, 1962).
- Lucassen, J., *Trans. Faraday Soc.*, **64**, 2221 (1968).
- Lucassen-Reynders, E.H. and Lucassen, J., *Adv. Coll. Int. Sci.*, **2**, 347 (1969).
- Miyano, K. and Tamada, K., *Langmuir*, **8**, 160 (1992).

Moore, B.G., Knobler, C.M., Akamatsu, S. and Rondelez, F., *J. Phys. Chem.*, **94**, 9588 (1990).

Nelson, D., **unpublished report**, (1985).

Pallas, N.R. and Pethica, B.A., *J. Chem Soc., Fara. Trans1*, **83**, 585 (1987).

Plinius, *Historia Naturalis*

Rayleigh, L., *Proc. Roy. Soc. London*, **47**, 364 (1890).

Reynolds, O., *Brit. Ass. Rep.*, (1880).

Tempel, M.v.d. and Riet, R.P.v.d., *J. Chem. Phys.*, **42**, 2769 (1965).

## Chapter 7

# Damping of Capillary Waves at Liquid Surfaces covered with Insoluble Monolayers

The damping of capillary waves on the surface of a pure liquid of low viscosity is presented in Chapter 5. Surfactants can have a drastic effect on this damping. These changes occur because of the viscous and elastic properties of the adsorbed monolayer, which resists the periodic expansion and compression of the surface. Below we present a theory for the damping of capillary waves on a liquid surface covered by a surfactant monolayer. Next, we show experimental data taken on a water-air interface covered by a monolayer of pentadecanoic acid and obtain from the data a phase boundary for the gas-liquid transition.

## 7.1 Background

The effect of surfactants on the wave motion of a liquid surface has been known since antiquity. The calming effect of oil on a rough sea was first noted by Pliny the Elder [Plinius] in the first century, and has since been common knowledge to seamen. In fact, most of the early observations on the effect of surface-active substances on ocean waves were made by sailors under trying conditions.

The first recorded experiment on the effect of oil on surface wave damping was carried out by Benjamin Franklin on the pond of Clapham Common in the late eighteenth century. In 1774, he described this famous experiment to his colleagues at the Royal Society in London [Franklin, 1774]:

*... the oil, though not more than a teaspoonful, produced an instant calm over a space several yards square, which spread amazingly, and extended itself gradually till it reached the lee side, making all that quarter of the pond, perhaps half an acre, as smooth as a looking glass. ...*

Franklin subsequently also carried out a number of experiments on the damping of surface wave by monolayers of oil. Since then, many experimental and theoretical studies have focused on the effect of surface-active substances on the damping of surface waves. It was not until 1883, however, that Aiken showed that the increase of surface wave damping by a surface film is due to the film's resistance to compression [Aiken, 1883].

It took over a hundred years after Franklin's experiments before it was realized that Franklin's oil film had a thickness on the order of molecular dimensions [Rayleigh, 1890]. Aiken was first to associate the increased damping

with the film's resistance to compression [Aiken, 1883]. Later work shows that the presence of a monomolecular film at a liquid-vapor interface changes the viscoelastic properties of the surface. This alters the boundary condition of the problem and leads to an increased damping of surface waves [Levich, 1941]. Theoretical studies have also shown that the calming of surface waves in the presence of a monolayer with finite dilational compressibility is due to the suppressed capillary wave generation, which, in turn, results in a reduced coupling between the liquid surface and the wind [Nelson, 1985].

In Section 5.2, we showed that for a pure interface, the boundary imposes the condition that the stresses from within the liquid balance out any stresses due to surface forces. As shown in Eqs. (5.28a) and (5.28b), the boundary condition thus requires that both the tangential and normal components of the viscous stress tensor be continuous. The normal components of the stress tensor is equal to the capillary pressure of the deformed surface as given by Laplace-Young's law (5.8), and is the same for both a pure interface and one with an adsorbed monolayer. A tangential component arises only when there is a surface tension gradient at the interface. For a pure interface the tangential component vanishes, since there can be no gradients in surface tension, see Eq. (5.28b). The picture is different for a monolayer-covered surface because the wave motion causes the monolayer to contract and expand and thus results in surface tension variations [Dorrestein, 1951, Goodrich, 1961, Hansen and Mann, 1964, Levich, 1941, Tempel and Riet, 1965].

The non-zero tangential components of the stress tensor depend on the extent and rate of surface deformation, and represent the resistance of the surface film to changes in both area and shape. The new surface viscoelastic properties introduced by the presence of a monolayer can therefore be

expressed by two moduli [Lucassen-Reynders and Lucassen, 1969]: 1) the surface dilational modulus, which is a measure of the surface film's resistance to changes in surface area, represented by a surface dilational elasticity,  $\varepsilon_d$ , and a surface dilational viscosity  $\eta_d$ ; 2) the surface shear modulus, which is the resistance to changes in the shape of the surface, represented by a surface shear elasticity,  $\varepsilon_s$ , and a surface shear viscosity  $\eta_s$ . In general, the effects of the surface shear modulus are assumed to be small compared those of the dilational modulus [Lucassen-Reynders and Lucassen, 1969]. If both the surface shear elasticity and viscosity are neglected, the only new viscoelastic coefficients are  $\varepsilon_d$  and  $\eta_d$ .

For the case where the surface dilational viscosity  $\eta_d$  is zero,<sup>1</sup> the surface dilational modulus is given by the surface dilational elasticity alone,

$$\varepsilon = \varepsilon_d(\omega). \quad (7.1)$$

In the static limit, the surface dilational elasticity is frequency independent, and is equivalent to the static elasticity,  $\varepsilon_d = \varepsilon_0$ . This static elasticity follows from the equilibrium relationship between surface tension  $\sigma$  and surface concentration of surfactant molecules,  $\Gamma_0$ , and is given by [Davies and Vose, 1965],

$$\varepsilon_0 = -\frac{\partial \sigma}{\partial \ln \Gamma_0}. \quad (7.2)$$

The surface dilational modulus is therefore directly related to measurable equilibrium surface properties in the purely elastic case.

These new viscoelastic properties alter the boundary conditions that constrain the wave motion. In the next section, we use these boundary

---

<sup>1</sup>The case of negligible surface dilational viscosity has been observed with a number of insoluble monolayers [Lucassen-Reynders, 1969 #10].

conditions to derive the velocity components of the surface wave and obtain a dispersion relation for waves on a surface covered with an insoluble monolayer.

## 7.2 Wave Motion at an Interface Covered with an Insoluble Monolayer

As for the case of a pure surface of an incompressible liquid, we start from the general solutions for the velocity components and pressure, which follow from the equation of continuity and the linearized Navier-Stokes equation,

$$v_x = \left( ikAe^{kz} - lCe^{lz} \right) e^{i(kx - \omega t)}, \quad (7.3)$$

$$v_z = \left( kAe^{kz} + ikCe^{lz} \right) e^{i(kx - \omega t)}, \quad (7.4)$$

$$p_o = i\rho\omega_o A e^{k_o z} e^{i(k_o x - \omega_o t)} - \rho g z, \quad (7.5)$$

see Chapter 5. The boundary conditions which constrain these solutions are, however, different from the pure case.

In the normal direction the boundary condition is still given by the Laplace-Young equation (see Eq. 5.28b). Neglecting, again, the pressure due to the vapor phase above the liquid, this condition becomes

$$p_{zz} = \sigma(\Gamma) \frac{\partial^2 \zeta}{\partial x^2}. \quad (7.6)$$

Note that the surface tension,  $\sigma(\Gamma)$ , is now a function of the surface concentration,  $\Gamma$ , and that  $\zeta$ , the vertical displacement of the liquid surface from its equilibrium position, is related to  $v_z$  by

$$\frac{\partial \zeta}{\partial t} = v_z. \quad (7.7)$$

Using  $v_z$  in Eq. (7.4), we can write  $\zeta$  in the form,

$$\zeta = \frac{kA + ikC}{-i\omega} e^{i(kx - \omega t)}. \quad (7.8)$$

A second boundary condition is given by the tangential component of the stress tensor, which is now no longer zero because of the additional viscoelastic properties introduced by the monolayer,

$$p_{zx} = \frac{\partial \sigma}{\partial \Gamma} \frac{\partial \Gamma}{\partial x}, \quad (7.9)$$

where  $\Gamma$  is a function of position on the surface.

Assuming the motion of the surface waves causes only small deviations of the surface concentration from its equilibrium value, the surface concentration can be written as

$$\Gamma = \Gamma_0 + \Gamma', \quad (7.10)$$

where  $\Gamma_0$  is the equilibrium surface concentration and  $\Gamma' \ll \Gamma_0$  the deviation from the equilibrium value. The surface concentration must obey conservation of mass [Levich, 1962]:

$$\frac{\partial \Gamma}{\partial t} + \frac{\partial}{\partial x}(\Gamma v_x) = D_s \frac{\partial^2 \Gamma}{\partial x^2}, \quad (7.11)$$

with  $D_s$  is the surface diffusion coefficient. Substituting Eqs. (7.3) and (7.10) into (7.11) and seeking a solution for the surface concentration deviation of the form,

$$\Gamma' = E e^{i(kx - \omega t)}, \quad (7.12)$$

the following expression is obtained for the constant  $E$ ,

$$E = \frac{-ik\Gamma_o(ikA - lC)}{-i\omega + k^2 D_s}, \quad (7.13)$$

where we have neglected all terms of second order contribution. For frequencies in the capillary wave regime, the term containing the diffusion coefficient in the denominator is small compared to the wave frequency, and the surface concentration reduces to

$$\Gamma = \Gamma_o + \frac{ik\Gamma_o(ikA - lC)}{i\omega} e^{i(kx - \omega t)}. \quad (7.14)$$

Substituting Eqs. (7.14) and (7.8) into (7.6), and approximating the value of  $\sigma(\Gamma) \approx \sigma(\Gamma_o)$ , the normal boundary condition in Eq. (7.11) now becomes

$$p_{zz} = \sigma(\Gamma_o) \frac{kA + ikC}{-i\omega} e^{i(kx - \omega t)}. \quad (7.15)$$

By a similar substitution of Eq. (7.14) into (7.12), the tangential boundary condition can be re-expressed as

$$p_{zx} = \frac{\varepsilon k^2}{i\omega} (ikA - lC) e^{i(kx - \omega t)}, \quad (7.16)$$

where the surface dilational modulus  $\varepsilon$  is defined as

$$\varepsilon \equiv -\frac{\partial \sigma}{\partial \Gamma} \Gamma_o. \quad (7.17)$$

Equating Eqs. (7.15) and (7.16) to the definitions of the normal and tangential boundary conditions given by

$$p_{zz} \equiv -p + 2\eta \frac{\partial v_z}{\partial z}, \quad (7.18)$$

$$p_{zx} \equiv \eta \left( \frac{\partial v_x}{\partial v_z} + \frac{\partial v_z}{\partial v_x} \right), \quad (7.19)$$

and substituting into them Eqs. (7.3) and (7.4), we obtain the following two equations relating the unknown quantities  $A$  and  $C$  :

$$\left(-\omega^2 - i\omega 2vk^2 + gk + \frac{\sigma}{\rho}k^3\right)A + i\left(gk + \frac{\sigma}{\rho}k^3 - i\omega 2vkl\right)C = 0, \quad (7.19)$$

$$i\left(-i\omega 2vk^2 + \frac{\varepsilon}{\rho}k^3\right)A - \left(-i\omega 2vk^2 - \omega^2 + \frac{\varepsilon}{\rho}k^2l\right)C = 0. \quad (7.20)$$

In the capillary wave regime, the terms due to gravity  $gk$  are negligible. Neglecting these terms and setting the determinant of the equations to zero, we obtain the following dispersion relation between the angular frequency and wavevector for a monolayer-covered surface:

$$\begin{aligned} & \left(\frac{\sigma}{\rho}k^3 - i\omega 2vkl\right)\left(-i\omega 2vk^2 + \frac{\varepsilon}{\rho}k^3\right) \\ & - \left(-i\omega 2vk^2 - \omega^2 + \frac{\varepsilon}{\rho}k^2l\right)\left(-\omega^2 - i\omega 2vk^2 + \frac{\sigma}{\rho}k^3\right) = 0 \end{aligned} \quad (7.21)$$

Setting  $\varepsilon$  to zero in the above equation, we recover the Lamb-Levich dispersion relation for a pure liquid,

$$(2vk^2 - i\omega)^2 + \omega_0^2 = 4v^2k^4 \sqrt{1 - \frac{i\omega}{vk^2}}. \quad (7.22)$$

In the general case, however, the dispersion relation is now a sixth-order polynomial in  $k$ ,

$$-\frac{\varepsilon\sigma}{\rho^2}k^6 + \omega^4 + i4vk^2\omega - \frac{\varepsilon}{\rho}k^2l\omega^2 - \frac{\sigma}{\rho}k^3\omega^2 + \frac{\varepsilon\sigma}{\rho^2}k^5l = 0. \quad (7.23)$$

The above dispersion relation for a surface covered with a monolayer is considerably more complicated than the Lamb-Levich equation, and cannot generally be solved analytically.

## 7.3 Damping

As for a pure surface, the angular frequency  $\omega$  and wavevector  $k$  in the dispersion equation (7.23) are complex quantities, with the imaginary parts representing damping of the wave motion. In evaluating damping in the monolayer-covered system, we will, as in the case of the pure liquid, be concerned only with liquids of low viscosity, where the following inequality

$$\frac{\omega}{2\nu k^2} \gg 1, \quad (7.24)$$

is satisfied.

Let us first evaluate the spatial damping coefficient of surface waves produced by a source of fixed amplitude. In this case, the amplitude of the wave at a given distance from the source does not decay with time; the falloff of the wave amplitude at different positions gives the spatial damping coefficient. For a surface wave of angular frequency  $\omega_0$  generated at some point on the surface, the associated wavevector  $k$  is complex. In the low-viscosity limit,  $k$  differs only slightly from the real value  $k_0$  of the pure case, given by Eq. (5.10), and can be written as

$$k = k_0 + k', \quad (7.25)$$

where  $k' = k'' + i\alpha$  represents the change in wavevector from the pure case. The real part of  $k'$  represents changes in the wavelength of the surface wave in the presence of a monolayer; the imaginary part  $\alpha \ll k_0$  is the spatial damping coefficient.

The spatial damping coefficient  $\alpha$  can be obtained by substituting Eq. (7.25) into the dispersion relation (7.23) and setting  $\omega = \omega_0$ . In the low-viscosity limit given by Eq. (7.24) the factor  $l$ , which is defined in Eq. (5.26) and which appears in the dispersion relation, reduces to

$$l \approx k_0 \sqrt{\frac{-i\omega_0}{\nu k_0^2}}. \quad (7.26)$$

Retaining only first order terms in  $\alpha$ , the dispersion relation yields a general solution for  $k'$ . The imaginary part  $\alpha$  of this solution, which accounts for the spatial damping of the waves is given by

$$\alpha = \frac{2k_0}{3\omega_0} \frac{\frac{\omega_0}{2\sqrt{2}} \left(\frac{\varepsilon}{\sigma}\right)^2 \sqrt{\frac{\omega_0}{\nu k_0}} - \frac{\varepsilon}{\sigma} \sqrt{2\nu k_0 \omega_0 + 2\nu k_0^2}}{1 - \sqrt{2} \frac{\varepsilon}{\sigma} \sqrt{\frac{\omega_0}{\nu k_0^2}} + \left(\frac{\varepsilon}{\sigma}\right)^2 \frac{\omega_0}{\nu k_0^2}}, \quad (7.27)$$

while the real part  $k''$  has the form,

$$k'' = \frac{k_0}{3} \frac{\varepsilon}{\sigma} \frac{1 - \frac{\varepsilon}{\sigma} \sqrt{\frac{\omega_0}{2\nu k_0^2}} - \frac{2}{\omega_0} \sqrt{2\nu k_0^2 \omega_0}}{1 - \sqrt{2} \frac{\varepsilon}{\sigma} \sqrt{\frac{\omega_0}{\nu k_0^2}} + \left(\frac{\varepsilon}{\sigma}\right)^2 \frac{\omega_0}{\nu k_0^2}}. \quad (7.28)$$

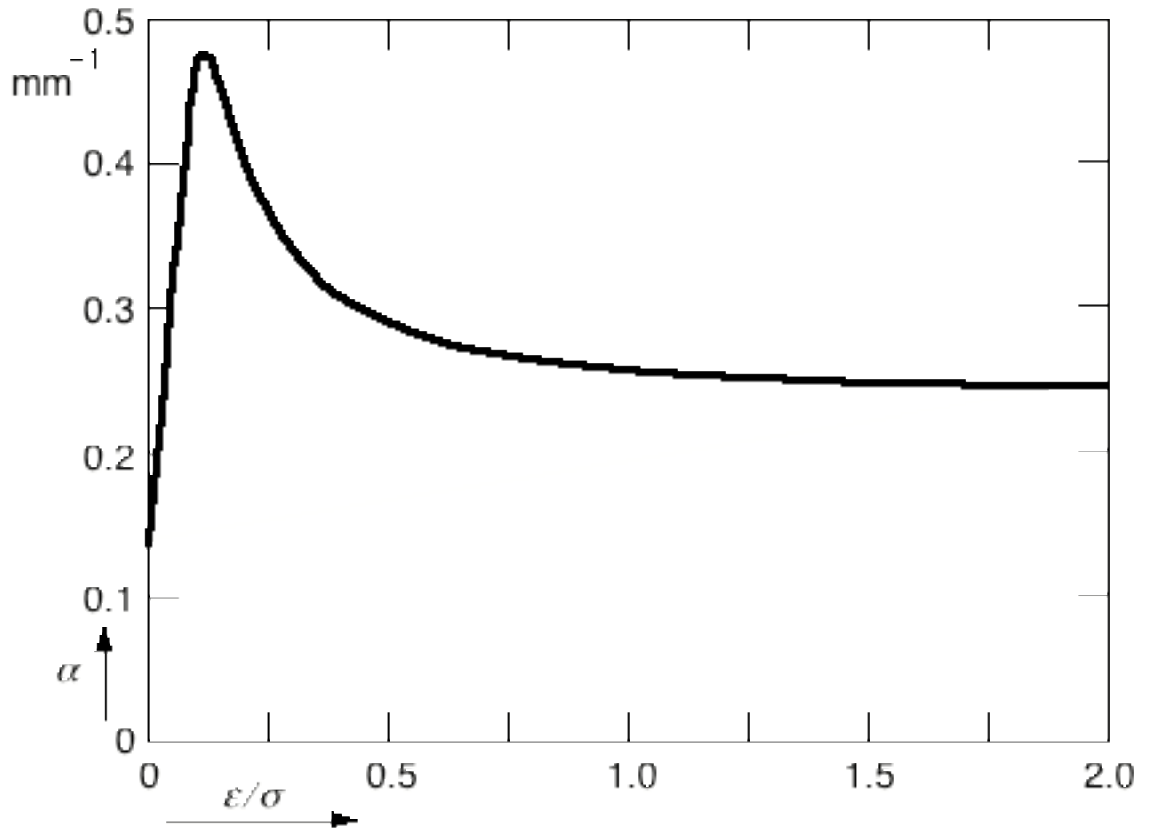


**Fig. 7.1** Calculated spatial damping coefficient as a function of the ratio between surface elasticity and surface tension using Eq. (7.27).

Equation (7.27) relates the spatial damping coefficient and the surface dilational modulus,  $\epsilon$ . In the limiting case of zero elasticity, the coefficient reduces to Stokes' value for a pure liquid, Eq. (5.37)

$$\alpha_0 = \frac{4\eta\omega_0}{3\sigma}. \quad (7.29)$$

Another limiting case is obtained for a totally inelastic surface, when  $\epsilon \rightarrow \infty$ . The damping coefficient then correctly reduces to the damping coefficient obtained by Reynolds [Reynolds, 1880],

$$\alpha_\infty = \frac{2k_0}{3\omega_0} \frac{\sqrt{vk_0^2\omega_0}}{2\sqrt{2}}. \quad (7.30)$$

The ratio of the coefficients in the two extreme limits is,

$$\frac{\alpha_{\infty}}{\alpha_0} = \frac{1}{4\sqrt{2}} \sqrt{\frac{\omega_0}{\nu k_0^2}}. \quad (7.31)$$

From the functional form of the spatial damping coefficient in Eq. (7.27) we see that the coefficient does not rise monotonically from its zero-elasticity value,  $\alpha_0$ , to its inelastic value,  $\alpha_{\infty}$ . Figure 7.1 shows the behavior of the spatial damping coefficient as a function of the ratio  $\varepsilon/\sigma$ . As can be seen the spatial damping goes through a maximum at a rather low value of the surface dilational modulus. The exact location of the maximum can be calculated by setting the partial derivative of  $\alpha$  with respect to  $\varepsilon$  to zero. The maximal value is thus found to be

$$\alpha_{max} = \frac{1}{3} k_0^2 \sqrt{\frac{2\nu}{\omega}}. \quad (7.32)$$

This maximum is achieved when the dilational modulus assumes the value,

$$\varepsilon_{max} = \frac{\sqrt{2\nu\rho^2\omega_0^3}}{k_0^2}. \quad (7.33)$$

Notice that the maximum spatial damping coefficient is twice as large as that for an inelastic surface, Eq.(7.30).

Now we turn to the temporal decay of thermally excited capillary waves. Consider a thermally excited wave with a fixed, real wavevector  $k_0$ . The associated angular frequency is now complex and its imaginary part represents the temporal damping of the waves. In the low-viscosity regime, the angular frequency in the presence of a monolayer can be written as

$$\omega = \omega_0 + \omega', \quad (7.34)$$

where  $\omega' = \omega'' - i\beta$  represents the change in frequency from the frequency  $\omega_0$  of a surface wave of wavevector  $k_0$  in the absence of a monolayer. The imaginary part  $\beta \ll \omega_0$  is the temporal damping coefficient. The coefficient,  $\beta$ , is obtained by substituting the wavevector,  $k_0$ , and the angular frequency,  $\omega$ , in Eq. (7.34) into the dispersion relation given by Eq. (7.23). Using Eq. (7.26), neglecting small terms in accordance with inequality (7.24), and retaining only first order terms in  $\beta$ , the dispersion relation yields a general solution for  $\omega'$ . The imaginary part of this solution, which accounts for the temporal damping of the waves is given by

$$\beta = \frac{\frac{\omega_0}{2\sqrt{2}} \left(\frac{\varepsilon}{\sigma}\right)^2 \sqrt{\frac{\omega_0}{\nu k_0^2}} - \frac{\varepsilon}{\sigma} \sqrt{2\nu k_0^2 \omega_0} + 2\nu k_0^2}{1 - \sqrt{2} \frac{\varepsilon}{\sigma} \sqrt{\frac{\omega_0}{\nu k_0^2}} + \left(\frac{\varepsilon}{\sigma}\right)^2 \frac{\omega_0}{\nu k_0^2}}, \quad (7.35)$$

while the real part has the form

$$\omega'' = \frac{\omega_0}{2} \frac{\varepsilon}{\sigma} \frac{1 - \frac{\varepsilon}{\sigma} \sqrt{\frac{\omega_0}{2\nu k_0^2}} - \frac{2}{\omega_0} \sqrt{2\nu k_0^2 \omega_0}}{1 - \sqrt{2} \frac{\varepsilon}{\sigma} \sqrt{\frac{\omega_0}{\nu k_0^2}} + \left(\frac{\varepsilon}{\sigma}\right)^2 \frac{\omega_0}{\nu k_0^2}}. \quad (7.36)$$

The temporal damping coefficient for a pure liquid surface,

$$\beta_0 = 2\nu k^2, \quad (7.37)$$

is recovered from Eq. (7.35) by setting the dilational modulus  $\varepsilon$  to zero.

Notice that the spatial damping coefficient  $\alpha$  in Eq. (7.27) and the temporal damping coefficient  $\beta$  in (7.35) are related by

$$\alpha = \frac{\beta}{\left(\frac{3\omega_0}{2k_0}\right)}. \quad (7.38)$$

The denominator in the above relation is the group velocity derived from the Kelvin equation. Notice that Eq. (7.38) is formally identical to (5.42) which relates the two damping coefficients in the case of a pure liquid surface. That this simple relation between the coefficients is true even for a monolayer-covered surface, and that the proportionality constant is the group velocity derived from the Kelvin equation may seem surprising. However, if one examines the wavevector (or frequency) corrections introduced by  $k''$  (or  $\omega''$ ), one finds that the changes are small<sup>2</sup>; therefore, to first order, the Kelvin equation is still an excellent approximation.<sup>3</sup>

## 7.4 Experimental Results

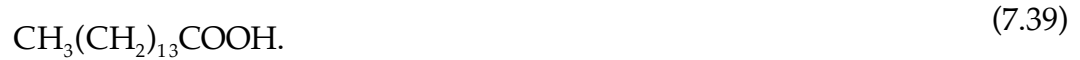
In Section 5.4, we presented data on the spatial damping coefficient for capillary waves on a pure liquid-vapor interface obtained using the differential Fourier transform heterodyne technique (see Section 4.2.2); the results are in excellent agreement with predictions given by hydrodynamic theory. We used the same experimental apparatus and optical setup to study spatial damping of capillary waves at a liquid-vapor interface in the presence of an adsorbed monolayer. As before, the measurements were carried out in a sealed chamber and capillary waves of a known frequency are induced using electrocapillarity. The resulting spectra are similar to the one shown in Fig. 4.7.

---

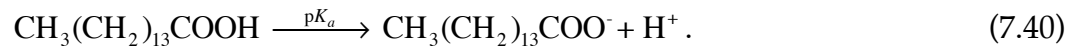
<sup>2</sup>For a capillary wave of frequency  $f = 1200$  Hz propagating on a water surface, the wavelength correction according to Eq. (7.28) is less than 3%.

<sup>3</sup>Substituting, for a completely inelastic surface,  $\varepsilon \rightarrow \infty$  into the dispersion relation (7.23) and retaining only terms containing  $\varepsilon$ , one recovers the Kelvin equation (with the gravity term omitted).

The surfactant used in this experiment is pentadecanoic acid (PDA), which is a fatty acid with a polar –OH headgroup and a 15-carbon hydrophobic tail, represented by the chemical formula,



This weak acid dissociates in water by undergoing the following reaction,



The dissociation constant of PDA,  $\text{p}K_a$ , is given by<sup>4</sup>

$$\text{p}K_a = -\log \frac{[\text{CH}_3(\text{CH}_2)_{13}\text{COO}^-][\text{H}^+]}{[\text{CH}_3(\text{CH}_2)_{13}\text{COOH}]}, \quad (7.41)$$

and is related to the  $\text{pH}^5$  of the subphase by the following equation:

$$\text{p}K_a - \text{pH} = -\log \frac{[\text{CH}_3(\text{CH}_2)_{13}\text{COO}^-]}{[\text{CH}_3(\text{CH}_2)_{13}\text{COOH}]}. \quad (7.42)$$

Since the dissociation constant for PDA is 5.6 [Dippy, 1939], one finds that 96% of the surfactant molecules dissociate when PDA is spread on a neutral water subphase ( $\text{pH} = 7$ )<sup>6</sup>. An acidic subphase is therefore necessary to minimize the dissociation of surfactant molecules. From Eq. (7.42) one finds that only 0.03% of

---

<sup>4</sup>Square brackets in the equation denote the concentration of the bracketed compound.

<sup>5</sup> $\text{pH}$  is related to the concentration of  $\text{H}^+$  ions by the relation [Atkins, 1982]

$$\text{pH} = -\log[\text{H}^+].$$

<sup>6</sup>Using Eqn. (7.42), one finds that for  $\text{pH} = 7$ ,

$$\frac{[\text{CH}_3(\text{CH}_2)_{13}\text{COO}^-]}{[\text{CH}_3(\text{CH}_2)_{13}\text{COOH}]} = 10^{1.4} = 25.12.$$

the molecules dissociate when the acid is spread on a subphase with a pH of 2<sup>7</sup>, and the percentage further reduces by an order of magnitude when the pH of the subphase is 1. The acidic aqueous subphase used in the experiment, described in Section 4.1.4, is a solution made by adding concentrated hydrochloric acid<sup>8</sup> to the ultrapure water sample<sup>9</sup>. A subphase of pH 2 is used for low temperature (< 30 °C) measurements, and a pH-1 subphase for high temperatures (>30 °C).

A solution of PDA<sup>10</sup> of known concentration is made with ultrahigh purity chloroform<sup>11</sup>. The monolayer is spread by carefully applying a small amount of the chloroform solution onto the surface of the aqueous subphase using a microliter syringe<sup>12</sup>. Access of the syringe to the sealed chamber is provided by one of the inlet ports on the front panel (see Section 4.1.5), and a 9-inch needle<sup>13</sup> is connected to the syringe to allow the point of application to be directly above the trough. The chloroform is allowed to evaporate for at least 20 minutes before the chamber is flushed several times with ultrahigh purity nitrogen<sup>14</sup>. Measurements are made only after the system is left undisturbed for

---

<sup>7</sup>For pH = 2,

$$\frac{[\text{CH}_3(\text{CH}_2)_{13}\text{COO}^-]}{[\text{CH}_3(\text{CH}_2)_{13}\text{COOH}]} = 10^{-3.6} = 0.0002.$$

<sup>8</sup>Ultrex II Reagent, Baker Analyzed

<sup>9</sup>Throughout 18-MΩ, deionized and distilled water from a Milli-Q UV+ system, by Millipore Corporation, is used.

<sup>10</sup>Pentadecanoic acid 99+%, F.W. = 242.40, Aldrich Chemical Company.

<sup>11</sup>Reagent, Baker Analyzed.

<sup>12</sup>100-μl Gastight® high-performance syringe with Teflon Luer lock, Hamilton Company.

<sup>13</sup>9-inch sharp-point 22s-gauge needle for 100-μl syringe volume, Hamilton Company.

<sup>14</sup>99.999% purity with < 0.5 ppm total hydrocarbon content, Igo's.

at least two hours to assure complete mechanical and thermal equilibrium of the monolayer.

We studied the effect of monolayers on capillary wave damping as a function of surface concentration over a range of temperatures. The surface concentration is varied by either reducing the surface area, or by successively spreading a known amount of chloroform solution of PDA onto the subphase surface. The surface tension of the system is monitored by the surface balance described in Section 4.1.3. All measurements were carried out at a frequency of 1.2 kHz. The temperature ranges from 14.9 °C, which lies below the triple point for PDA [Harkins, 1952, Moore, Knobler, *et al.*, 1990, Pallas and Pethica, 1987],

$$T_{TP} \approx 17^\circ\text{C}, \quad (7.43)$$

to 40.2 °C. Because of convection, increased humidity inside the chamber<sup>15</sup>, and increased solubility of surfactant molecules into the aqueous subphase, it is difficult to carry out measurements above 40 °C. The experimental results are plotted in Figs. 7.2 – 7.5, which show surface pressure and spatial damping as a function of surface concentration at the various temperatures.

The data in Fig. 7.2 were measured at 20.1 °C, a temperature above the triple point of PDA. As discussed in Section 6.3, we expect two plateau regions in the  $\Pi$ - $\Gamma$  isotherm at this temperature, one corresponding to the G-LE coexistence region, and the other to the LE-LC coexistence region. These plateaus can indeed be seen in the surface pressure data of Fig. 7.2 (a). The G-LE coexistence plateau

---

<sup>15</sup>The increased humidity leads to condensation on the windows and on the motors and encoders.

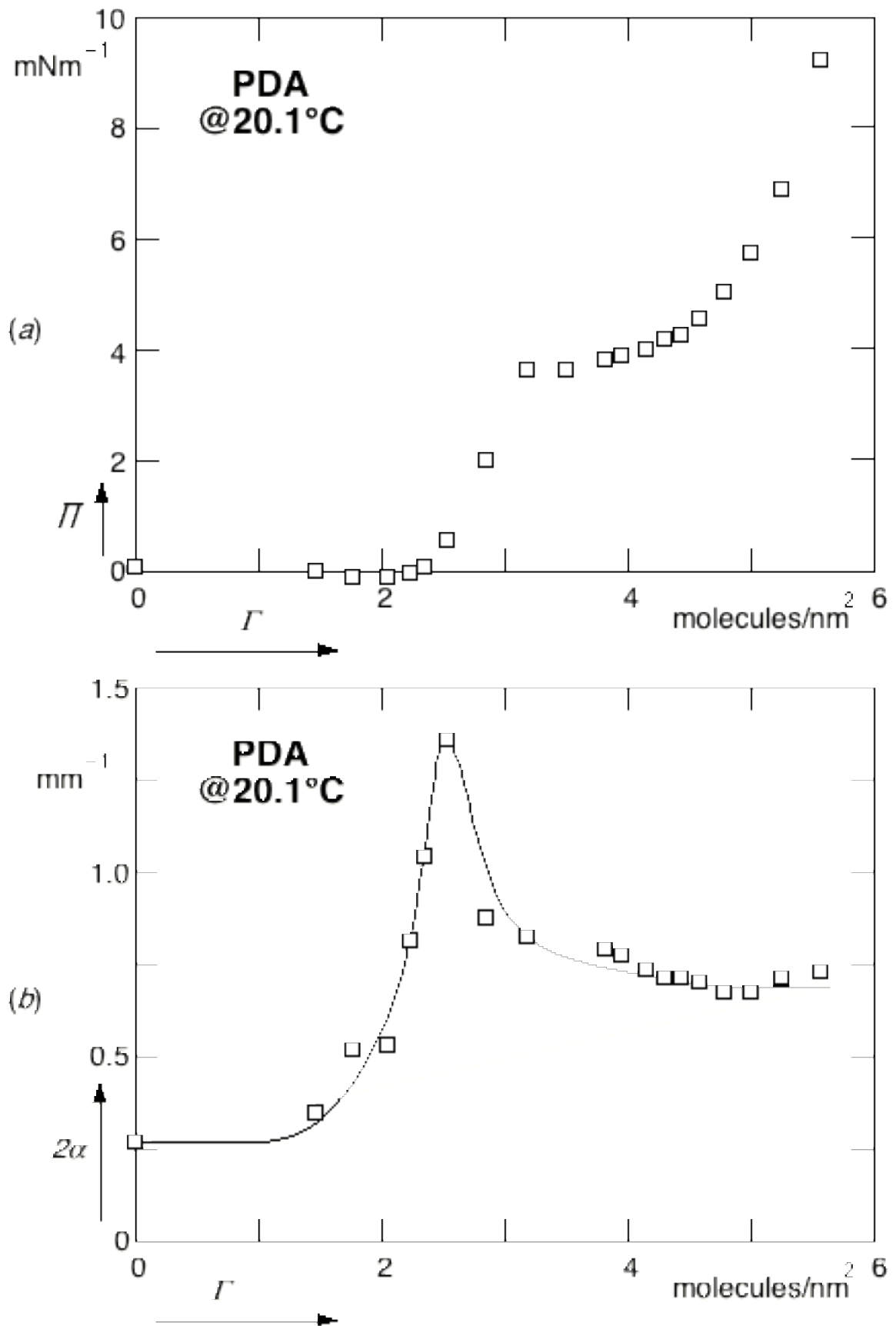


**Fig. 7.2** (a) Surface pressure  $\Pi$  and (b) damping coefficient  $\alpha$  as a function of surface concentration  $\Gamma$  for pentadecanoic acid adsorbed at a water-air interface at 20.1 °C. Capillary waves of frequency 1200 Hz were induced at the interface for the damping measurements.

occurs at low surface concentrations, and the measured surface pressure is essentially zero. The end of the G-LE transition occurs at a surface concentration,  $\Gamma_{LE}$ , of about 2.4 molecules/nm<sup>2</sup><sup>16</sup>. The LE-LC coexistence plateau is found at higher surface concentrations, spanning the range from 3.2 to 3.9 molecules/nm<sup>2</sup>.

The corresponding spatial damping coefficients are shown in Fig. 7.2 (b). Each point in this figure is determined by measuring the exponential decay of the induced capillary waves from a plot of wave amplitude ratio *vs.* distance, as in Fig. 5.3. Each value of this wave amplitude ratio is, in turn, obtained from a spectrum analogous to that in Fig. 5.2. Up to a surface concentration of 1.4 molecules/nm<sup>2</sup> the spatial damping coefficient is nearly constant and, within experimental error, identical to the one for pure water. Beyond 1.4 molecules/nm<sup>2</sup>, the spatial damping coefficient shows a sharp increase and a maximum is reached at a surface concentration of  $\Gamma_{max} = 2.5$  molecules/nm<sup>2</sup>. As the surface concentration is further increased, the damping coefficient decreases and levels out.

At 1.4 molecules/nm<sup>2</sup>, when the rise in the damping sets in, the monolayer is in the G-LE coexistence region. Recall that this region is characterized by islands of surfactant molecules in the gaseous phase surrounded by surfactant molecules in the LE phase (see Section 6.3). The data in Fig. 7.2 (b) indicate that the damping is unaffected when the fraction of molecules in the gaseous phase is high. The maximum in the damping occurs near the end of the G-LE coexistence region at a surface concentration of  $\Gamma_{LE}$ .

---

<sup>16</sup>We have not investigated at what surface concentration the transition from the gaseous phase to the LE phase begins, but other workers find that this takes place at a surface concentration of < 0.16 molecules/nm<sup>2</sup> [Pallas, 1987 #14; Kim, 1976 #19].

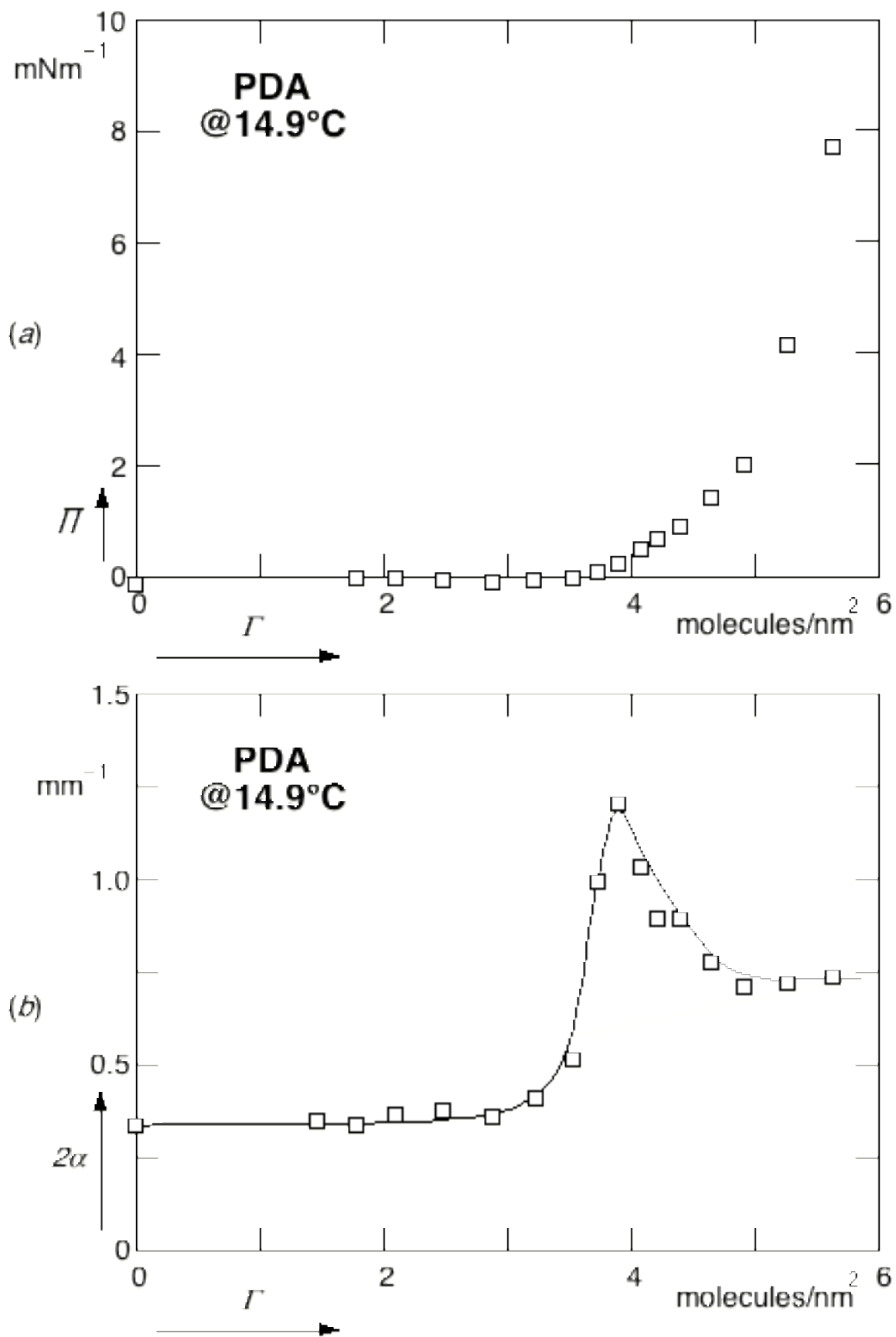


**Fig. 7.3** (a) Surface pressure  $\Pi$  and (b) damping coefficient  $\alpha$  as a function of surface concentration  $\Gamma$  for pentadecanoic acid adsorbed at a water-air interface at 14.9 °C. Capillary waves of frequency 1200 Hz were induced at the interface for the damping measurements.

Figure 7.3 shows data obtained at 14.9 °C, which lies below the triple point of PDA. Isotherms below the triple point have only one plateau; the LE phase is no longer observed as the film sublimates from the gas phase to the more condensed LC phase. The  $\Pi$ - $\Gamma$  isotherm in Fig. 7.3 (a) indeed shows only a single plateau and the surface pressure remains zero up to much higher surface concentration than above the triple point. The surface pressure starts to rise at  $\Gamma_{LC} = 3.9$  molecules/nm<sup>2</sup>, indicating the end of the transition and the emergence of a pure LC phase.

Unlike the measurements at 20.1 °C, where the rise in the damping sets in at  $\Gamma = 1.4$  molecules/nm<sup>2</sup>, below the triple point a rise is not observed until a much higher surface concentration of 3.0 molecules/nm<sup>2</sup> is reached, see Fig. 7.3 (b).<sup>17</sup> The maximum now occurs at a surface concentration  $\Gamma_{max} = 3.9$  molecules/nm<sup>2</sup>. As before, when the surface concentration is further increased, the damping coefficient decreases and levels out.

It is believed that the surface morphology in the G-LC coexistence region is similar to that in the G-LE region, where islands of surfactant molecules in the gaseous phase float in a sea of molecules in the condensed LC phase [Moore, Knobler, *et al.*, 1990]. The spatial damping results of Fig. 7.3 (b) show that the damping coefficient remains close to that of a pure water interface at low surface concentrations. In this case the maximum coincides with the end of the G-LC transition at  $\Gamma_{LC}$ .

Figures 7.4 (a) and 7.4 (b) show the results obtained at 30.3 °C. The G-LE and LE-LC coexistence regions are now smaller. The first plateau extends to a surface concentration,  $\Gamma_{LE} = 1.9$  molecules/nm<sup>2</sup>, while the second plateau spans

---

<sup>17</sup>At this concentration the monolayer is well within the G-LC coexistence region.

the range 2.4–2.7 molecules/nm<sup>2</sup>. The rise in damping sets in at 1.1 molecules/nm<sup>2</sup> and achieves a maximum at  $\Gamma_{max} = 1.9$  molecules/nm<sup>2</sup>, at the point where the surface pressure begins to increase. As before the coefficient decreases and then levels out as the surface concentration is increased further.

The results obtained at 40.2 °C are shown in Figs. 7.5 (a) and 7.5 (b). At this high temperature the solubility of PDA increases and not all PDA molecules remain at the interface; the actual surface concentration is therefore probably lower than the one shown in the figures, which is calculated assuming no solubility. The isotherm in Fig. 7.5 (a) shows much more scatter than those obtained at lower temperatures, but the damping data, shown in Fig. 7.5 (b), remains very clean. Ignoring the solubility of the PDA, the rise in surface pressure occurs at  $\Gamma = 2.6$  molecules/nm<sup>2</sup>; the one in the spatial damping at  $\Gamma = 2.3$  molecules/nm<sup>2</sup>; the maximum in the damping occurs at  $\Gamma_{max} = 2.6$  molecules/nm<sup>2</sup>. Although the location of the maximum cannot be determined exactly, once again we note that the maximum occurs near the point where the surface pressure starts to increase.

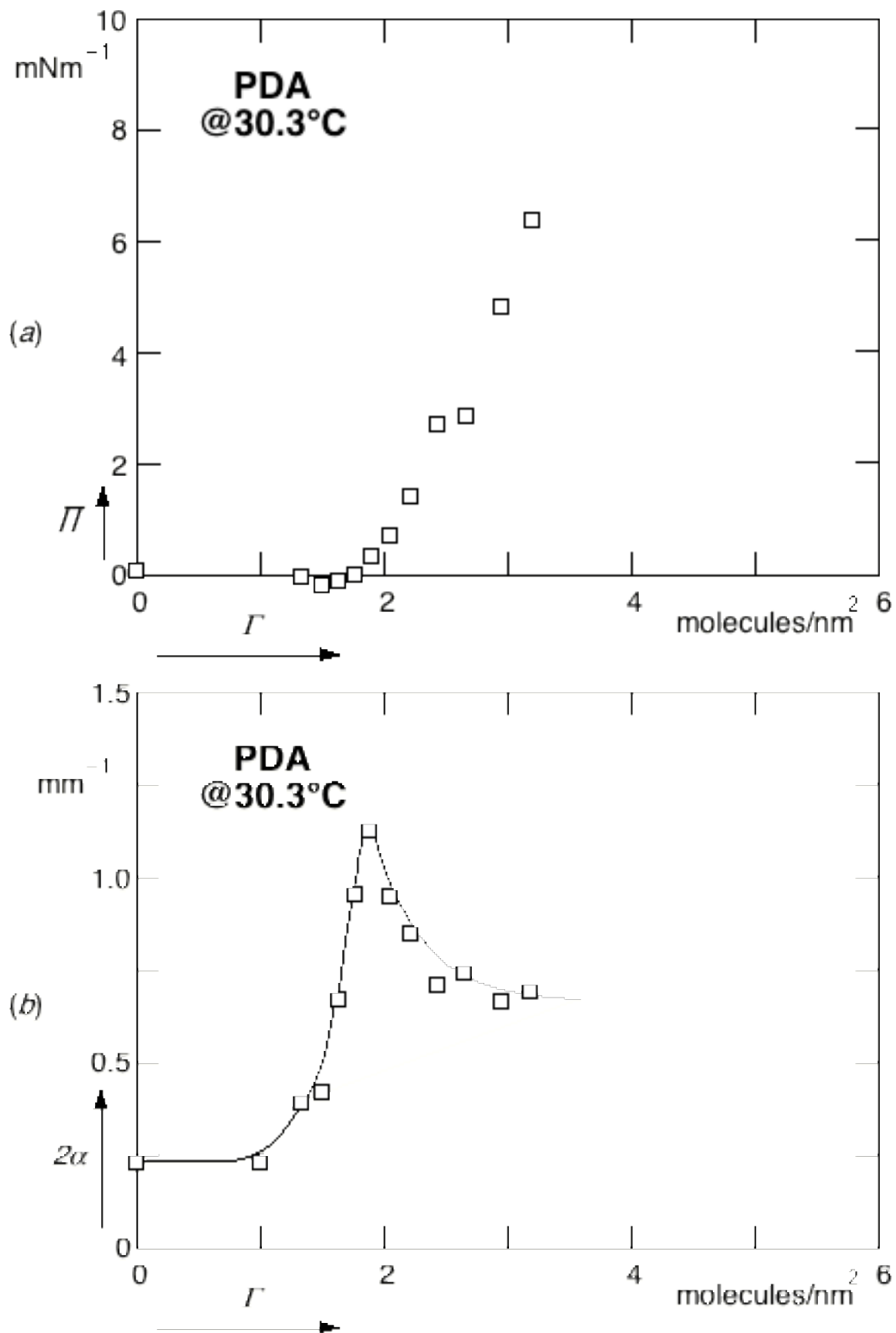
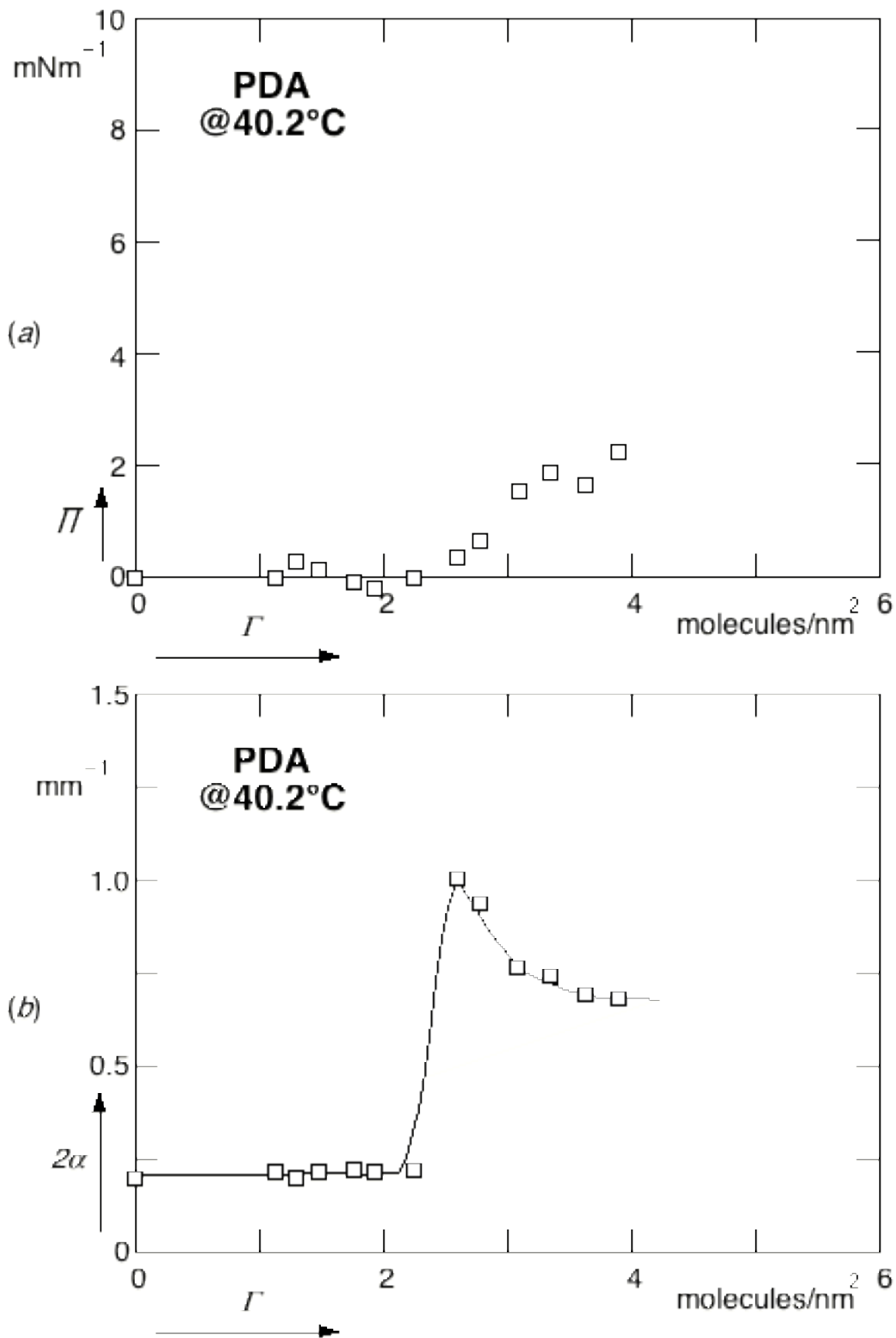


Fig. 7.4 (a) Surface pressure  $\Pi$  and (b) damping coefficient  $\alpha$  as a function of surface concentration  $\Gamma$  for pentadecanoic acid adsorbed at a water-air interface at 30.3 °C. Capillary waves of frequency 1200 Hz were induced at the interface for the damping measurements.



**Fig. 7.5** (a) Surface pressure  $\Pi$  and (b) damping coefficient  $\alpha$  as a function of surface concentration  $\Gamma$  for pentadecanoic acid adsorbed at a water-air interface at 40.2 °C. Capillary waves of frequency 1200 Hz were induced at the interface for the damping measurements.

## 7.5 Discussion

The experimental results presented above indicate that at every temperature studied, a maximum in the damping occurs at the surface concentration where the surface pressure begins to rise. We will now examine if the observed maximum can be adequately explained by the theory outlined in Section 7.3.

We recall first that the experimentally determined spatial damping coefficients  $\alpha_o$  of a pure water-air interface (see Figs. 5.4 and 5.5) agree well with the theoretical predictions. Using Eqs. (7.33), (7.34), (7.36), and (7.37), one can calculate the spatial damping coefficient  $\alpha_o$  for a pure surface, the value for a completely inelastic surface,  $\alpha_\infty$ , the maximum value of the damping,  $\alpha_{max}$ , and the surface dilational modulus at which the maximum is reached,  $\varepsilon_{max}$ . The calculated values are tabulated along with the experimental values in Table 7.1. These tabulated values reaffirm the good agreement between

| $T$ ( $^{\circ}\text{C}$ ) | $\alpha_o$ |      | $\alpha_\infty$ |      | $\alpha_{max}$ |      | $\varepsilon_{max}$ |      |
|----------------------------|------------|------|-----------------|------|----------------|------|---------------------|------|
|                            | theory     | exp  | theory          | exp  | theory         | exp  | theory              | exp  |
| 14.9                       | 1.56       | 1.67 | 2.44            | 3.59 | 4.89           | 6.01 | 11.74               | 3.43 |
| 20.1                       | 1.38       | 1.36 | 2.30            | 3.45 | 4.60           | 6.78 | 10.91               | 8.53 |
| 30.3                       | 1.12       | 1.09 | 2.08            | 3.37 | 4.16           | 5.63 | 9.58                | 4.75 |
| 40.2                       | 0.94       | 0.98 | 1.91            | 3.42 | 3.82           | 5.02 | 8.55                | 4.36 |

**Table 7.1** Theoretical and experimental values for spatial damping at three limiting cases:  $\alpha_o$  for a pure interface;  $\alpha_\infty$  for completely inelastic surface film;  $\alpha_{max}$  for the maximal damping value occurring at  $\varepsilon_{max}$ .

theory and experiments in the case of a pure interface. In the other two limits, however, consistently higher experimental damping values are found. These higher values suggest that there might be other dissipative processes present. In the theory outlined in Sections 7.2 and 7.3, effects due to surface dilational viscosity and the surface shear modulus have been ignored. These dissipative quantities may partly account for the additional capillary wave observed.

The above comparison is restricted to only three limiting cases. The spatial damping at other surface concentrations can be obtained using Eq. (7.27), but this requires the knowledge of the surface dilational modulus  $\varepsilon$  as a function of surface concentration. In the following analysis, we use, for the surface dilational modulus, static elasticity values obtained from the isotherm measurements using the relation,

$$\varepsilon_o = \frac{\partial \Pi}{\partial \Gamma_o} \Gamma_o, \quad (7.44)$$

which is equivalent to Eq. (7.2) because the surface tension and surface pressure differ from one another by a constant. Figures 7.6 (a) and 7.7 (a) show the static elasticity obtained using Eq. (7.44) from a polynomial fit to surface pressure measurements made at 14.9 °C and 20.1 °C respectively. As mentioned before, 14.9 °C is below the triple point temperature for PDA, and there is only one plateau in the isotherm, see Eq. (7.43). This translates into a flat region with zero elasticity for surface concentrations up to approximately 3.5 molecules/nm<sup>2</sup>. Beyond this value, the elasticity rises steadily, see Fig. 7.6(a). Above the triple point temperature, at 20.1 °C, there are two plateaus in the isotherm resulting in two zero elasticity regions, see Fig. 7.7 (a).

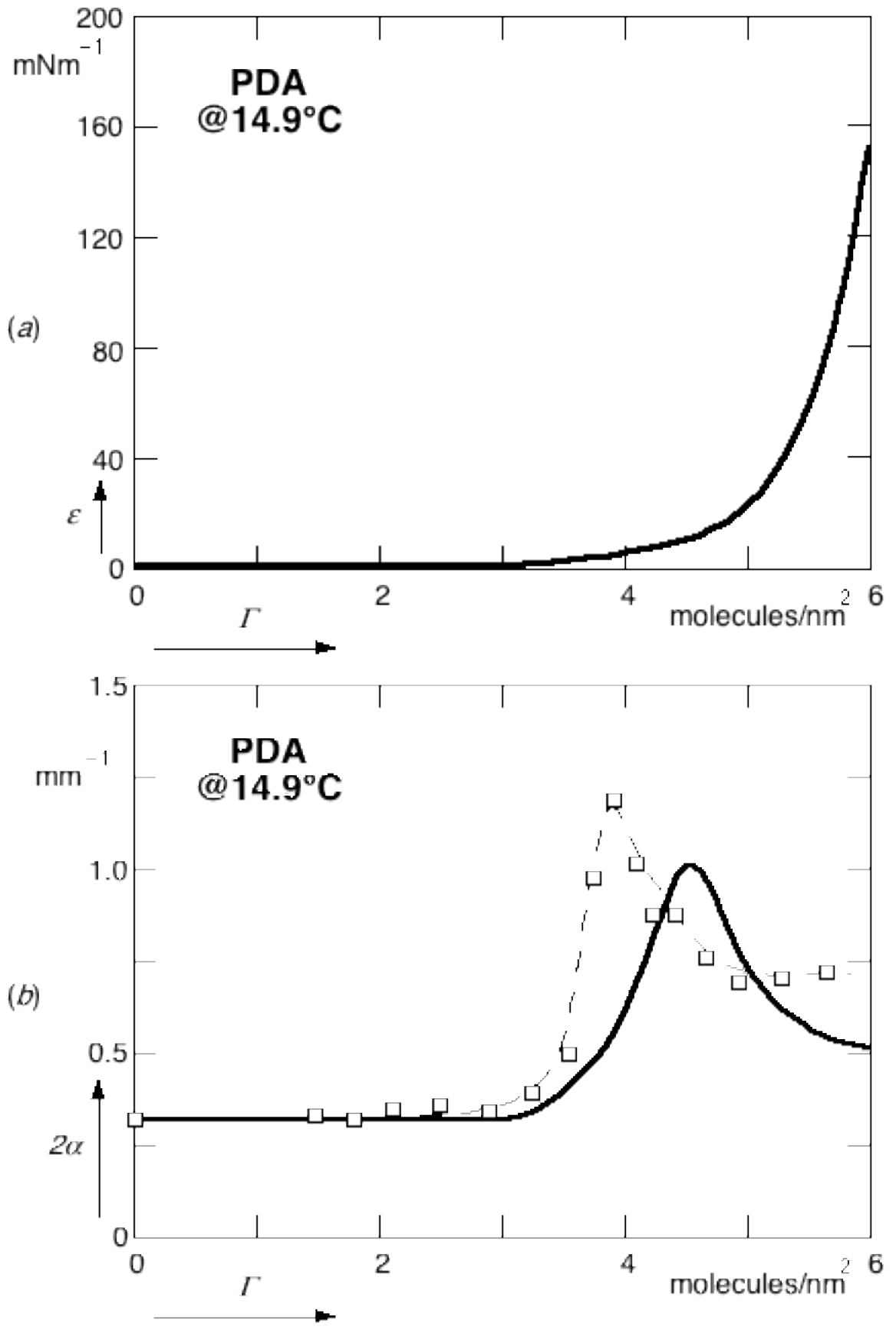


**Fig. 7.6** Plotted against the surface concentration are: (a) the static elasticity values obtained from isotherm measurements; (b) experimentally observed damping coefficients (squares) and the corresponding predictions (solid line) obtained using Eq. (7.27)

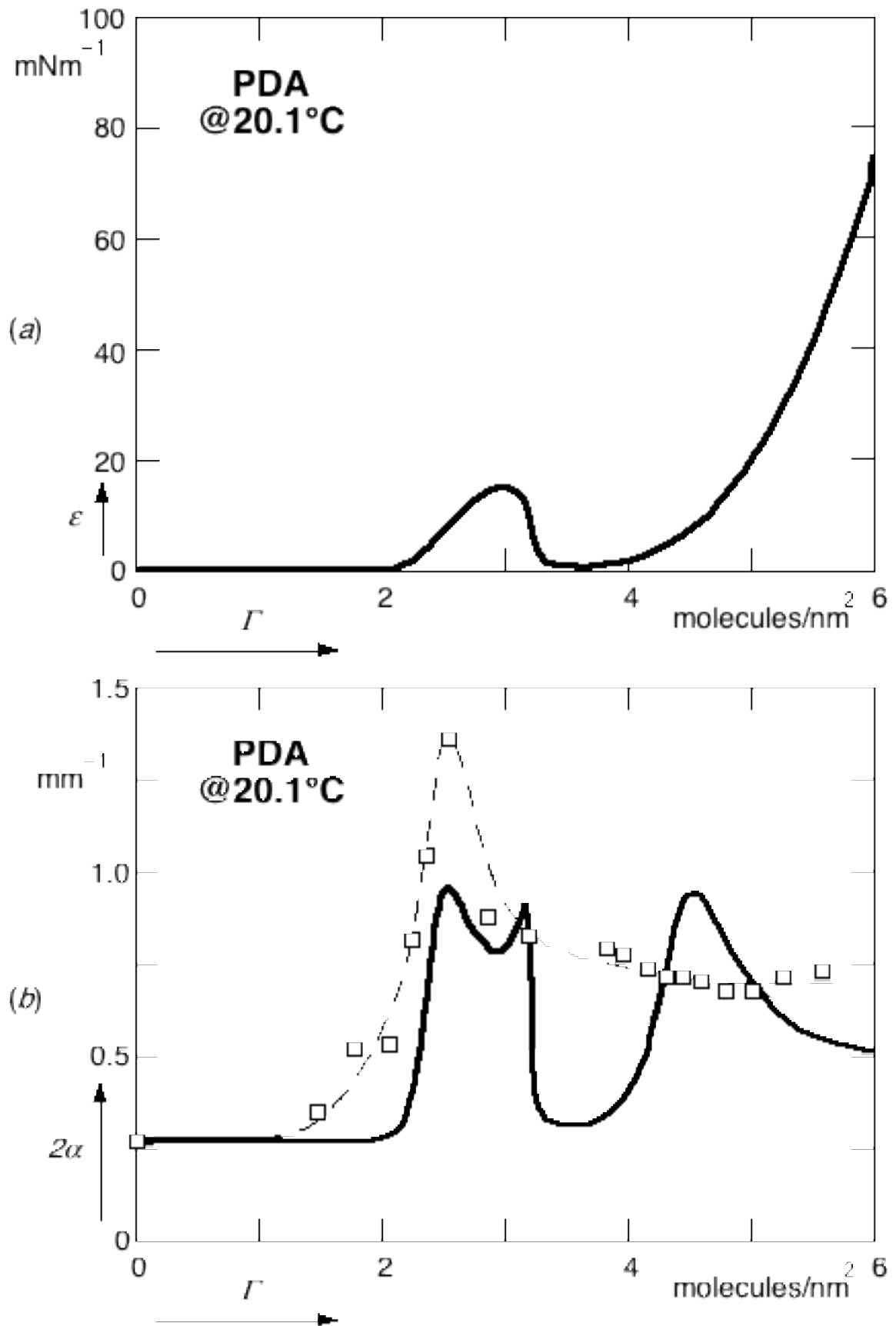


Fig. 7.7 Plotted against the surface concentration are: (a) the static elasticity values obtained from isotherm measurements; (b) experimentally observed damping coefficients (squares) and the corresponding predictions (solid line) obtained using Eq. (7.27)

Using Eq. (7.27) we can now obtain the spatial damping coefficient as a function of surface concentration from the calculated elasticity. The results are shown in Figs. 7.6 (b) and 7.7 (b). Comparing the measured spatial damping results at 14.9 °C, with the calculated values in Fig. 7.6 (b), we find that the results agree qualitatively. Although both plots show a maximum in damping, the exact location and size of the maximum are different. The discrepancy in the peak location may be due to uncertainty in the surface pressure measurement as well as accuracy of the polynomial fit used to obtain the elasticity curve, while that in the damping value may be due to additional dissipative processes. Above the triple point the agreement is not as good, see Fig. 7.7(b). Instead of a single maximum in the spatial damping curve, as observed experimentally, the theory predicts three peaks. This prediction is due to the existence of the second plateau which causes the elasticity curve to fall back to zero from some finite value at the low concentration end of the LE–LC coexistence region, and rise up again at the high concentration end. As a result, the curve in Fig. 7.7 (a) coincides with the calculated value  $\varepsilon_{max} = 10.91 \text{ mN}\cdot\text{m}^{-1}$  (see Table 7.1) in three different locations. Although the first of the three peaks agrees well with the experimental one, see Fig. 7.7(b), the hydrodynamic theory as outlined here cannot fully account for the observed damping.

One explanation for the damping peak has its basis on the coupling between different modes of surface waves. Apart from the transverse capillary waves at the interface, Lucassen discovered that there exists another kind of surface waves, a longitudinal surface wave [Lucassen, 1968], which obeys the same boundary conditions. He and his co-worker explained the maximal spatial damping as a resonance phenomenon involving these two types of wave motion. The resonance condition is satisfied when the wavelength of the

transverse capillary wave at a given frequency equals that of the longitudinal surface wave [Lucassen-Reynders and Lucassen, 1969]. and their computer calculations indicate that this resonance condition is met only when the surface dilational modulus assumes the value  $\varepsilon_{max}$  in Eq. (7.33). In other words, this argument, like the theory in Section 7.2 and 7.3, also predicts a peak in damping to occur when  $\varepsilon = \varepsilon_{max}$ . While the coupling between longitudinal surface waves and transverse capillary waves may exist and account for the extra damping observed experimentally (see Table 7.1), this argument still predicts three peaks to occur for a system with a elasticity curve like the one in Fig. 7.7 (a) and cannot explain the single peak observed experimentally as indicated in Fig. 7.7 (b).

The hydrodynamic theory described in Sections 7.2 and 7.3 describes surface wave propagation at a liquid-vapor interface in the presence of a homogeneous monolayer. From fluorescent microscopy, we learn that the monolayer is inhomogeneous in the coexistence regions [Moore, Knobler, *et al.*, 1990], but as far as we know, there exists no theoretical treatment of surface wave propagation at an interface covered with an inhomogeneous monolayer. The existence of domain structures in the coexistence region, unaccounted for in the above theory, may help explain the location of the maximum, as well as consistently higher damping value obtained experimentally.

Surface waves propagating at an interface cause periodic contraction and expansion. This periodic change in surface area translates into a periodic change in the surface concentration of surfactant molecules. In the G-LE coexistence region, such a variation modifies the ratio of surfactant molecules in the gaseous phase to those in the LE phase. In the low surface concentration end of the region, this change does not affect the inhomogeneous nature of the surface film. At higher concentrations near the coexistence phase boundary, where the G-LE

transition is approaching completion<sup>18</sup>, oscillations in the surface concentration may drive the monolayer back and forth between a homogeneous and inhomogeneous film. With a fixed wave amplitude, this effect is expected to be most pronounced around the coexistence phase boundary. Recent work by Miyano and Tamada on capillary wave propagation at an interface covered with an inhomogeneous monolayer in the G-LE coexistence region also demonstrates the lack of surface film influence until a 90 % coverage of the LE phase is attained [Miyano and Tamada, 1992]. Repeated switching back and forth between a homogeneous and inhomogeneous film leads to the continuous breakage and formation of island domains in the monolayer. Such a process is not be described by the hydrodynamic theory previously discussed. The additional energy dissipated<sup>19</sup> by this switching mechanism may account for the increased damping observed at higher concentrations in the G-LE coexistence region, as well as the discrepancy between the theoretical and experimental values of  $\alpha_{\max}$  (see Table 7.1). In addition, this process may also explain the correspondence between the maximal spatial damping coefficient and the initiation of surface pressure growth. One should note that this effect comes into play only when the domain response time is shorter than the period of the capillary wave.

Similar to the G-LE coexistence region, the LE-LC coexistence region is also inhomogeneous, exhibiting domain structures. If the damping peak is sensitive to the conversion process of a homogeneous film to an inhomogeneous one, and vice-versa, one would expect damping peaks to be located at the beginning and end of the LE-LC transition. Our experimental findings, however,

---

<sup>18</sup>When the monolayer enters the LE phase, a complete liquid film coverage is attained, and a homogeneous film is resulted.

<sup>19</sup>This energy can be thought of as equivalent to the latent heat in first-order phase transitions.

show otherwise. The absence of damping peaks may be due to the difference in phase characteristics, like compressibility, for instance, between the two coexistence regions.

## 7.6 Damping as a Probe of Phase Transitions

In Section 6.4, we described the difficulties encountered in mapping out the phase boundaries and finding the critical temperature,  $T_c$ , of the G-LE coexistence region of PDA. Because the surface pressure changes in this region are small, isotherm measurements require great care, and similar experimental data can lead to very different conclusions depending on the criteria used to interpret the data. Fluorescence microscopy, on the other hand, provides clear pictures of the surface morphology, but requires the addition of fluorescent dyes which may alter the phase behavior of the film. The damping results discussed in Section 7.4 indicates that peaks in the spatial damping coefficient occur at the surface concentrations which signify the initiation of surface pressure growth. Analogous results have been observed in temporal damping measurements [Chen, Sano, *et al.*, 1986]. Such results suggest that capillary wave damping measurements provide a sensitive tool for locating the phase transitions of a monolayer. In the case of PDA, damping results allow us to identify the high concentration end of the G-LE phase boundary. Table 7.2 shows the experimentally determined values of surface area for which maximal damping occurs at various temperatures. These values agree well with the phase boundary on the high surface concentration end of the G-LE coexistence region obtained by other workers (see Table 6.1).

| $T$ (°C) | $\mathcal{A}_{LE}$ or $\mathcal{A}_{LC}$ (Å <sup>2</sup> ) |
|----------|--|
| 14.9     | 25   |
| 20.1     | 40   |
| 30.3     | 51   |

**Table 7.2** Experimentally determined values of surface area at which maximal damping occurs at various temperatures.

Although our damping results do not allow us to locate the low concentration end of the G-LE phase boundary, the observed increase in surface area,  $\mathcal{A}_{LE}$ , with increasing temperature indicates that the coexistence region diminishes in size with increasing temperature until the critical temperature,  $T_c$ , for the formation of the LE phase is reached. The determination of the critical temperature from capillary wave damping measurements is, however, not as simple as we do not completely understand the damping mechanism or the behavior of the isotherms above the critical point. If as outlined in Section 7.5, the damping peak can be attributed to the additional energy dissipated involved in the forming of a coherent film, one would expect the peak to disappear above the critical temperature. If, on the other hand, one subscribes to the hydrodynamic theory in Sections 7.2 and 7.3, a peak should exist above  $T_c$ , at the surface dilational modulus given by Eq. (7.33). Depending on the specific shape of the isotherm<sup>20</sup>, this peak may be broadened or occur at a much lower surface

---

<sup>20</sup>For temperatures well above the critical point, the surface film is expected to behave like an ideal-gas; for an isotherm with a small slope, the damping peak is expected to be significantly broadened, and for an isotherm with a large slope, the damping peak is expected to occur at a much lower surface concentration. For temperatures above but close to the critical temperature, it is well-known that the isotherms may have inflection points which can result in damping behavior similar to that observed below the critical point.

concentration. With the information available, it is not possible to determine  $T_c$  exactly.

## 7.7 Conclusion and Future Work

Using hydrodynamic theory, we reviewed the damping of capillary waves at a liquid-vapor interface in the presence of a homogeneous monolayer of surfactant molecules. We also carried out direct measurements of the spatial damping coefficient for such waves traveling on a water-air interface with an adsorbed monolayer of PDA, at temperatures ranging from below the PDA triple point to 40 °C. A maximum in spatial damping as a function of surface concentration is observed at all temperatures, and occurs at a concentration which marks the initial rise of the surface pressure from its zero value. The discrepancies between hydrodynamic predictions and experimental results may be explained by the inhomogeneous nature of the film in the coexistence region. The simple hydrodynamic theory presented in Sections 7.2 and 7.3 does not allow for an inhomogeneous surface configuration. In Section 7.5, we give a heuristic argument which may explain the additional dissipation observed at the coexistence phase boundary. Comparison between the position at which maximal spatial damping occurs and measurements of the phase boundary surface area,  $A_{LE}$ , found by other workers, shows good agreement, suggesting that the spatial damping of capillary waves can be used as an indicator of phase transitions. Our search for a critical temperature of the G-LE transition was, however, inconclusive.

A better understanding of damping in the vicinity of the critical temperature is necessary to determine if capillary wave damping measurements

can provide useful information in this regime. Damping measurements with monolayers of esters of different chain length (some with established critical temperature below room temperature) will be performed and may elucidate the physics near the critical temperature. The effects of inhomogeneous monolayer films on capillary wave damping are still not well understood. The ability to observe the structure of the monolayer while carrying out spatial damping measurements may lead to better understanding. A Brewster angle microscopy<sup>21</sup> setup is being built to allow such direct observation of the surface morphology.

The study of surface wave damping has a long history, yet various aspects of the observed behavior and underlying mechanisms are not well understood. It is my hope that this set of experiments will stimulate new theoretical and experimental efforts in the field, leading to insights into the viscoelastic properties of surface films, and elucidating the basic concepts of surface wave damping.

---

<sup>21</sup>This microscope employs the characteristics that  $p$ -polarized light has zero reflectivity at Brewster angle. The formation of a monolayer at the interface slightly modifies the Brewster angle, and different domains give different reflectivities for the incident light. The Brewster angle microscopy therefore allows one to detect monolayer inhomogeneity [Henon and Meunier, 1991, Honig and Mobius, 1991].

## References

- Aiken, *Proc. Roy. Soc., Edin. (V)*, **12**, 56 (1883).
- Atkins, P.W., *Physical Chemistry* (W.H. Freeman & Co., San Francisco, 1982).
- Chen, Y.-L., Sano, M., M. Kawaguchi, H.Y. and Zografu, G., *Langmuir*, **2**, 349 (1986).
- Davies, J.T. and Vose, R.W., *Proc. Roy. Soc.*, **A286**, 218 (1965).
- Dippy, J.A.G., *Chem. Rev.*, **25**, 151 (1939).
- Dorrestein, R., *Koninkl. Ned. Akad. Wetenschap. Proc.*, **B45**, 260 (1951).
- Franklin, B., *Roy. Soc. London, Philos. Trans.*, **64**, 445 (1774).
- Goodrich, F.C., *Proc. Roy. Soc. (London)*, **A260**, 481 (1961).
- Hansen, R.S. and Mann, J.A., *J. Appl. Phys.*, **35**, 152 (1964).
- Harkins, W.D., *The Physical Chemistry of Surface Films* (Reinhold Publishing Corporation, New York, 1952).
- Henon, S. and Meunier, J., *Rev. Sci. Instrum.*, **62**, 936 (1991).
- Honig, D. and Mobious, D., *J. Phys. Chem.*, **95**, 4590 (1991).
- Levich, V.G., *Act. Phys. U.R.S.S.*, **14**, 307 (1941).
- Levich, V.G., *Physicochemical Hydrodynamics* (Prentice-Hall, Englewood Cliff, New Jersey, 1962).
- Lucassen, J., *Trans. Faraday Soc.*, **64**, 2221 (1968).
- Lucassen-Reynders, E.H. and Lucassen, J., *Adv. Coll. Int. Sci.*, **2**, 347 (1969).
- Miyano, K. and Tamada, K., *Langmuir*, **8**, 160 (1992).

Moore, B.G., Knobler, C.M., Akamatsu, S. and Rondelez, F., *J. Phys. Chem.*, **94**, 9588 (1990).

Nelson, D., **unpublished report**, (1985).

Pallas, N.R. and Pethica, B.A., *J. Chem Soc., Fara. Trans1*, **83**, 585 (1987).

Plinius, *Historia Naturalis*

Rayleigh, L., *Proc. Roy. Soc. London*, **47**, 364 (1890).

Reynolds, O., *Brit. Ass. Rep.*, (1880).

Tempel, M.v.d. and Riet, R.P.v.d., *J. Chem. Phys.*, **42**, 2769 (1965).